Simulation and Control of an Underwater Hexapod Robot

Christina Georgiades

Department of Mechanical Engineering
McGill University, Montreal

February 2005

A thesis submitted to McGill University in partial fulfillment of the requirements of the degree of Master of Engineering

Your file Votre référence
ISBN: 0-494-12604-3
Our file Notre référence
ISBN: 0-494-12604-3

Abstract

AQUA is an underwater hexapod robot which uses its paddles to propel itself and to control its orientation. The use of oscillating paddles for propulsion and control represented a novel and challenging problem, which motivated the need for a simulation of the motion of the robot based on its paddle oscillations. The most difficult aspect of this simulation was the characterization of the forces generated by the paddles oscillating in the water. In this work, a model predicting the forces produced by an oscillating rigid paddle was developed and validated experimentally. Also, the forces produced by a flexible fin were determined experimentally and were compared to those generated by the rigid paddle. Rigid paddle and flexible fin experiments were performed on an experimental setup, which was designed and built to measure the forces and torques produced by a paddle oscillating in a water tank. Finally, a simulation of the AQUA robot was developed, based on the validated rigid paddle model.

Résumé

AQUA est un robot hexapode sous-marin qui utilise ses palmes pour se propulser et pour contrôler son orientation. L'utilisation des palmes pour la propulsion et le contrôle d'orientation représente un problème intéressant qui motive le besoin d'une simulation du mouvement du robot résultant des oscillations des palmes. L'aspect le plus difficile de cette simulation est la détermination des forces produites par une palme oscillant dans l'eau. Dans cette oeuvre, un modèle prédisant les forces produites par une palme rigide qui oscille a été développé et validé expérimentalement. Aussi, les forces produites par une palme flexible ont été déterminées expérimentalement et ont été comparées aux forces produites par la palme rigide. Les expériences avec les palmes rigide et flexible ont été exécutées sur une installation expérimentale qui a été conçue et construite pour mesurer les forces et les couples produits par une palme oscillant dans un réservoir d'eau. Enfin, une simulation du robot AQUA a été développée, basée sur le modèle de palme rigide validé.

Table of Contents

List of Figures

List of Tables

Nomenclature

A	amplitude of oscillation [*radians*]
A_f	frontal area of the paddle [m^2]
B	width of the robot [m]
$\vec{B}$ and $\vec{M}_b$	buoyancy force vector and buoyancy moment vector
$C_{D\max}$	maximum value of drag coefficient of the rigid paddle
$C_{L\max}$	maximum value of lift coefficient of the rigid paddle
$\boldsymbol{C}(\vec{v})$, $\boldsymbol{C}_A(\vec{v})$ and $\boldsymbol{C}_{RB}(\vec{v})$	matrix of Coriolis and centripetal terms, matrix of added hydrodynamic Coriolis and centripetal terms and rigid-body Coriolis and centripetal matrix
D	drag force [N]
$F_{//}$	force parallel to the paddle [N]
$F_{\perp}$	force perpendicular to the paddle [N]
$\vec{F}$	vector of forces $\vec{F}_{cm}$ and moments $\vec{M}_{cm}$ acting on the robot
$\vec{F}_{cm}$	total external force vector acting at the center of mass of the robot
$F_{cm\,x}$, $F_{cm\,y}$ and $F_{cm\,z}$	total external force vector components along the x-, y- and z-axes [N]
$\vec{F}_g$	gravitational force vector
$\vec{F}_p$ and $\vec{M}_p$	propulsive force and propulsive moment vectors
$F_{px\,j}$, $F_{py\,j}$ and $F_{pz\,j}$	components of $\vec{F}_p$ for paddle j [N]
$\vec{F}_h$ and $\vec{M}_h$	hydrodynamic force and hydrodynamic moment vectors
$\vec{g}$	gravitational acceleration vector
H	height of the robot [m]
I_{xx}, I_{yy} and I_{zz}	moments of inertia of the robot about the x-, y- and z-axes [kg]
I_{xy}, I_{xz} and I_{yz}	products of inertia of the robot [$kg{\cdot}m^2$]

J	moment of inertia of the paddle [$kg \cdot m^2$]
K_p	proportional gain of the PD controller
K_v	derivative gain of the PD controller
l	length of the paddle [m]
L	lift force [N] or length of the robot [m] depending on context
$L_{\dot{p}}$, $M_{\dot{q}}$ and $N_{\dot{r}}$	hydrodynamic derivatives [$kg \cdot m^2$]
m	mass of the robot [kg]
$\vec{M}_{cm}$	total external moment vector acting at the center of mass of the robot
$M_{cm\,x}$, $M_{cm\,y}$ and $M_{cm\,z}$	total external moment vector components about the x-, y- and z- axes [Nm]
$\boldsymbol{M}$, $\boldsymbol{M}_A$ and $\boldsymbol{M}_{RB}$	inertia matrix, added inertia matrix and rigid-body inertia matrix
p, q and r	components of body angular velocity about the x-, y- and z-axes [$rads/s$]
$\vec{P}_j$	position of the point of application of the drag and lift forces generated by paddle j.
R	oscillation ratio
S	surface area of the paddle [m^2]
t	time [s]
t_f	time at end of stroke or recovery phase [s]
t_r	recovery time [s]
t_s	stroke time [s]
T	period of oscillation [s]
$\boldsymbol{T}$	rotation matrix
T_{res}	resistive torque [Nm]
U	velocity of flow impinging on the paddle [m/s]
u, v and w	components of velocity of the mass center along the x-, y- and z-axes [m/s]
$\dot{\vec{v}}$ and $\vec{v}$	acceleration and velocity vectors of the robot's center of

	mass with respect to the body-fixed frame.
v	inflow velocity [*m/s*]
V	Volume of the robot [m^3]
V_d	volume of water displaced by the paddle during stroke or oscillation [m^3]
w	width of the paddle [*m*]
x_b, y_b and z_b	distances from the center of mass to the center of buoyancy along the *x*-, *y*- and *z*-axes [*m*]
$x_{\text{hip}\,j}$, $y_{\text{hip}\,j}$ and $z_{\text{hip}\,j}$	distances from the center of mass to hip *j* along the *x*-, *y*- and *z*-axes [*m*]
$X_{\dot{u}}$, $Y_{\dot{v}}$ and $Z_{\dot{w}}$	hydrodynamic derivatives [*kg*]
α	angle of attack [*radians*]
β	direction of flow impinging on the paddle [*radians*]
γ, $\dot{\gamma}$ and $\ddot{\gamma}$	angular position, angular velocity and angular acceleration of the paddle [*radians, radians/s, radians/s*^{2}]
γ_0	offset angle [*radians*]
γ_d and $\dot{\gamma}_d$	desired angular position and velocity of the paddle [*radians, radians/s*]
γ_f and $\dot{\gamma}_f$	paddle angular position and velocity at end of stroke or recovery phase [*radians, radians/s*]
γ_i and $\dot{\gamma}_i$	paddle angular position and velocity at beginning of stroke or recovery phase [*radians, radians/s*]
δ	logarithmic decrement
ζ	damping ratio
θ	Euler angle (pitch) [*radians*]
ρ	density of water [kg/m^3]
τ	torque commanded to the motor [*Nm*]
ϕ	Euler angle (roll) [*radians*]
ψ	Euler angle (yaw) [*radians*]

Acknowledgements

I would like to express my appreciation and gratitude to:

- My parents, first and foremost, for supporting me in every possible way. I would not be where I am today had it not been for them.
- Professor Martin Buehler for giving me a lifetime opportunity, by giving me a chance and a place in his lab.
- Professor Meyer Nahon for his supervision, his dedication, his understanding, his support, his care and his advice.
- Precarn Inc., which manages the Institute for Robotics and Intelligent Systems, for funding AQUA as well as for supporting me financially.
- My sister and cousin, a.k.a. my "Tech. Supports", for being there when I experienced difficulties. I can't even imagine my life without them.
- Francis Esmonde-White for believing in me, encouraging me and helping me.
- James Smith for helping with a countless number of things, for answering all my computer and programming related questions, for listening every time I needed an attentive ear, for supporting and for encouraging me. I would also like to thank James for resuscitating my thesis with his Mac, when my PC was not able to open my document, five days before it was due.
- Dave McMordie for answering all my Electrical Engineering related questions and for helping me pursue my interest in robotics.
- Aaron Saunders for guiding me, helping me and encouraging me.
- Gen Vinois for all the things that you took care of for everyone at the Ambulatory Robotics Lab.
- Neil Neville and François Deschênes, who were writing their thesis at the same time as I was writing mine, for their encouragement and their help, but mostly for their company.
- Matt Smith for making my days at the Ambulatory Robotics Lab a bit brighter with his presence.

- All the other really bright people that I had the opportunity to work with at the Ambulatory Robotics Lab: Chris Prahacs, Don Campbell, Ioannis Rekleitis, Shane Saunderson, Enrico Sabelli, John Sheldon, Aki Sato, Evgeni Kiriy, Neil Wyper, Jacqui McCallum, Julien Marcil, Mike Tolley and Carl Steeves. They made the lab a stimulating and fun place to work at.
- Laurent Haccoun, Julie Agar, Prakash Patel and Rebecca Houwer, fellow graduate students, for their friendship, their encouragement and their support.
- Professor Gaskin for letting me use the tank in her research facility and Thomas Lavertu for sharing it with me and preparing it every time I needed to use it.
- Mathieu Kemp, from Nekton Research in North Carolina, for spending an entire weekend running flexible fin experiments in a tow tank with me.
- Dr. John N. Hammar, from ESDU, for taking time during his business trip to Montreal to show me the data item that I needed for my simulation.

1. Introduction

Underwater vehicle designers rely increasingly on simulations in order to design a vehicle and to develop its controllers. This work describes the development of a simulation of AQUA: an underwater hexapod robot that is very different from conventional underwater vehicles and legged underwater vehicles. AQUA uses paddles to achieve propulsion and control whereas conventional underwater vehicles use thrusters and control surfaces. In this work, an analytical model was developed to predict the forces generated by an oscillating rigid paddle. The model was validated experimentally using a test setup of a single paddle in a static water tank. A simulation of the entire AQUA vehicle was then developed, based on the validated rigid paddle model.

1.1. Conventional Underwater Vehicles and Legged Underwater Vehicles

In the present work, the term 'conventional' is used to label a class of underwater vehicles comprising Remotely Operated Vehicles (ROVs) and Autonomous Underwater Vehicles (AUVs) because most underwater vehicles are of either type. Legged underwater vehicles can be autonomous or remotely operated, but they form a class of underwater vehicles separate from the conventional ones. An ROV is shown in Figure 1-1 and an AUV is shown in Figure 1-2.

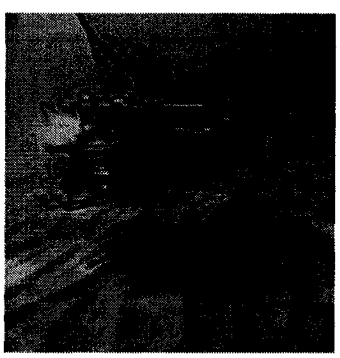

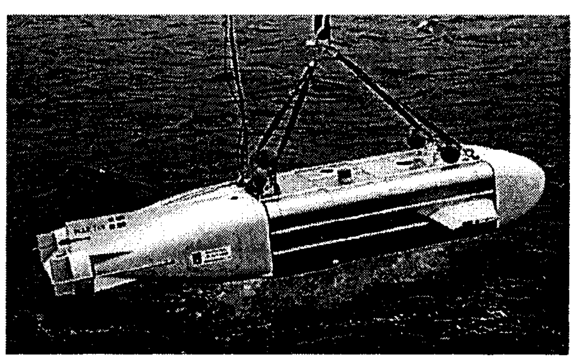

Figure 1-1 (left): Remotely Operated Vehicle. **Figure 1-2 (right):** Autonomous Underwater Vehicle

Remotely Operated Vehicles (ROVs)

ROVs are unmanned underwater robotic vehicles, typically box-shaped, which are controlled remotely by a pilot. Some ROVs work routinely at depths of 3000 to 5000 meters. ROVs can be small, weighing less than 5 kg, with just a camera for simple observation. They can also be quite large and complex, with several dexterous manipulator arms, cameras, tools and other equipment. Basic features of a ROV include thrusters, cameras and various sensors (water temperature sensors, depth sensors, sonar…). ROVs typically move over short distances at relatively slow speeds - on the order of 1 meter per second or less. For any tasks involving manipulation and requiring maneuverability, they are the most cost-effective platform.

The vehicle's operator remains on land or on a ship, in front of a remote control console, while the vehicle ventures underwater. Using a joystick, a camera control and a video monitor, the operator moves the vehicle and points the camera to desired locations. The vehicle is linked to the control console by an umbilical cable. The umbilical cable carries electric power and control commands to the thrusters and other vehicle systems. The umbilical cable also carries data from the vehicle's cameras and sensors to the operator.

The umbilical is one of the ROV's greatest assets because it can carry unlimited power for high endurance operation and it can transmit large amounts of data. The umbilical is also one of the ROV's greatest drawbacks because it limits the range and speed a ROV can travel, and it creates drag. Today, advanced technology is allowing many ROVs to shed their cable, and thus become free to roam the ocean without this physical constraint. These emerging systems, which are usually battery powered, are called Autonomous Underwater Vehicles (AUVs).

Autonomous Underwater Vehicles (AUVs)

AUVs are unmanned underwater robotic vehicles of varying lengths (1-10m), which resemble torpedoes. An AUV contains a propulsion system consisting of one or two thrusters, control surfaces to control the vehicle's attitude, a pressure hull to contain electronics and power, and a streamlined fairing to reduce hydrodynamic drag. The vehicle is self-sufficient since it carries its own energy source and is programmed to carry out an underwater mission without assistance from an operator on the surface. The programs allow guidance and navigation between pre-determined geographic positions, obstacle avoidance, and recovery in case of equipment breakdown. Procedures for the operation of the payload devices, which the AUV carries, are also provided.

One disadvantage of the AUV carrying its own energy source is that it has limited endurance. On the other hand, an advantage of it not having a tether is that it can undertake missions over long ranges at reasonable speeds – on the order of 1.5 to 2 m/s. For example, Theseus, a large AUV having a possible range of 700km and a speed of 2m/s, laid a fiber-optic cable in a completely autonomous mode for a distance of 200km under Arctic sea-ice and then returned to the launch station for recovery [1]. When an AUV is recovered, at the end of its mission, the data stored on the vehicle is retrieved.

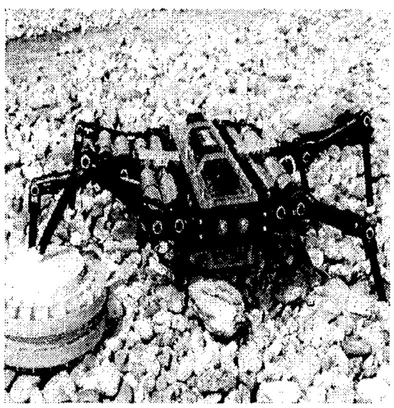

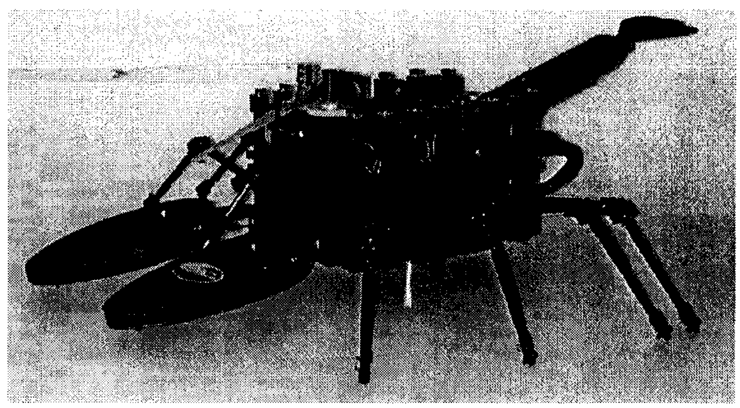

Figure 1-3 (left): iRobot's Ariel. **Figure 1-4 (right):** Northeastern University's Ambulatory Underwater Robot.

Legged Underwater Vehicles

Legged underwater robots are typically multi-legged robotic platforms that resemble lobsters or crabs. Modeled after a crab, irobot's Ariel (shown in Figure 1-3) is a six-legged robot capable of walking either on land or underwater in the turbulent surf zone [2]. Based on the lobster, Northeastern University's Ambulatory Underwater Robot (shown in Figure 1-4) is an eight-legged vehicle that can crawl across the sea floor, clamber over rocks and fight currents [3, 4]. Legged underwater robots are able to crawl on the ocean bottom as well as on land. They can traverse a broad range of environments, but they are not able to navigate the water column above the ocean bottom.

1.2. Evolution of RHex

As stated earlier, AQUA is different from conventional underwater vehicles and legged underwater vehicles. It is based on RHex, a terrestrial six-legged robot developed in a collaboration between the Ambulatory Robotics Laboratory at McGill University, the University of Michigan, the University of California at Berkeley and Carnegie Mellon University, with sponsorship from DARPA [5, 6]. RHex, shown in Figure 1-5, is a power autonomous robot with compliant re-circulating half-circle shaped legs, which each have only one actuator. RHex uses a clock-driven alternating open-loop tripod gait to walk and run. The robot is able to traverse rugged and obstacle-ridden terrain that few other robots can negotiate at all. RHex can walk, run at speeds of up to 2.7 m/s on flat terrain [7], traverse height variations well exceeding its body clearance, climb slopes over 40°, climb stairs [8], pronk [9], bound [10], flip [11] and even run on its two rear legs [12].


Figure 1-5 (left): RHex. **Figure 1-6 (right):** RHex sealed with a plastic bag.

Because RHex routinely encountered hazards such as rain, mud, sticks and sand, and falls from heights greater than 30 cm, it became apparent that the original aluminum frame and Lexan cover were not sufficient for rigorous outdoor testing. Moreover, RHex demonstrated amphibious abilities for the first time when its body was sealed with a plastic bag shown in Figure 1-6. It walked from a sandy beach into a lake, swam on the water surface using its unmodified legs and the tripod gait, and walked back out on land. This amphibious experiment, combined with the RHex project's mandate to demonstrate increased ruggedness in all outdoor environments, initiated the development of three successive robot designs: Shelley-RHex, Rugged-RHex, and AQUA [13].

Shelley had a waterproof shell made out of carbon fiber, which enabled it to operate amphibiously: it could walk on land, as shown in Figure 1-7, and swim at the surface of the water, as shown in Figure 1-8.

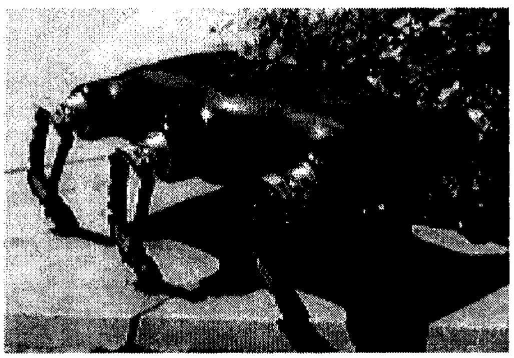
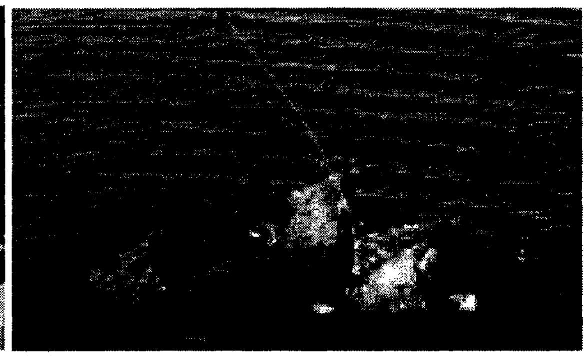

Figure 1-7 (left): Shelley out of the water. **Figure 1-8 (right):** Shelley swimming in the water.

Rugged-RHex has two modes of operation: it can walk on land (Figure 1-9) and swim on the water surface using half-circle shaped legs, or it can swim underwater (Figure 1-10) using flexible paddles. The oscillating flexible paddles propel the robot and act as surfaces that control its attitude. When the robot swims underwater, it is ballasted to be neutrally buoyant. A tether was required to transmit the robot's video signal to the vehicle operator and the operator's control commands to the robot. Since the Rugged-RHex platform has two NiMH radio batteries onboard, which provide it power to operate continuously for more than two hours, there was no need for power wires in the tether.

 

Figure 1-9 (left): Rugged-RHex with half-circle shaped legs. **Figure 1-10 (right):** Rugged-RHex with flexible fins in water.

The goal of the AQUA project was to develop a platform capable of walking on land, crawling at the bottom of the sea, swimming on the surface and underwater, and diving to a depth of 10m. The robot had to be able to walk in the water from the shore and, once in the water, transition between crawling at the bottom of the sea and swimming. Based on the Rugged-RHex platform and with funding from the Canadian Institute for Robotics and Intelligent Systems (IRIS), AQUA, shown in Figure 1-11, was developed [14].

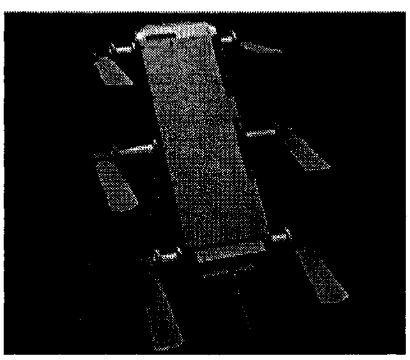 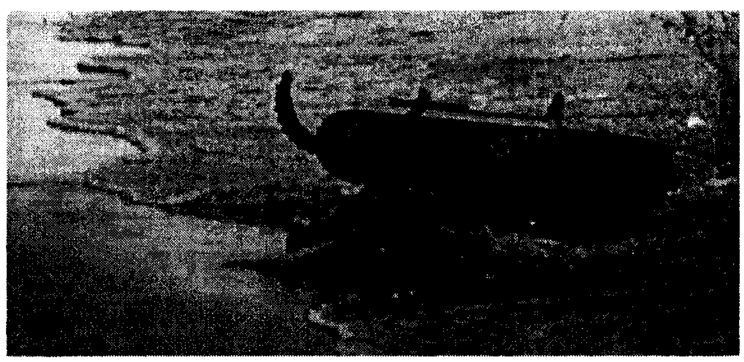

Figure 1-11 (left): AQUA with flexible fins underwater. **Figure 1-12 (right):** AQUA with amphibious legs exiting the water.

With amphibious legs, which act as flippers during swimming and legs during walking, AQUA was able to walk from the shore into the water or from the water to the shore. Figure 1-12 shows AQUA exiting the water. The robot could walk at the bottom of the sea if it was ballasted to be negatively buoyant. Before the robot is able to transition between swimming and crawling at the bottom of the sea, a computer controlled buoyancy system needs to be developed. That system would enable the platform to change its buoyancy depending on whether it wants to walk on the bottom of the sea, swim underwater or float to the surface.

1.3. Differences Between AQUA and Other Underwater Vehicles

Many underwater applications (such as reef or pipeline inspection, fish stock surveillance, marine life observation and environmental disaster assessment) involve stationary observation. Although mobility is required to bring the vehicle into proximity of the task, the task itself relies on the vehicle to maintain a constant pose. Station keeping is a complex and energy-consuming task for swimming-only thruster-driven aquatic robots because they must actively control their thrusters and buoyancy in order to maintain their pose. Some ROVs have the ability to land on the sea bottom, just like AQUA, but they cannot move along the sea bottom the way AQUA can. Hence, for station keeping, legged robots are more attractive than swimming-only robots. For long distance movement, however, swimming robots are more attractive than walking robots because swimming is more energy efficient than walking. Hence, for stationary observation applications involving long distance movement and station keeping, a robot like AQUA, which is capable of both swimming and walking, is very attractive.

Another issue with thruster-based aquatic vehicles is that they must be deployed and recovered from sufficiently deep water in order to be able to maneuver. While it is not possible for conventional underwater vehicles to be deployed from the beach or to be operated in shallow water, it is possible for legged underwater robots. It is not possible, however, for legged underwater robots to navigate the water column above the ocean bottom, which conventional underwater vehicles roam in. AQUA can be deployed from the beach, operate in shallow water and crawl on the ocean bottom like legged underwater vehicles and it can swim underwater like conventional underwater vehicles.

1.4. Literature Review

Extensive studies of the how aquatic animals swim began with Gray's pioneering work in 1935 on the energetics of dolphins swimming [15]. In this study, the force required to propel a dolphin shaped body at typical swimming speeds, was compared to the muscle strength of the animal. Surprisingly, it was shown that the force required is seven fold that of what is available from the muscles of the dolphin. This result, known as the Gray paradox, sparked much research amongst zoologists, scientists, mathematicians and engineers alike. The key findings of this research reveal that aquatic animals can reduce their effect drag by manipulating the vortices shed behind them. By controlling the heaving and pitching movements of their tail fins, they create configurations of the vortices advantageous for propulsion. The observed configuration behind a fish or dolphin is similar to that of a Karman street seen behind a bluff body, except that the polarity of the vortices is reversed. Unlike a Karman street behind a bluff body, which generates a high-speed jet in the direction of the body relative to the rest of the stream (and hence a drag force), the reverse Karman street forms a jet rearward. This high speed jet generates a powerful propulsive thrust that propels the animal forward. Figure 1-13 and Figure 1-14 show the Karman street and the reverse Karman street.

Figure 1-13 (left): Karman street [16]. **Figure 1-14 (right):** Reverse Karman street [17].

The tails of some of the fastest swimming animals resemble high aspect ratio foils. In order to understand the principles of oscillating foil propulsion and apply them to underwater technology, oscillating foils have been studied using analytical, numerical and experimental techniques.

A number of researchers have developed analytical models for the forces generated by oscillating foils. Harper et al. presented a model for oscillating-foil propulsion in which springs are used to transmit forces from the actuators to the foils [18]. Kelly et al.

proposed a model for planar carangiform (tuna-like) swimming based on reduced Euler-Lagrange equations for the interaction of a rigid body and an incompressible fluid [19]. Mason et al. built a three-link robot system to study carangiform-like swimming [20]. They experimentally verified a quasi-steady fluid flow model for predicting the thrust generated by a flapping tail.

M.S.Triantafyllou et al. carried out a review of the experimental work done in biomimetic foils [21]. For steadily oscillating two-dimensional foils, it was determined that pitching-only foils [22], heaving-only foils [23], and heaving and pitching foils [24 and 25] exhibit reverse Karman streets. Figure 1-15 illustrates the pitch and heave of a two-dimensional foil. When two or more foils operate side by side, or when foils operate near a wall or are attached to a vehicle, there are important interaction effects, which may result in a drag wake and deterioration of performance. When a foil operates in the wake of an upstream body, or in the wake of another foil or propeller, the performance of the foil is affected. Sparenberg and Wiersma [26], Koochesfahani and Dimotakis [27], Gopalkrishnan et al. [28], Streitlien et al. [29], and Beal et al. [30] performed theoretical and experimental studies on the interaction of foils with upstream vorticity. Gopalkrishnan et al. identified interactions resulting in substantial increase of efficiency or increase of thrust at the expense of reduced efficiency.

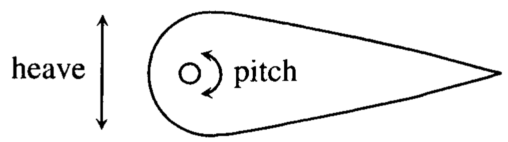

Figure 1-15: Heave and pitch of two-dimensional foil.

Fish fins present great variability in shape, aspect ratio and flexibility. Kemp et al. [31] report experiments with a low-aspect ratio pitching foil, whose propulsive efficiency doubles when the flexibility of the fin is optimized. P. Prempraneerach et al. [32] show experimentally that properly selected chord-wise flexibility can have a significant effect on the propulsive efficiency of two-dimensional heaving and pitching foils (up to 36% compared to the flexibility of a rigid foil).

Numerical techniques have also been used to characterize the forces generated by oscillating fins. Ramamurti used a finite element flow solver based on unstructured grids to study the unsteady flow past oscillating airfoils [33]. Singh et al. used computational fluid dynamics to parameterize the forces generated by a mechanical flapping foil [34]. Mittal et al. used numerical simulations to examine the performance of flapping foils [35]. Mittal states that computational modeling is assuming increased significance in the area of bio-hydrodynamics. However, despite these recent advances, computational modeling of flows in complex bio-hydrodynamic configurations remains a challenging problem [36].

In the mid-nineteen nineties, the oscillating foil was proposed as an alternative to the conventional screw propeller to propel underwater vehicles [37, 38]. The idea that AUVs may propel themselves by flapping their tails like fish was made popular by Triantafyllou et al. through their pioneering work on Robotuna: an 8-link, foil-flapping robotic mechanism [39]. During the past several years, growing interest has developed in the area of design and control of underwater robots that propel and maneuver themselves with fins rather than with a propeller or thrusters. The motivation for this work comes partly from the high maneuverability that fish demonstrate compared to conventional propeller-driven underwater vehicles.

Hobson of Nekton Research LLC et al. state that oscillating fin thrusters (OFTs) are capable of delivering large and sudden amounts of thrust in a controlled fashion [40]. Kemp et al. report that, the magnitude and response time of thrust generated by Nekton's OFTs (when operated in high impulsive force mode) could prove invaluable for emergency stopping or obstacle avoidance. PilotFish, shown in Figure 1-16, is a vehicle with four single actuated degree of freedom foils aimed at demonstrating the capabilities of Nekton's OFTs [41]. Fish et al. discuss the conceptual design of a biomimetic AUV using two sets of four fins having two actuated of freedom each to effect high maneuverability. The biorobotic AUV was to be capable of translating sideways, up and down, and forward and backward. The design of the AUV also was to permit hovering and to maneuver with very small radius turns [42]. A representation of the AUV is shown in Figure 1-17. Licht et al. discuss a biomimetic flapping foil AUV, shown in Figure 1-18, which was designed and constructed as a proof of concept for the use of oscillating foils as the sole source of propulsion and maneuvering forces in an underwater vehicle [43]. Each of the four oscillating foils has two actuated degrees of freedom.


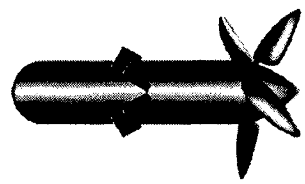
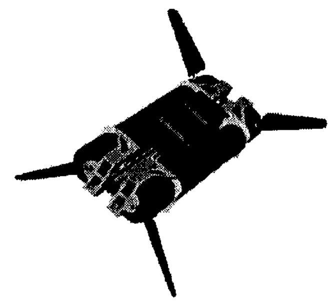

Figure 1-16 (left): Nekton's PilotFish [41]. **Figure 1-17 (middle):** Biorobotic AUV [42]. **Figure 1-18 (right):** Biomimetic flapping foil AUV [43].

1.5. Thesis Motivation and Organization

As stated earlier, one key difference between AQUA and conventional underwater vehicles is AQUA's use of paddles instead of thrusters and control surfaces for propulsion and attitude control. The use of oscillating paddles for propulsion and control represented a novel and challenging problem, which motivated the need for a simulation of the motion of the robot based on its paddle oscillations. The most difficult aspect of this simulation was the characterization of the forces generated by the paddles oscillating in the water. The Harper, Kelly and Mason analytical models [18, 19 and 20] could have been used with some adaptation to represent AQUA's oscillating paddles. These three models were not used because they are quite complicated and a model that could easily be implemented in a simulation was desired.

A model for AQUA's paddles could have been developed based on experiments, but that model would have been valid only for the fin and the set of oscillations that had been tested. It was desired that the model be valid for a paddle of any size undergoing random oscillations. An analytic parametric model for AQUA's paddles was therefore developed and it was validated experimentally. In this work, a model predicting the forces produced by an oscillating rigid paddle was developed and validated experimentally. A simulation of the AQUA robot, which incorporates the validated rigid paddle model, was also developed.

Chapter 2 presents a model to predict the forces generated by an oscillating rigid paddle. Chapter 3 describes the experimental setup, which was designed and built to measure the forces and torques produced by paddles oscillating in the water. The experimental setup was used to collect data allowing validation of the rigid paddle model. The setup was also used to conduct tests with a flexible fin in order to assess how it compared to a rigid paddle. Chapter 4 presents the rigid paddle and flexible fin experimental results. A simulation of the AQUA vehicle was then developed, based on the validated rigid paddle model. Chapter 5 describes the robot simulation and shows results from the simulation.

2. Paddle Model

In the simulation of AQUA, an underwater robot propelled by six oscillating paddles, determination of the forces generated by the paddles presents the greatest difficulty. It has been reported that flexible fins are superior to rigid paddles [44], but they are much more difficult to model analytically than rigid paddles. Hence, as a first solution to the force determination problem, a model of the forces generated by an oscillating rigid paddle was developed. That model is presented in this chapter. The accuracy of the model was gauged by conducting rigid paddle experiments. The setup on which the experiments were performed is described in Chapter 3 and the results of the experiments are presented in Chapter 4.

Section 2.1 discusses the rigid paddle model and explains inflow velocity. Section 2.2 discusses different types of paddle oscillations. Section 2.3 discusses the forces generated by the paddle during oscillation. Section 2.4 discusses an estimate of the inflow velocity for situations, like the rigid paddle experiments, where the paddle operates in stagnant water.

2.1. Rigid Paddle Model

The model for the rigid paddle was based on work done by Healey et al. on the four quadrant dynamic response of conventional AUV thrusters [45]. The authors presented a model of propeller blade lift and drag forces for angles of attack ranging between 0° and 360°. They proposed a formulation for lift and drag coefficients vs. angle of attack, which is shown in Figure 2-1. Few researchers have investigated the lift and drag coefficients of wing sections over the full 360° range of angles of attack. Evans [46] compiled drag and lift coefficient data obtained by Riegels [47] and Critzos [48]. The model of Healey et al., which is in reasonable agreement with Riegels and Critzos' data, was adapted in this work to represent rigid paddle lift and drag forces.

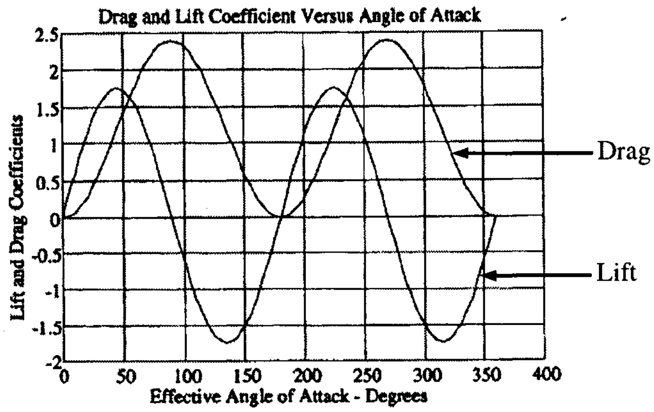

Figure 2-1: Formulation for lift and drag coefficients vs. angle of attack [45]

The scenario of a paddle of length l and width w moving with respect to an inertial frame is considered. Figure 2-2 and Figure 2-3 illustrate the paddle and the inertial frame xyz. The paddle, shown from its side, has a width w into the page and the inertial frame has its y-axis coming out of the page. The paddle is hinged at the origin of the inertial frame and rotates in the xz plane about its shorter edge, which is aligned with the y-axis of the inertial frame. The possibility of the fluid having a velocity with respect to the inertial frame is also considered. That velocity will hereafter be called inflow velocity.

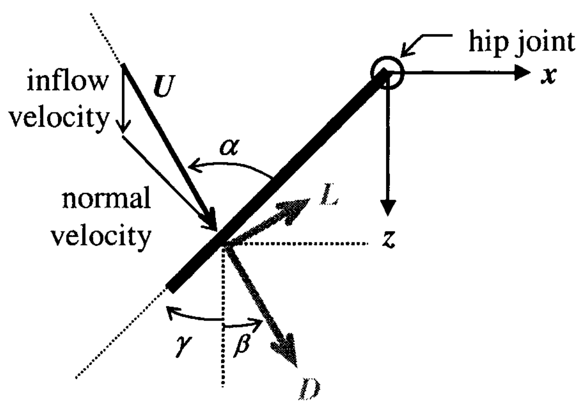

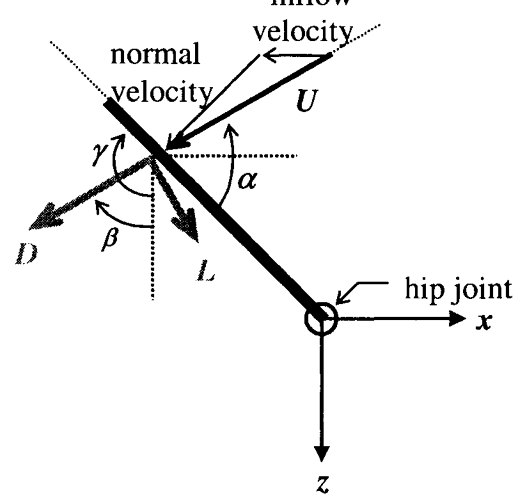

Figure 2-2 (left): Paddle, frame xyz and inflow in rigid paddle experiments. **Figure 2-3 (right):** Paddle, frame xyz and inflow in robot simulation.

In Figure 2-2, which represents the rigid paddle experiments discussed in Chapter 3, the xyz frame coincides with the coordinate frame of the sensor measuring the forces generated by the oscillating paddle and the inflow velocity is aligned with the z-axis. In Figure 2-3, which depicts the robot simulation described in Chapter 5, the xyz frame is attached to one of the six hip joints of the robot with the x-axis pointing towards the front of the robot and the z-axis pointing towards the bottom. The inflow velocity can come from any direction in the plane, but is shown in Figure 2-3 to be coming from the front of the robot.

The normal velocity, shown in Figure 2-2 and Figure 2-3, is due to the paddle motion and is perpendicular to the paddle. It is equal in magnitude and opposite in direction to the velocity of the point on the paddle where lift and drag forces are applied. The location of this point is discussed in Section 5.4.4.1. The flow impinging on the paddle with velocity U is a vector sum of inflow and normal velocities, as shown in Figure 2-2 and Figure 2-3.

The angle β represents the direction of flow impinging on the paddle, relative to the z-axis, while the angle γ represents the angular position of the paddle relative to that axis. Angles β and γ are both positive counter clockwise. Angle γ in Figure 2-2 as well as angles β and γ in Figure 2-3 are therefore negative. The angle of attack α is the direction of flow relative to the paddle and can be calculated as $\alpha = \beta - \gamma$.

A paddle moving through a fluid generates drag and lift forces. As shown in Figure 2-2 and Figure 2-3, the lift force L is perpendicular to the flow impinging on the paddle, while the drag force D is in line with that flow. Lift and drag forces vary with velocity U and angle of attack α as follows [45]:

$$L = 0.5\, \rho\, U^2 S\, C_{L\max} \sin(2\alpha) \tag{2.1}$$

$$D = 0.5\, \rho\, U^2 S\, C_{D\max} \left(1 - \cos(2\alpha)\right) \tag{2.2}$$

where ρ is the density of water, S is the surface area of the paddle, α is the angle of attack and U is the velocity of the flow impinging on the paddle. $C_{L\max}$ and $C_{D\max}$ are the maximum values of lift and drag coefficients of the paddle.

Lift and drag forces can be transformed into forces in the inertial frame of reference, using

$$F_x = D \sin \beta + L \cos \beta \tag{2.3}$$

$$F_z = -L \sin \beta + D \cos \beta \tag{2.4}$$

2.2. Paddle Oscillations

The model presented in Section 2.1 predicts forces generated by the paddle at any instant in time given the paddle angular position and velocity, and the inflow velocity. The paddle angular position γ and velocity $\dot{\gamma}$ are obtained from the paddle trajectory, which is desired to be periodic and differentiable. Two types of curves can be used to characterize this type of paddle motion: the sinusoidal wave and the cubic spline, which are shown in Figure 2-4. The cubic spline is more general in that it can also describe an asymmetric paddle motion. Both types of curves are characterized by three parameters: the amplitude of oscillation *A*, the period of oscillation *T* and the offset angle γ_0. The cubic spline is described by a fourth parameter, the oscillation ratio *R*, which defines the asymmetry.

One oscillation consists of two phases: stroke and recovery. During stroke, the paddle sweeps a given angle in one direction. During recovery, the paddle sweeps the same angle in the opposite direction. The amplitude of oscillation *A* refers to the angle swept by the paddle. The period of oscillation *T* is the time it takes to complete one stroke and one recovery phase of an oscillation. The offset angle γ_0 is the angular position about which the angle swept by the paddle is centered.

The amplitude *A* and the offset angle γ_0 are illustrated for a generic oscillation in Figure 2-5. Oscillations having an offset angle γ_0 of 0°, as illustrated in Figure 2-6, will be considered in Chapters 2 to 4.

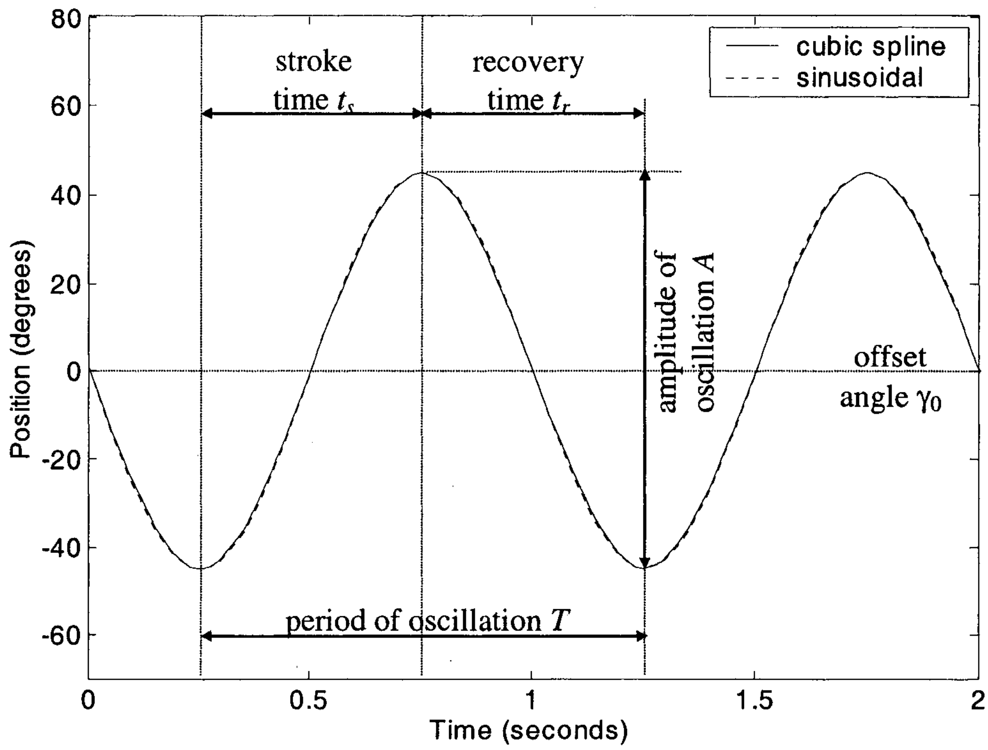

Figure 2-4: Cubic spline and sinusoidal trajectories having an amplitude of oscillation A of 90°, a period T of 1s and an offset angle γ_0 of 0°.

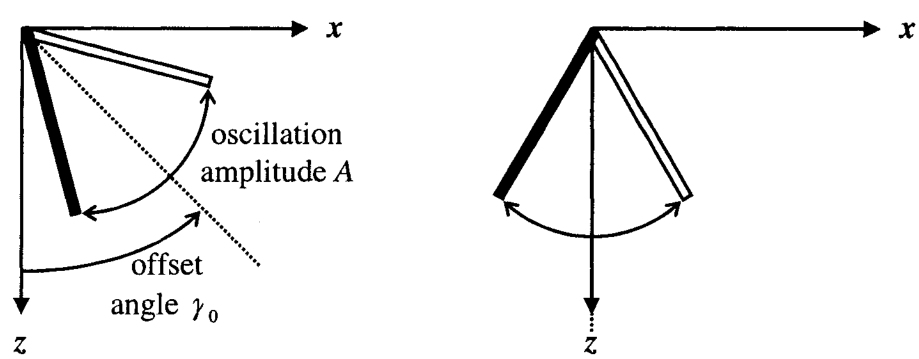

Figure 2-5 (left): Amplitude A and angle γ_0 for a generic oscillation. **Figure 2-6 (right):** Oscillation having an offset angle of 0°.

The cubic spline and sinusoidal trajectories shown in Figure 2-4 have the same parameters. These trajectories are practically identical, the difference between them being in the way they are defined. The sinusoidal trajectory is defined by

$$\gamma(t) = \gamma_0 + A\sin\left(\frac{2\pi}{T}t\right) \tag{2.5}$$

As stated earlier, the cubic spline trajectory is defined by A, T, γ_0 and R. The oscillation ratio R is the ratio of time taken to perform stroke to the time taken to perform the entire oscillation (stroke and recovery).

$$R = \frac{t_s}{t_s + t_r} = \frac{t_s}{T} \tag{2.6}$$

The stroke time t_s and the recovery time t_r were labeled in Figure 2-4. Setting the oscillation ratio to 0.5 results in a symmetric trajectory, in which the stroke time t_s is half the oscillation period T and is equal to t_r. Setting the oscillation ratio below 0.5 results in asymmetric trajectories in which the stroke phase takes place more quickly than the recovery phase. Some examples of asymmetric trajectories are shown in Figure 2-7.

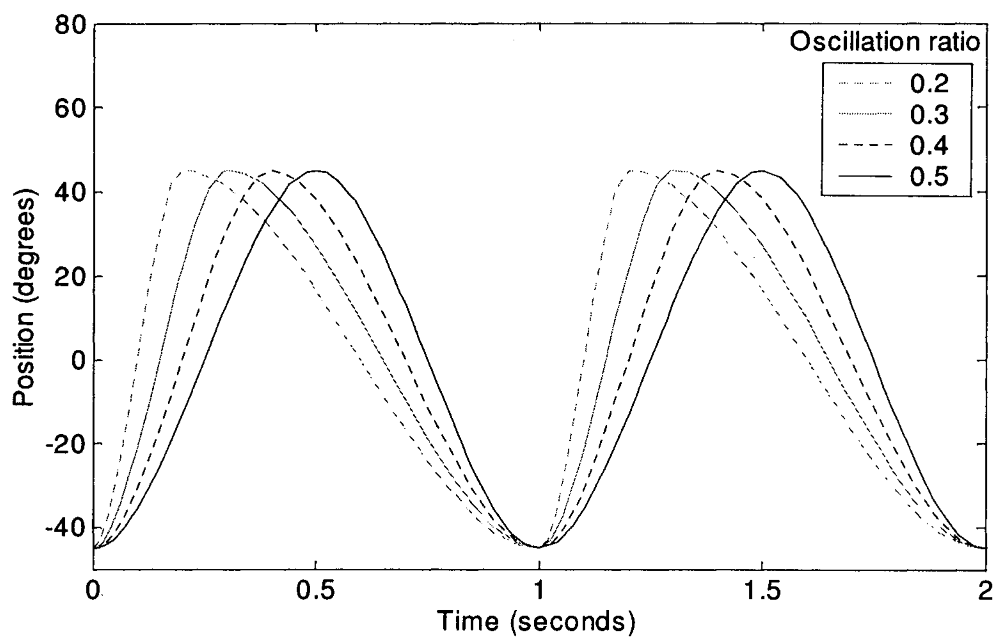

Figure 2-7: Cubic spline trajectories with different oscillation ratios for $A = 90°$, $T = 1$s and $\gamma_0 = 0°$.

Asymmetric trajectories can be desirable in order to investigate more complex paddling motions. The cubic spline trajectory uses a third order polynomial in t to describe the time-varying angular position of the paddle, during each of the stroke and recovery phases. The paddle angular position γ and the paddle angular velocity $\dot{\gamma}$ at time t during each of these phases are given by

$$\gamma(t) = a_0 + a_1 t + a_2 t^2 + a_3 t^3 \tag{2.7}$$

$$\dot{\gamma}(t) = a_1 + 2a_2 t + 3a_3 t^2 \tag{2.8}$$

where t is zero at the start of each phase.

In order to calculate the coefficients a_i, $i = 0,\ldots,3$, the desired boundary conditions at the beginning and end of each phase (stroke or recovery) are used. At the beginning of each phase, t=0 and the following conditions apply:

$\gamma(0) = \gamma_i$ where γ_i is the initial paddle angular position.

$\dot{\gamma}(0) = \dot{\gamma}_i = 0$ where $\dot{\gamma}_i$ is the initial paddle angular velocity, which is equal to 0.

At end of each phase, $t = t_f$ and the following conditions apply:

$\gamma(t_f) = \gamma_f$ where γ_f is the final paddle angular position.

$\dot{\gamma}(t_f) = \dot{\gamma}_f = 0$ where $\dot{\gamma}_f$ is the final paddle angular velocity, which is equal to 0.

After substituting these conditions into equations (2.7) and (2.8), the following expressions were obtained.

$$a_0 = \gamma_i \tag{2.9}$$

$$a_1 = 0 \tag{2.10}$$

$$a_2 = 3\left(\frac{\gamma_f - \gamma_i}{t_f^{\,2}}\right) \tag{2.11}$$

$$a_3 = 2\left(\frac{\gamma_i - \gamma_f}{t_f^{\,3}}\right) \tag{2.12}$$

Substituting these expressions in equations (2.7) and (2.8), results in

$$\gamma(t) = \gamma_0 + 3\left(\frac{\gamma_f - \gamma_i}{t_f^{\,2}}\right)t^2 + 2\left(\frac{\gamma_i - \gamma_f}{t_f^{\,3}}\right)t^3 \qquad (2.13)$$

$$\dot{\gamma}(t) = 6\left(\frac{\gamma_f - \gamma_i}{t_f^{\,2}}\right)t + 6\left(\frac{\gamma_i - \gamma_f}{t_f^{\,3}}\right)t^2 \qquad (2.14)$$

Table 2.1 shows the trajectory parameters (γ_i , γ_f and t_f) for stroke and recovery phases.

Parameters / Phase	γ_i	γ_f	t_f
Stroke	$\gamma_i = \gamma_0 - \frac{A}{2}$	$\gamma_f = \gamma_0 + \frac{A}{2}$	t_s
Recovery	$\gamma_i = \gamma_0 + \frac{A}{2}$	$\gamma_f = \gamma_0 - \frac{A}{2}$	$t_r = T - t_s$

Table 2.1: Parameters (γ_i, γ_f *and* t_f) of equations (2.13) and (2.14) for stroke and recovery phases. *T* is the oscillation period, t_s is the stroke time and t_r is the recovery time.

2.3. Forces Generated During Paddle Oscillations

In this section, forces generated by a paddle following a cubic spline trajectory will be shown. Figure 2-8 shows a symmetric trajectory for which A = 90°, T = 1s and γ_0 = 0°. It also shows the lift and drag forces generated by a paddle following that trajectory in the absence of inflow. The paddle has l = 0.2m, w = 0.05m, $C_{L\max}$ = 0.92 and $C_{D\max}$ = 1.12 [49] .

When there is no inflow, the velocity term U in the equations for lift and drag in equations (2.1) and (2.2) comes solely from the normal velocity of the paddle. When that happens, the angle of attack is 90° and lift is equal to 0 throughout the trajectory, as shown in Figure 2-8.

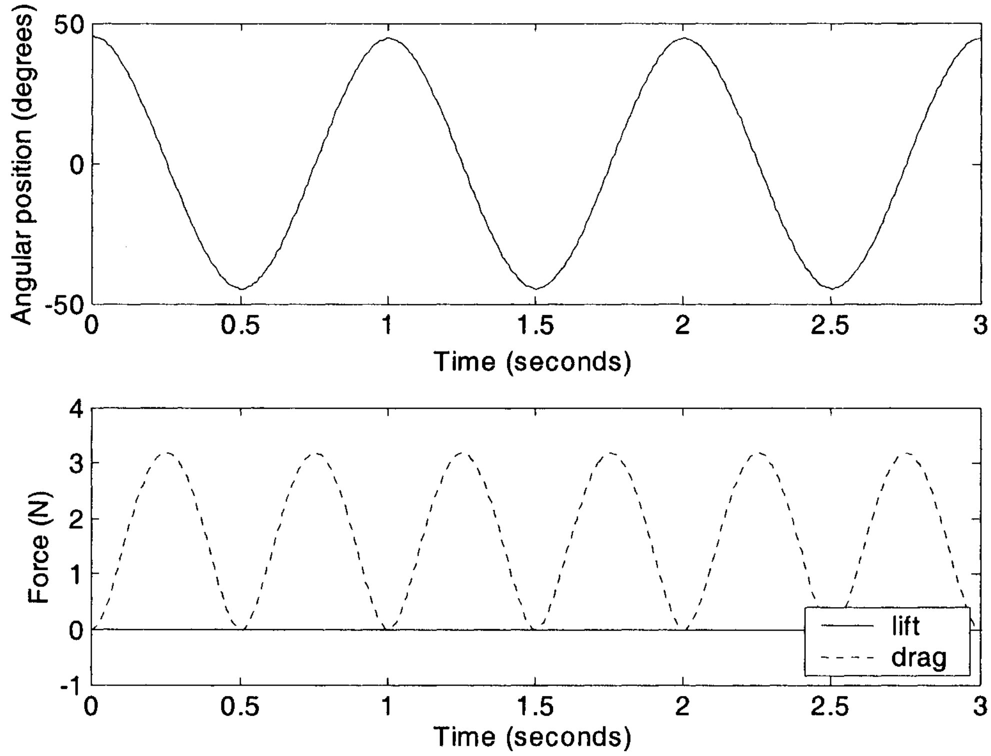

Figure 2-8: Lift and drag forces generated by a paddle following a symmetrical cubic spline trajectory in the absence of inflow.

As explained earlier, lift and drag forces are calculated in a coordinate frame aligned with the flow impinging on the paddle, and the forces are then transformed into the inertial frame of reference. If the offset angle is 0°, as shown in Figure 2-6, forces along the z-axis are parallel to the offset angle direction and forces along the x-axis are perpendicular to that direction. The forces along the z-axis will hereafter be called parallel forces and the forces along the x-axis will be called perpendicular forces. Figure 2-9 shows the instantaneous parallel and perpendicular forces obtained by transforming the lift and drag forces of Figure 2-8. Figure 2-9 also shows the parallel and perpendicular impulses, which are also of interest. The impulse is the integral of a force over time. Ideally, the parallel impulse should continually increase during a series of oscillations in order for net thrust to be produced. The perpendicular impulse should be zero after one oscillation or a series of oscillations so that no side force is produced. In Figure 2-9, the parallel and perpendicular impulses are both zero at the end of each oscillation. This indicates that no net thrust or side force is produced. Force cancellation occurs when forces generated during stroke are equal and opposite to forces generated during recovery. This happens when a paddle follows any symmetric trajectory in the absence of inflow.

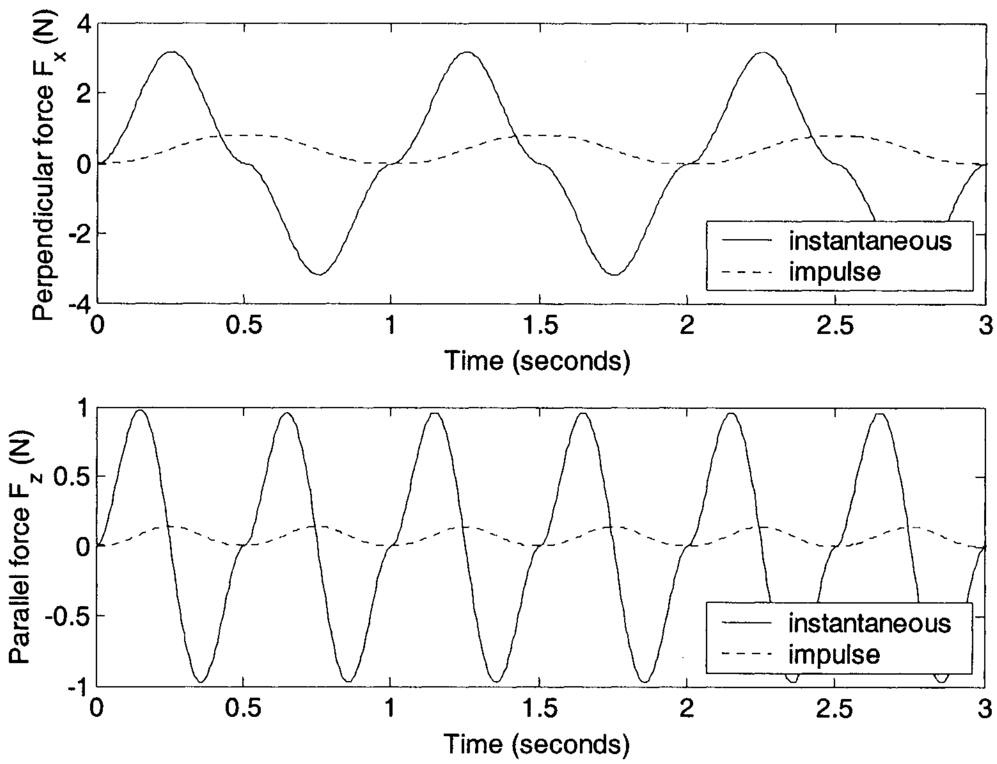

Figure 2-9: Parallel and perpendicular forces generated by a paddle following a symmetrical cubic spline trajectory in the absence of inflow.

2.4. Estimation of Inflow

As shown in Section 2.3, a paddle performing a symmetric oscillation in a fluid with zero inflow velocity produces no thrust. However, as will be shown in this section, a paddle oscillating symmetrically in a fluid with non-zero inflow velocity does produce useful thrust. In order to gauge the accuracy of the rigid paddle model described in Section 2.1, experiments were conducted in a stagnant tank. Even in a stagnant tank, the paddle entrains water during oscillation and there is inflow. In order to compare experiments with rigid paddle simulations, inflow needed to be quantified. Since inflow was not measured during the experiments, a method to estimate it had to be devised.

The inflow estimate is based on the premise that flow is created as water in front of the oscillating paddle moves to replace the volume of water displaced by the paddle. The rate at which the volume of water is displaced by the paddle during sweep or recovery corresponds to the rate at which water flows towards the paddle through a cross-section, which is equal to half the frontal area of the volume swept by the paddle. The water cannot flow through the other half of the area, which is blocked by the paddle. In mathematical terms:

$$\frac{V_d}{T/2} = A_f \; v \tag{2.15}$$

where V_d is the displaced water volume, $T/2$ is half the period of oscillation, A_f is the frontal area of the paddle and v is the inflow velocity. The displaced volume V_d and the frontal area A_f can be obtained by geometry using Figure 2-10.

$$V_d = w \, \pi \, l^2 \left(\frac{A}{2\pi} \right) \tag{2.16}$$

$$A_f = \sin\left(\frac{A}{2} \right) w \, l \tag{2.17}$$

where w is the width of the paddle, l is its length and A is the oscillation amplitude in radians.

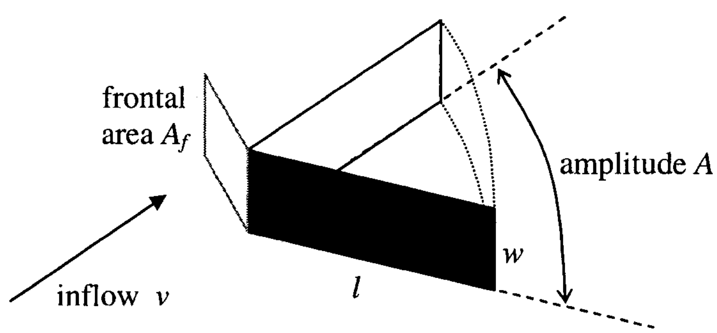

Figure 2-10: Diagram showing the volume swept by paddle and the frontal area of the paddle.

Substituting equations (2.12) and (2.13) in equation (2.11) allows to solve for v

$$v = \frac{l \, A}{T \, \sin\left(\frac{A}{2} \right)} \tag{2.18}$$

The variation of inflow velocity with A and T is shown in Figure 2-11. The inflow is inversely proportional to period and only weakly dependent on amplitude. The dependence of v on amplitude is not strong because the ratio $\frac{A}{\sin\left(\frac{A}{2}\right)}$ only varies from 2 to 2.2 as amplitude is varied from 0 to $\pi/2$. It must be emphasized that v is a crude approximation of the complex flow that results from paddle motion. Using equation (2.15), an inflow velocity of 0.44m/s is found for the case of a 0.20m long paddle undergoing the symmetric trajectory for which $A = 90°$ and $T = 1$s.

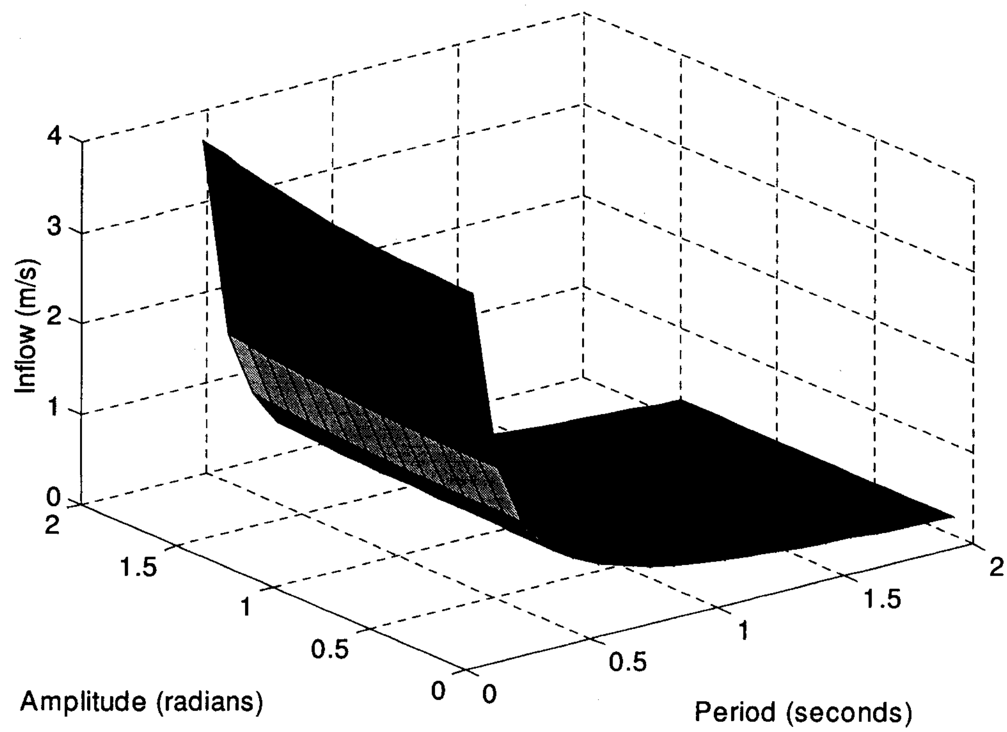

Figure 2-11: Estimate of inflow as a function of period and amplitude of oscillation for a 0.20m long paddle.

The lift and drag forces generated by a paddle following a symmetric trajectory for which for which $A = 90°$, $T = 1$s and $\gamma_0 = 0°$ in the presence of inflow are shown in Figure 2-12, while the corresponding parallel and perpendicular forces are shown in Figure 2-13. The paddle has $l = 0.2$m, $w = 0.05$m, $C_{L\max} = 0.92$ and $C_{D\max} = 1.12$. It can be seen in Figure

2-13 that the parallel impulse at the end of each oscillation is non zero while the perpendicular impulse is again equal to zero. Practically, this means that, in the presence of inflow, there is a net thrust but no net side force.

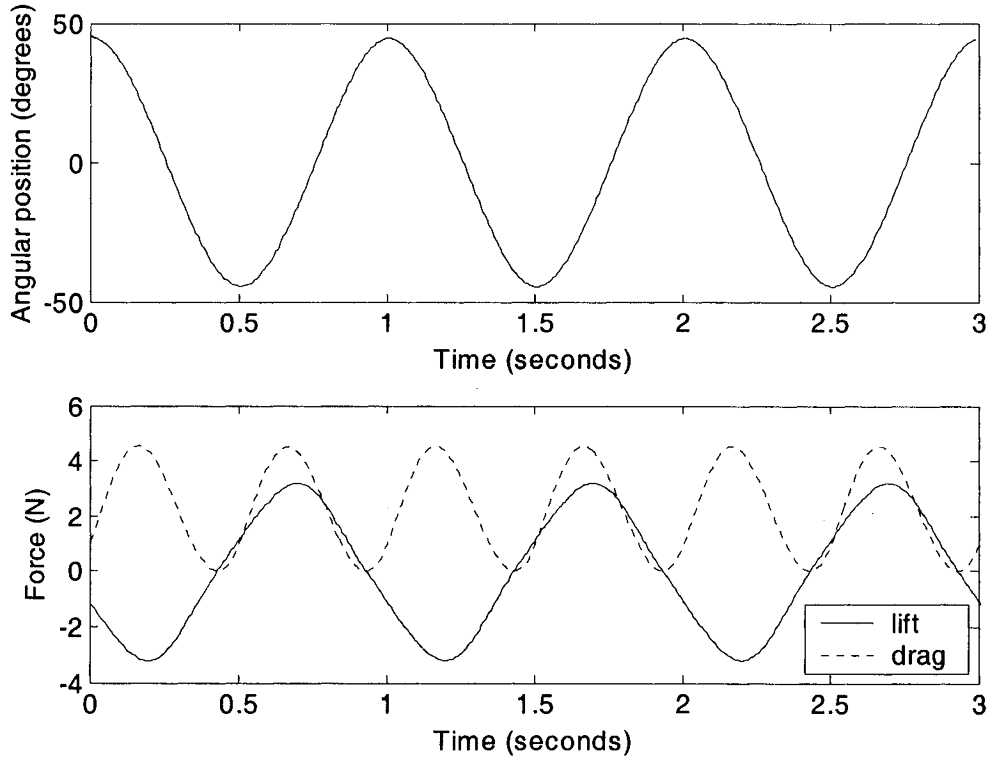

Figure 2-12: Lift and drag forces generated by a paddle following a symmetrical cubic spline trajectory in the presence of inflow of 0.44m/s.

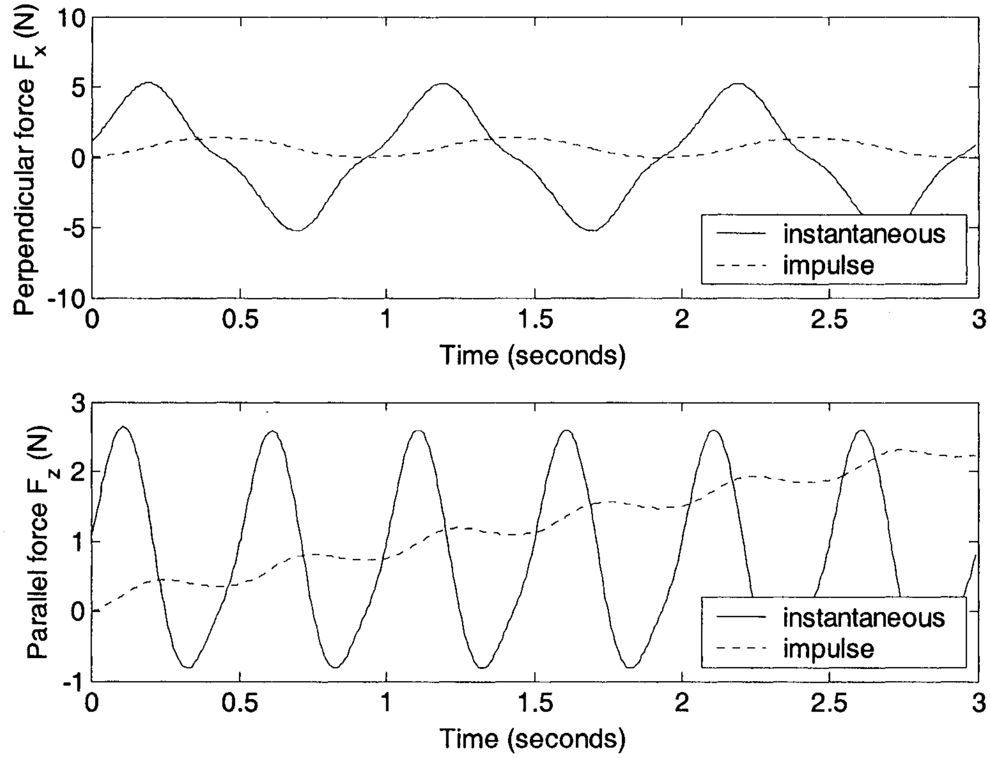

Figure 2-13: Parallel and perpendicular forces generated by a paddle following a symmetrical cubic spline trajectory in the presence of inflow of 0.44m/s.

As will be explained in Chapter 5, in the vehicle simulation, which incorporates the rigid paddle model, the inflow velocity is assumed to be the advance velocity of the paddle through the surrounding fluid. The rigid paddle model implies that the faster the vehicle moves through the water, the more thrust the paddle generates. By contrast, conventional thrusters typically generate less thrust as their advance velocity increases.

3. Thrust Measuring Setup

The Thrust Measuring Setup (TMS) is an experimental facility for measurement of forces and torques generated by an oscillating paddle. The TMS was designed to allow validation of the rigid paddle model presented in Chapter 2 and to support later development of models for flexible fins. It was constructed so that different paddles and modes of oscillation can be tested on it. This chapter discusses the design and assembly of the TMS, its main components and its experimental interface.

Thrust measuring experiments were conducted in a stagnant tank having a length of 6m, a width 1.5m and a depth of 1.2m. The TMS in the tank is illustrated in Figure 3-1. The paddle oscillates in a plane 0.15m below the water surface, while a sensor measures the forces and torques generated by the oscillating paddle. Measurements of greatest interest are the forces in the plane of oscillation and the torque about the axis perpendicular to that plane.

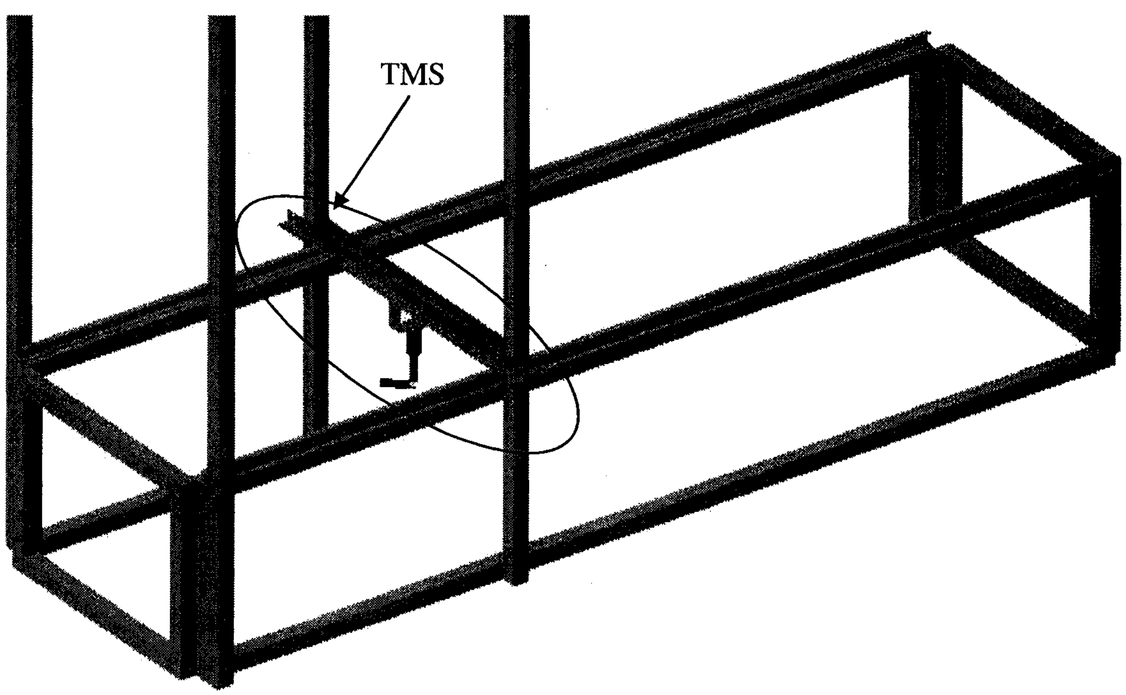

Figure 3-1: CAD drawing of TMS in tank

The high-level layout of the TMS is shown in Figure 3-2. The main components are:

- Paddle unit:
  - Paddle under test
  - Maxon motor stack: motor, gearbox and encoder
  - ATI Force/Torque sensor and its power supply
- Electronics:
  - National Instruments Data Acquisition Card (DAC) and breakout box
  - AMC Amplifier and Filter card
  - 48V and 5V DC power supplies
  - Quadrature encoder decoder (inside breakout box)
- Personal computer running LabVIEW software for the graphical user interface.

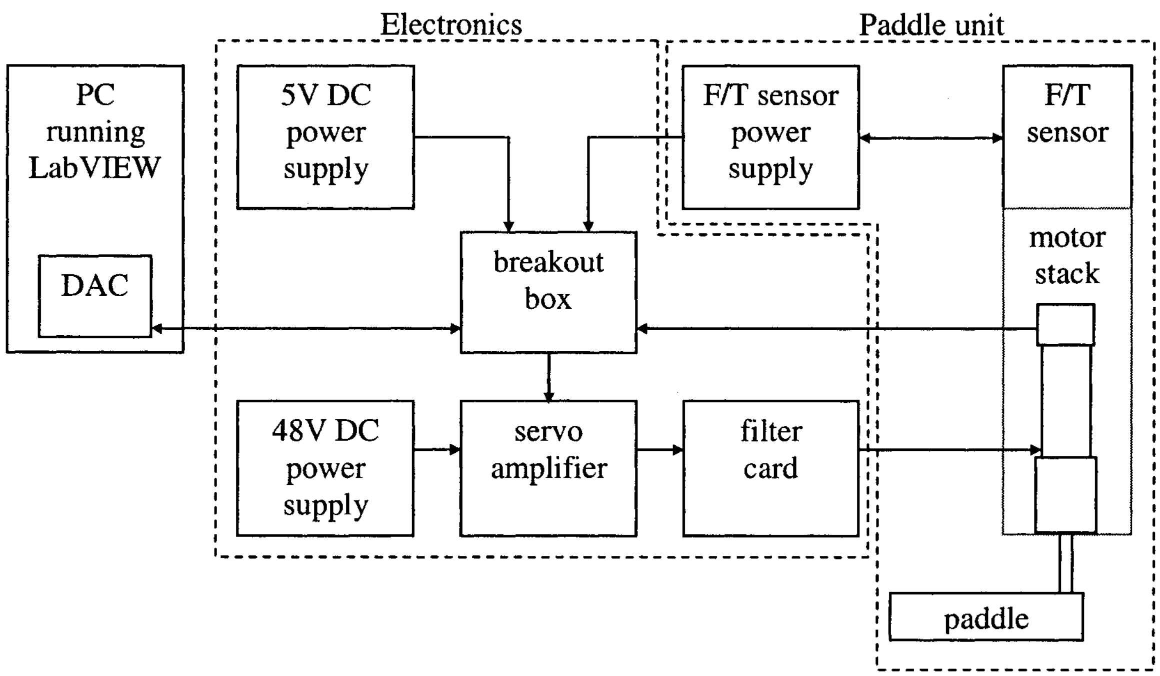

Figure 3-2: High-level layout of TMS

The considerations relevant to testing paddles in a stagnant tank are discussed in Section 3.1. The structure of the TMS is discussed in Section 3.2. The paddle unit is discussed in Section 3.3, the electronics of the TMS are discussed in Section 3.4 and the experimental interface is described in Section 3.5.

3.1. Tests in Stagnant Tank

Figure 3-3 and Figure 3-4 illustrate the position of the paddle relative to the walls of the tank. They show only the first 3meters of the 6m long tank. Figure 3-3 and Figure 3-4 also show the *xyz* frame attached to the force/torque sensor. Axes *x*- and *z*- coincide with the *x*- and *z*- axes of the model presented in Chapter 2. It was conjectured that the tank is large enough that effects such as turbulence, recirculation and slosh would not affect experimental measurements. The water entrained by the oscillating paddle was estimated in Chapter 2. Measuring entrained flow would have eliminated the need to estimate it. It is recommended to add a flow velocity sensor on the thrust measuring setup for future experiments. It is well known that results obtained for a forward-moving thruster would be quite different. Future tests in a tow tank would therefore be useful to better understand the thruster effectiveness in a moving vehicle.

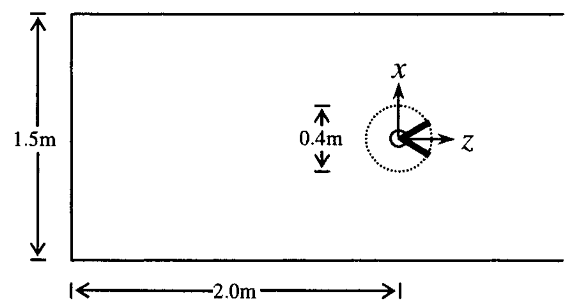

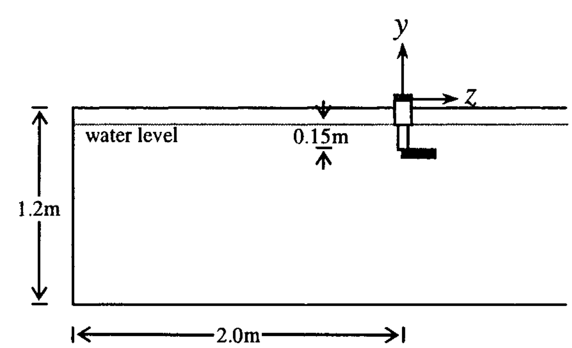

Figure 3-3 (left): Top view of the paddle in the tank. **Figure 3-4 (right):** Side view of the paddle in the tank.

3.2. TMS Structure

The three hip joints on either side of AQUA are aligned, and the middle and rear paddles oscillate in the turbulent flow created by the oscillation of the front paddle. Initially, it was considered to oscillate three paddles in a tank and measure the forces and torques produced by each paddle. Due to budgetary constraints and for the sake of simplicity, it was decided to start by testing only one paddle. The following subsections discuss the design of the thrust measuring setup and the test structure's natural frequencies.

3.2.1. Design Considerations

Many issues needed to be considered in designing the thrust measuring setup. The setup was attached to the tank's two central vertical beams using a single brace across the width of the tank. Other options considered would have been less rigid. Figure 3-5 shows the attachment of the setup on the tank's vertical beams. It does not show the rest of the tank for the sake of giving an unobstructed view of the setup.

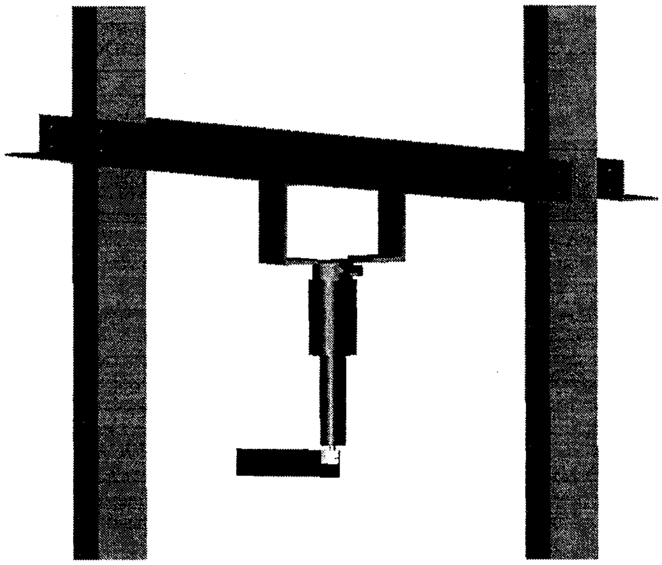

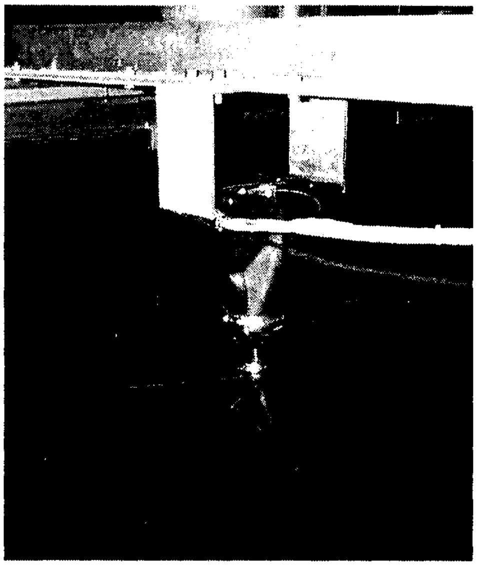

Figure 3-5 (left): CAD drawing of TMS. **Figure 3-6 (right):** Picture of TMS in the tank

In order for the sensor to properly measure forces and torques, the sensor had to be mounted between the structure, which was attached to the tank, and the paddle unit, which was partly in the water. In order to simplify the design, the force/torque sensor was kept out of the water and was protected from splashes by a cover as shown in Figure 3-6.

The surface of the water was roughly 0.28m below the point of attachment of the structure on the vertical beams. In deciding how deep to position the paddle in the water, two issues needed to be considered. On one hand, the paddle needed to be submerged deep enough that surface effects would not affect the results. On the other hand, the paddle needed to be positioned close enough to the force/torque sensor that moments resulting from paddle forces would not exceed the moment ratings of the sensor. When the paddle oscillated 0.15m below the water, no ripples could be seen at the surface. At that position, the distance between the paddle and the sensor would be 0.43m or less, depending on the position of the sensor. Based on the forces predicted by the rigid paddle model and the moment ratings of the force/torque sensors available on the market, it was determined that positioning the paddle 0.15m under the surface of the water was acceptable. This is explained further in Section 3.3.3.

3.2.2. Natural Frequencies of the Test Structure

In preliminary experiments, it was found that some high frequency oscillations were present in the data. It was conjectured that these were due to vibrations of the test structure. The natural frequencies of the thrust measuring setup were therefore measured by conducting an impact test on the structure. The impulse response of F_z, the force along the z-axis of the sensor, can be seen in Figure 3-7. From that plot, a dominant damped frequency of 15.7Hz was found. The same frequency was found from a plot of the impulse response of F_x, the force along the x-axis of the sensor. The impulse response of F_y, the force along the y-axis of the sensor, can be seen in Figure 3-8. From that plot, a dominant damped frequency of approximately 48Hz was found.

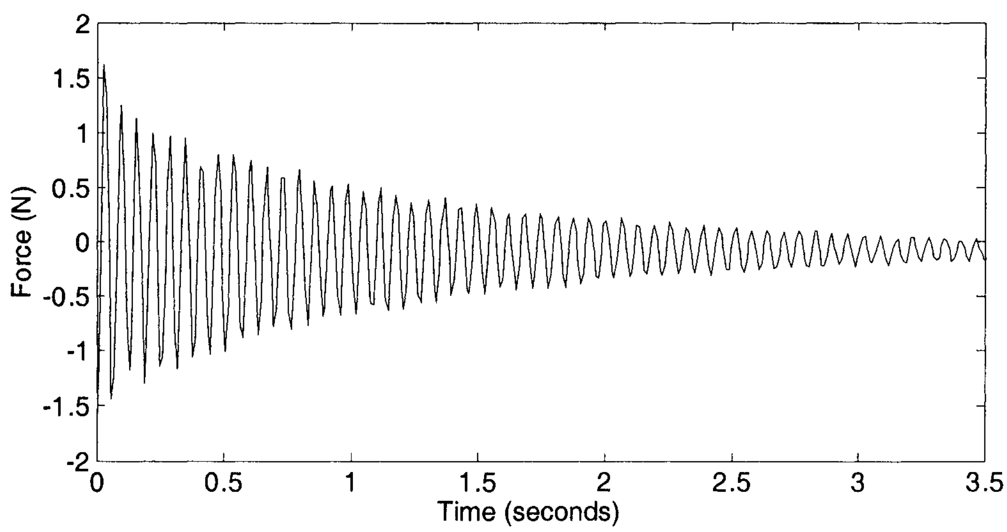

Figure 3-7: Impulse response of Fz, the force along the z-axis of the sensor.

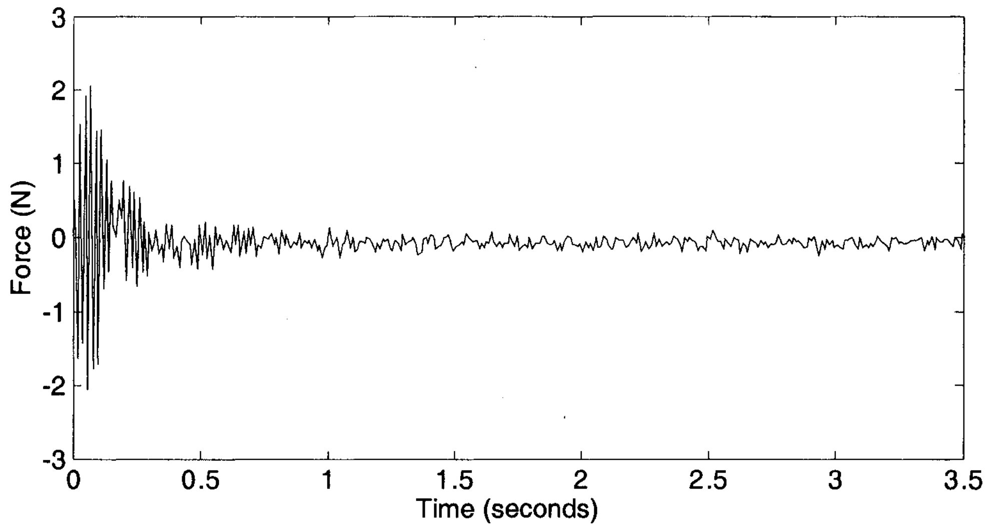

Figure 3-8: Impulse response of Fy, the force along the *y*-axis of the sensor.

The damping ratio ζ is found via the logarithmic decrement δ [50], which is estimated from the plot of Figure 3-7. The decrement is measured over multiple cycles for better accuracy. The first and the thirty-second peaks are 1.6185N and 0.1938N. Therefore,

$$\delta = \frac{1}{(32-1)} \ln\left(\frac{1.6185}{0.1938}\right) = 0.068 \tag{3.1}$$

The damping ratio ζ is equal to the logarithmic decrement divided by 2π, and is thus equal to 0.0108.

The system is very lightly damped. An attempt was made to increase the damping of the vibrations of the thrust measuring setup by adding rubber between the TMS crossbrace and the square cross-section beams on which the setup is attached. Rubber was also inserted between the force/torque sensor and the plate that it is mounted on. Both additions made no significant difference in the damping ratio of the setup. A recommendation is made to stiffen the setup in the future. This can be done by adding members, which will prevent the cross brace supporting the sensor from bending or twisting.

3.3. Paddle Unit

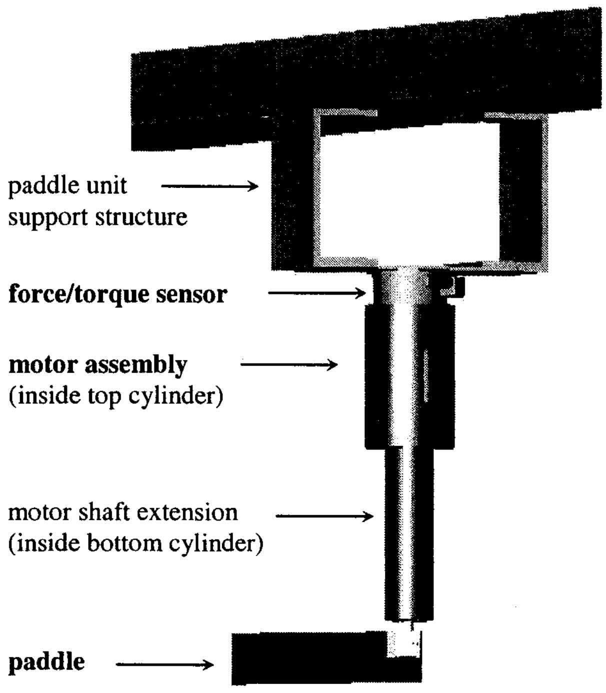

Figure 3-9: CAD drawing of paddle unit.

The leg unit is comprised of the paddle under test, the motor assembly (motor, gearhead and encoder) and the force/torque sensor. As shown in Figure 3-9, the paddle under test is attached at the end of the motor shaft extension, which protrudes from the bottom cylinder. The motor assembly is enclosed in the top cylinder. The sensor is mounted between the top cylinder and the paddle unit support structure. This section discusses each of the three components of the paddle unit.

3.3.1. Paddle

The rigid and semi-rigid paddles as well as the flexible fins that were tested on the TMS are shown in Figure 3-10. The rigid paddle was tested to validate the model presented in Chapter 2. The other fins were tested to determine the paddle to be used on the robot. Results of rigid paddle experiments are given in Chapter 4. Also, in that chapter, a comparison of the results obtained for the rigid paddle and for the flexible fin that was chosen for the robot is presented.

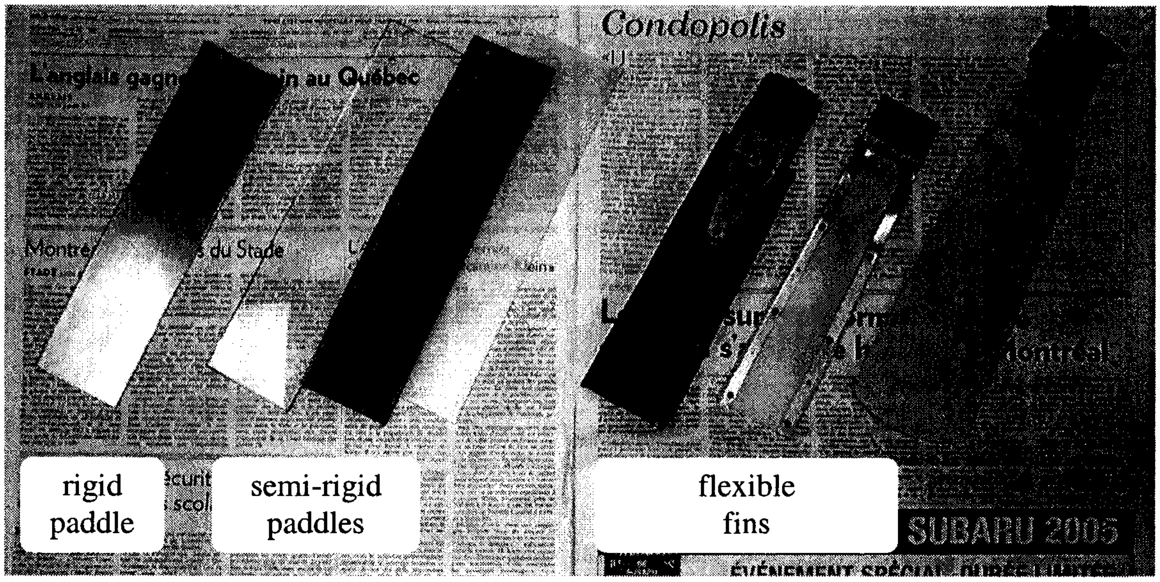

Figure 3-10: Rigid and semi-rigid paddles, and flexible fins. All paddles, except the rigid paddle, were developed by Shane Saunderson at the Ambulatory Robotics Laboratory.

3.3.2. Motor Assembly

While the TMS was being designed and built, AQUA was also being constructed. RHex has 18V, 20W, graphite-brushed DC motors (Maxon RE 25 series, number 118751) and 33:1 reduction ratio gearheads (Maxon GP 32 A, number 166163). The RHex motor stack has a maximum torque of 5.45Nm and a maximum speed of 309rpm. AQUA was going to have 42V, 20W, graphite-brushed DC motors (Maxon RE 25 series, 118754) and the same 33:1 reduction ratio gearheads. The AQUA motor stack has a maximum torque of 7.00Nm and a maximum speed of 336rpm. Data sheets for the two motors and the gearhead can be found in Appendix A.

At the time when TMS tests were scheduled, a RHex motor stack was available, but an AQUA motor stack was not. In simulation, the RHex motor stack seemed capable of delivering enough torque for all oscillations to be tested. It was therefore decided to perform the tests with the RHex motor, but to design the motor enclosure of the TMS so that experiments could be performed with the AQUA motor at a later time, if desired. The mounting pattern of both motor stacks is identical, but the AQUA stack is longer than the RHex stack. The motor enclosure was made long enough so that either motor stack can fit inside it.

3.3.3. Force/Torque Sensor

Moment capacity was the determining factor in choosing the best force/torque transducer for the TMS. The rigid paddle model predicted maximum forces of 20N. Based on that and the fact that the point of application of the force would be less than but close to 0.5m, a force/torque sensor able to handle up to 10Nm of torque was required. ATI's Gama SI 130-10 was used to measure the forces and torques generated by the oscillating paddle. It is capable of measuring torques of 10Nm and forces of 130N. The data sheet for the force/torque sensor can also be found in Appendix A.

3.4. Electronics

The Electronics of the TMS are comprised of a National Instruments Data Acquisition Card (DAC) and breakout box, an amplifier, a filter card, 48V and 5V DC power supplies and a quadrature encoder decoder. The DAC resides in the computer. All the other components are shown in Figure 3-11.

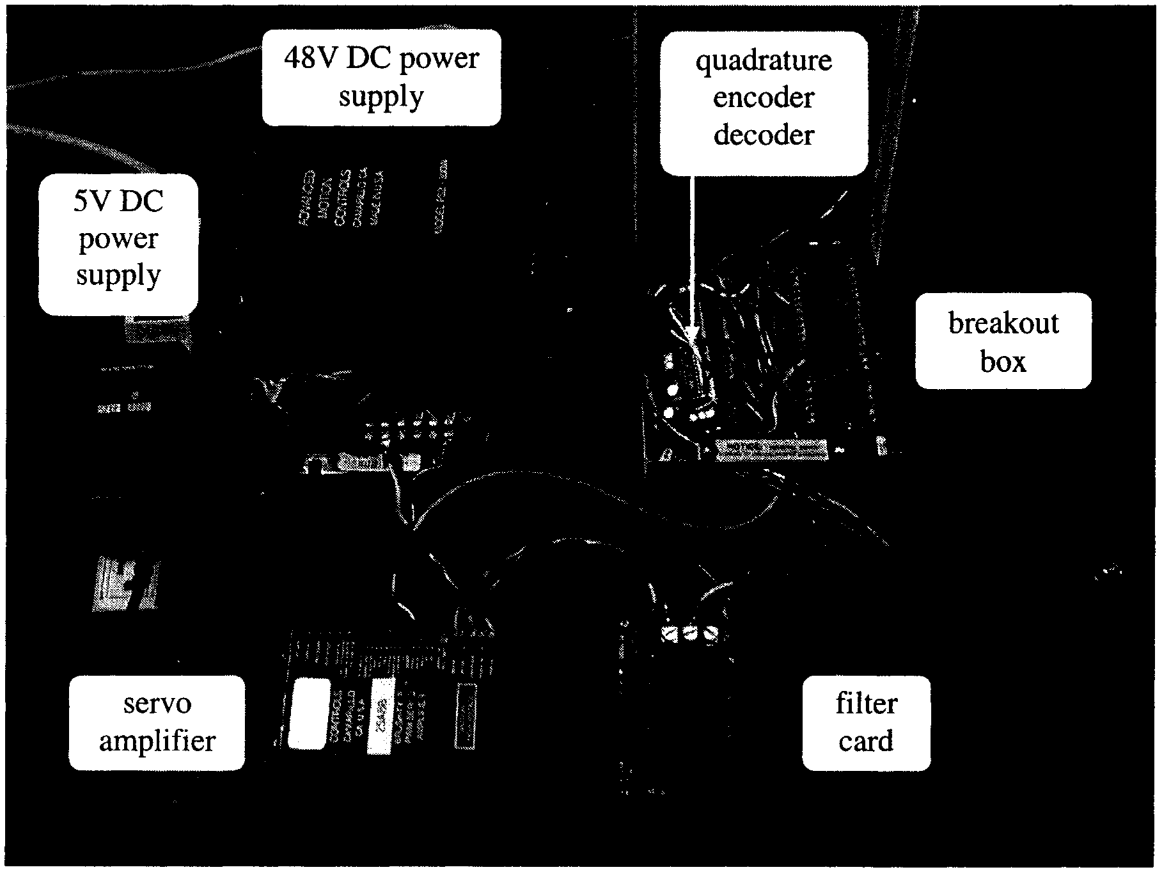

Figure 3-11: Electronics of TMS.

3.4.1. Motor Amplifier and Filter Card

Advanced Motion Controls' 25A8B amplifier and FC15030 filter card were used to drive the TMS motor stack. The 25A Series PWM servo amplifiers are designed to drive brush type DC motors. They require only a single unregulated power supply of 20 to 80V. The amplifier can supply the motors a peak current of 25 A, which is more than the starting current of the RHex and AQUA motors, and a maximum continuous current of 12.5A, which is also more than the continuous current of the two motors.

The amplifier's minimum load inductance is 200μH. The terminal inductance of the RHex motor is only 120 μH. The FC15030 filter card is designed to complement Advanced Motion Controls servo amplifiers and it is used to increase load inductance. This is typically necessary with some types of motors (e.g. basket-wound, pancake), which do not have a conventional iron core rotor and thus have a winding inductance that is usually less than 25μH. The 300 μH inductance on the card is adequate to meet the minimum load inductance requirements of the 25A8B amplifier.

3.4.2. Data Acquisition and Control

The National Instruments PCI-6035E was used in the thrust measuring setup to acquire experimental data and to give motor control commands. This data acquisition card (DAC) features sixteen single-ended or eight differential 16-bit analog inputs and two 12-bit analog outputs. Depending on the hard drive, the PCI-6035E can stream to disk at rates up to 200 kS/s. The SCB-68 is a shielded connector block with 68 screw terminals for easy connection to National Instruments products, such as the PCI-6035E card. Inputs to the DAC, such as measured forces and torques as well as encoder readings, were routed through the SCB-68 breakout box shown in Figure 3-2. Outputs of the DAC, such as reference signals of the amplifier, were also channeled through that same breakout box.

3.4.3. Quadrature Encoder Decoder

Agilent Technologies' HCTL-2020 chip was used to decode the signals generated by the quadrature encoder. It outputs increments or decrements in position. Paddle position is obtained by summing these. Paddle velocity is obtained by dividing changes in position by time increments between position readings.

3.4.4. Power Supplies

Two DC power supplies were used. The first one was Advanced Motion Controls' PS2x300W Series Power Supply. This unregulated power supply, which has been designed to complement Advanced Motion Controls' servo amplifiers, provided 48V to the 25A8B amplifier. This voltage can drive the 18V RHex motor as well as the 42V AQUA motor. The second power supply used in the TMS was an AC/DC converter outputting 5V. The 5V output was used to power the quadrature encoder decoder.

3.5. Experimental Interface

The goal of the experiments is to measure the forces and torques generated by a paddle as it oscillates in the water. The acquisition of the experimental data and the control of the paddle are done by a program created in LabVIEW. Before performing the oscillations, the program calibrates the paddle by doing an angular sweep of 360° until a Hall effect sensor is triggered. This calibration is done to position the paddle accurately relative to the force/torque sensor coordinate frame. Once the paddle is positioned, it starts following a trajectory for a length of time or number of cycles specified by the user.

3.5.1. PD Controller in GUI

The torque command sent to the paddle motor was generated by a PD controller, based on the errors in the paddle's angular position and angular velocity.

The paddle angle PD torque controller generates a torque command according to

$$\tau = K_p(\gamma - \gamma_d) - K_v(\dot{\gamma} - \dot{\gamma}_d) \qquad (3.2)$$

where γ is the angular position of the paddle, γ_d is the desired angular position of the paddle, K_p is the proportional gain, $\dot{\gamma}$ is the angular velocity of the paddle, $\dot{\gamma}_d$ is the desired angular velocity of the paddle and K_v is the derivative gain.

In the experiments, the desired paddle angular position γ_d is generated from the cubic spline presented in equation (2.5). The desired paddle angular velocity $\dot{\gamma}_d$ is the derivative of γ_d and is the second order polynomial presented in equation (2.6). The K_p

and K_v gains were tuned by the user in order to obtain the best possible tracking of the desired trajectory.

3.5.2. Graphical User Interface

The program for data acquisition and motor control was written in National Instruments LabVIEW software. By connecting block diagrams of the virtual instrument (VI) libraries that come with LabVIEW as well as those supplied with the ATI Force/Torque sensor, a graphical user interface (GUI) was constructed. Figure 3-12 shows the LabVIEW GUI developed for the TMS.

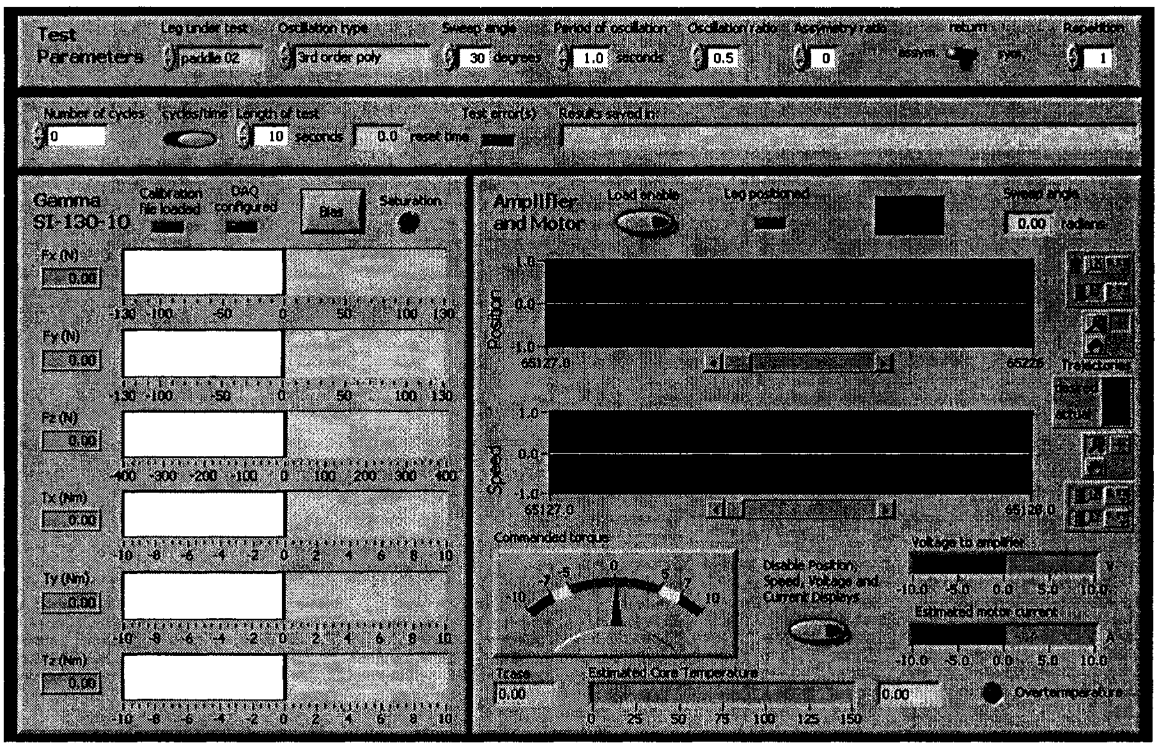

Figure 3-12: LabVIEW GUI developed for the TMS.

Through pull-down menus, the GUI enables the user to select certain test parameters. Each paddle tested on the TMS was named, and that name was written in the title of the experiment. The oscillation types that can be selected are sinusoidal, cubic spline, square wave and 360°. The type of trajectory is also embedded in the name of the file.

Through various entry fields in the GUI, the user can set additional parameters: the test length or the number of oscillations, the amplitude of oscillation (defined as the peak-to-peak magnitude), the period of oscillation and the oscillation ratio. All these parameters are also integrated in the name of the file where the results are saved, so that it is easy to link a particular file to the corresponding test conditions.

During experiments, the GUI displays real time test information, enabling the user to monitor results and to detect errors. Progress bars display the force and torque measurements, the voltage sent to the amplifier, the estimated motor current and the estimated motor core temperature. The estimated motor core temperature is based on a paper written by two colleagues at the Ambulatory Robotics Lab [51]. Charts compare the paddle position and velocity to the corresponding desired values. A dial displays the torque commanded to the motor. Finally, LEDs toggle when the motor has reached a critical temperature of 125°C or when one of the forces or torques has exceeded the force/torque sensor's ratings.

The GUI gives the user access to various functions such as biasing the F/T sensor and enabling the motor. Pushing the Bias button resets all force and torque measurements, so that static forces and torques acting on the sensor do not appear in the force and torque measurements. After the load is enabled, the paddle calibrates and starts oscillating. If problems arise, the user can disable the load or push an emergency stop button, which terminates the experiment. The user can also turn off the position, speed, voltage and current displays. Since graphic indicators consume processing time, it is usually better to turn off the graphical displays and instead read the digital displays, thus allowing iteration loops to be completed in a more timely manner.

The program in LabVIEW was designed to acquire sensor readings at frequencies of 100 S/s. Figure 3-13 shows how the actual iteration times varied from the set 0.01 second. The greatest problem with LabVIEW was related to unsynchronized occurrence of events and unequal iteration times. During a given time step, the encoder and time readings did not occur simultaneously. As a result, the paddle velocity calculated from these readings was noisy. Noise on velocity resulted in noisy commanded torque for values of the PD controller derivative gain that were not very near zero. Unequal iteration times contributed to instability of the PD controller because the torque was applied at intervals of time that were different from the set iteration time.

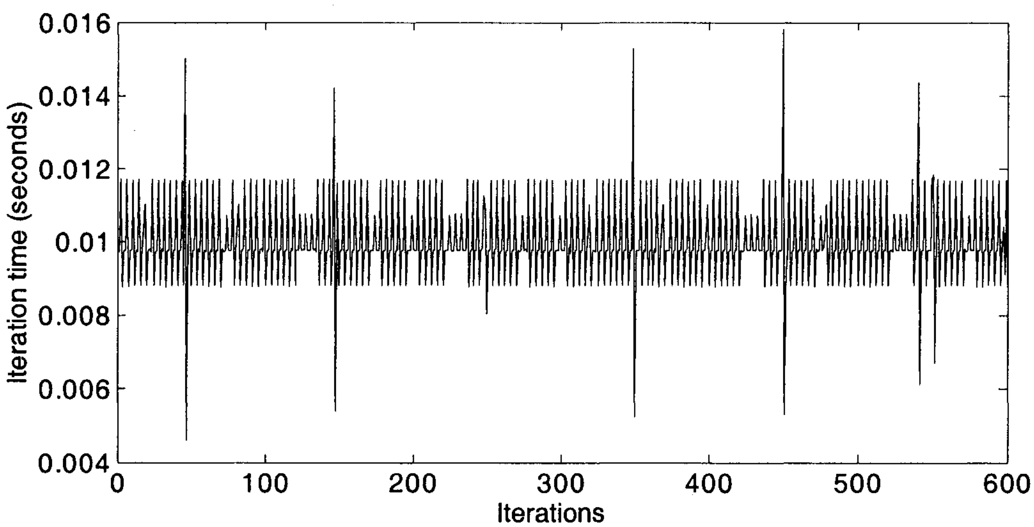

Figure 3-13: Iteration times of a thrust measuring setup experiment. These should be constant at 0.01s, but deviate from that.

4. Thrust Measurement Experiments

Experiments were performed on the thrust measuring setup described in Chapter 3 with a rigid paddle in order to validate the rigid paddle model presented in Chapter 2. Tests were also performed with various flexible fins. In this chapter, the results of the rigid paddle experiments are presented and compared to the results of the rigid paddle model. Also, the forces generated by a flexible fin are compared to those produced by the rigid paddle.

4.1. Rigid Paddle

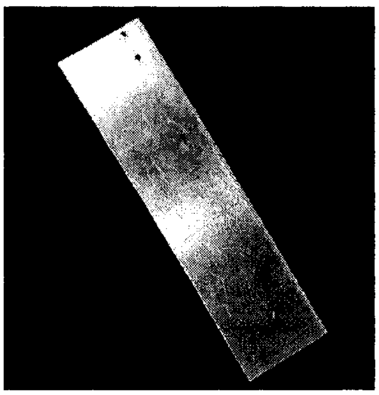

Figure 4-1: Rigid paddle

Rigid paddle experiments were performed by mounting the 20cm long, 5cm wide and 3.2mm thick aluminum flat plate, illustrated in Figure 4-1, on the TMS and oscillating it at different periods and amplitudes. This section describes the experiments that were performed, the problems that were experienced in controlling the paddle, and the conditioning and analysis of the measured data. Also, this section displays the results of the rigid paddle experiments and compares them to the results of the rigid paddle model.

4.1.1. Experiments

The first objective of the paddle experiments was to validate the rigid paddle model. The second objective was to determine the oscillation parameters which produce the greatest net thrust per unit power. In Chapter 2, the lift and drag forces were transformed into a thrust force, which was parallel to the offset angle direction, and a side force that was perpendicular to that direction. When the offset angle direction is aligned with the back of the robot, the thrust force constitutes the force that propels the vehicle and should be as great as possible. The side force constitutes the force that moves the robot upwards or downwards and should be as close to zero as possible. The test matrix was designed to include all periods and amplitudes of oscillation that produce significant thrust forces.

Finding the oscillation parameters which produce the greatest net thrust per unit power is useful in applications, such as AQUA, where the power is limited.

In rigid paddle simulations, oscillations with large periods generated smaller forces than did oscillations with shorter periods. Oscillations with a period of 2 seconds resulted in forces which were only slightly greater than the noise level on force measurements, while oscillations with a period of 1 second produced significant forces. Thus, 1 second was chosen as the upper bound for the period and 0.4 seconds was chosen as the lower bound. Intermediate oscillation periods of 0.6 seconds and 0.8 seconds were included in the test matrix.

The test matrix for amplitudes of oscillation (defined here as peak-to-peak magnitudes) was also chosen based on preliminary tests and simulations. Preliminary tests showed that amplitudes of oscillation of 10° resulted in forces which were approximately equal to the sensor noise level. Simulations of the rigid paddle indicated that net thrust and required power monotonically increase with amplitude of oscillation increasing up to an amplitude of π. Taking the ratio of net thrust to power shows that smaller amplitudes produce more thrust per watt than larger amplitudes do. Based on this, it was conjectured that the most efficient amplitude of oscillation would be less than 90°. Thus, amplitudes of oscillation of 20° to 90°, in increments of 10°, were chosen for the paddle experiments. The 4 periods coupled to 8 amplitudes led to a total of 32 experiments.

For all thirty-two cases in the test matrix, the paddle followed a symmetric cubic spline trajectory having an offset angle of 0°. This type of trajectory was described in Chapter 2 and it was shown in Figure 2-4 for an oscillation having a period of 1 second and an amplitude of 90°.

4.1.2. Trajectory Tracking Difficulties

In each experiment, the paddle did not track the desired trajectory accurately: the amplitude of oscillation was smaller than that desired and the motion tended to lag the command. The paddle's tracking can be seen in Figure 4-2 for a desired amplitude of 60° and a period of 1 second.

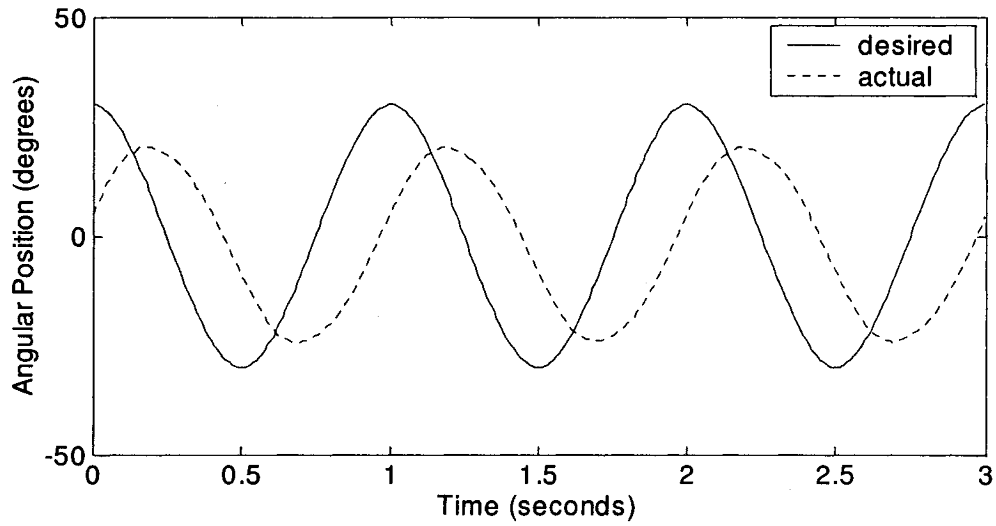

Figure 4-2: Rigid paddle trajectory tracking; the desired amplitude of oscillation is 60° and the actual amplitude is 44°.

Figure 4-2 shows that for a desired amplitude of 60° and a period of 1 second, the paddle sweeps an angle of 44°. The first plot of Figure 4-3 shows that for a desired amplitude of 90° and a period of 1 second, the paddle sweeps an angle of 70°. In all experiments, the actual paddle position lags the desired paddle position by 0.1 to 0.2 seconds. This time lag causes the actual sweep angle to be smaller than the desired sweep angle. At the instant when the desired trajectory reaches a local maximum (shown as 2 in Figure 4-3), the actual paddle position is 5°. Between 2 and 3, the desired position is decreasing but is still greater than the actual position and the actual position keeps increasing. Where the actual and desired curves intersect (3), the component of torque due to position error starts being negative. The component of torque due to speed error has been negative since 1. Thus, the torque must be negative at point 3 and the paddle is driven in the opposite direction than the one it is traveling in. When the paddle's decreasing speed reaches 0, the paddle reverses direction (4).

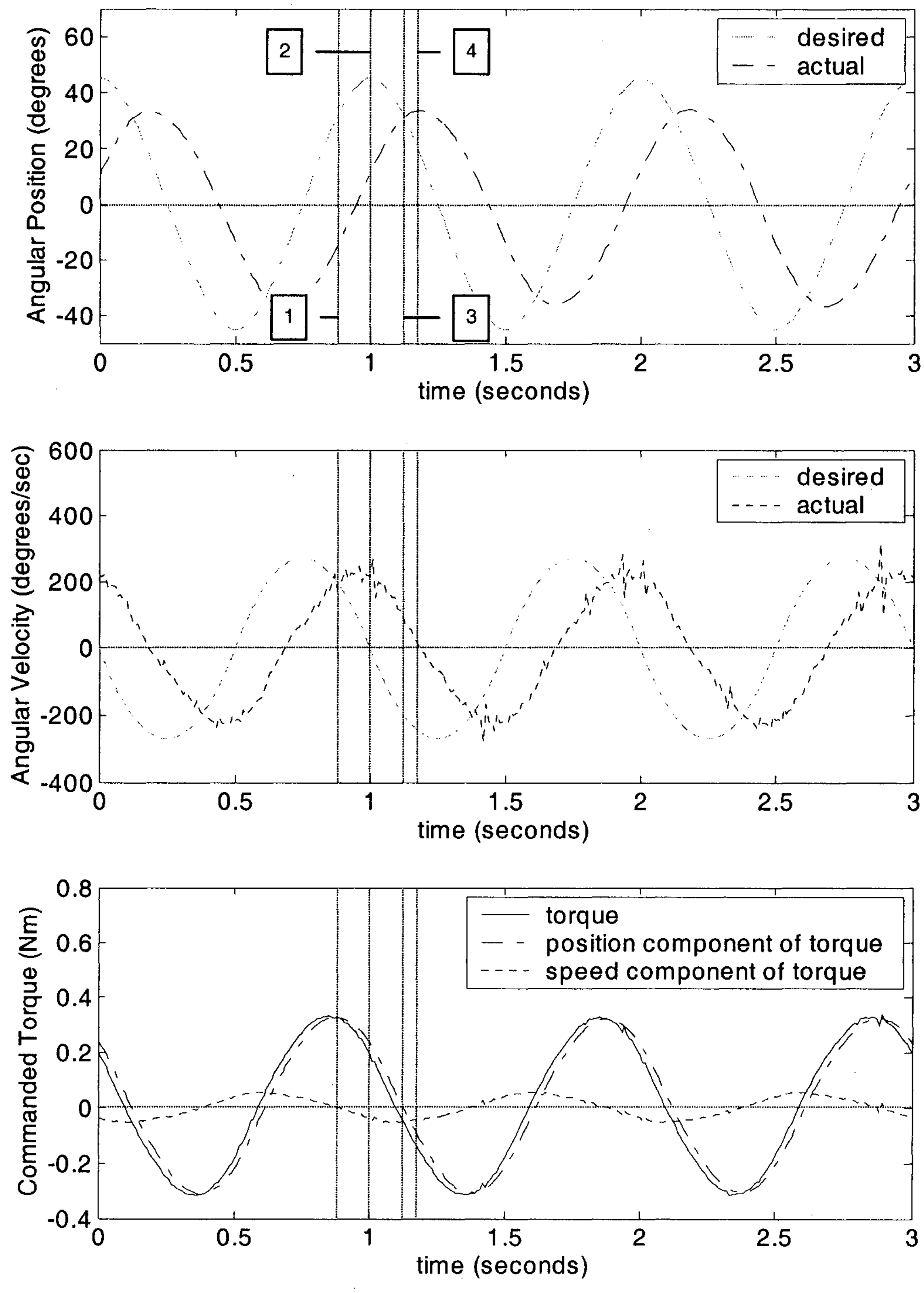

Figure 4-3: Angular position, angular velocity and commanded torque shown to explain why the actual sweep angle is smaller than the desired sweep angle.

The ratio of actual oscillation amplitude to desired oscillation amplitude, hereafter called amplitude ratio, is always less than 1 in water for the rigid paddle. Figure 4-4 illustrates how the amplitude ratio varies with period and desired amplitude of oscillation. The amplitude ratio decreases with increasing frequency (decreasing period) for all desired amplitudes.

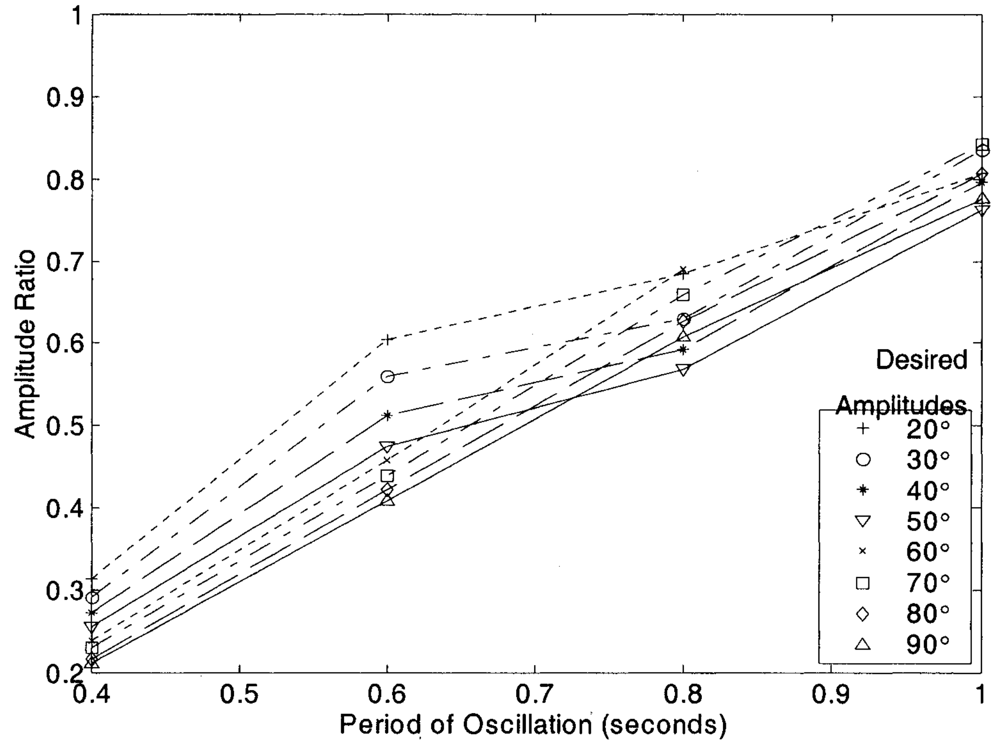

Figure 4-4: Amplitude ratio vs. period for different desired amplitudes of oscillation; amplitude ratio decreases with decreasing period for all desired amplitudes.

One possible reason why the paddle does not follow the desired trajectory accurately is that the applied torque is not great enough. According to specifications, at a continuous speed of 33rpm, the motor and gearhead assembly can output a maximum torque of 0.8Nm. In the experiment of Figure 4-3, the paddle's maximum speed of oscillation is 33rpm and the commanded torques are smaller than 0.35Nm. Increasing the requested torques, by increasing the gains of the PD controller, should have resulted in better trajectory tracking, but led to unstable paddle motion. Each experiment was conducted with the maximum stable gains. The proportional gain of the 32 experiments ranged between 0.25 and 0.40. It was lowest for the oscillation with the largest period and smallest amplitude and it increased as the oscillation period decreased and/or the amplitude increased. The derivative gain of all experiments was 0.01; setting it to any value greater than 0.01 led to instability. The discrepancy between actual and commanded paddle travel was not considered to be problematic in the present context, since the experiment and simulation could be compared based on the actual paddle motion rather than the commanded motion.

4.1.3. Noise in the Collected Data

During the experiments, peak-to-peak force measurements along the x- and z- axes ranged between 0.6N and 6N. These measurements are much lower than the maximum force that the load cell can measure along those axes (130N). Noise associated with force measurements along the x- and y-axes was 0.1N. This noise level represents less than 0.1% of the full range, but is a significant percentage of some of the recorded forces. The signal-to-noise ratio was as low as 6:1 for some experiments.

In addition to the small amplitude noise originating from the transducer, a larger amplitude signal at approximately 16Hz or 47Hz was superimposed on the force measurement signals, as can be seen in Figure 4-5.

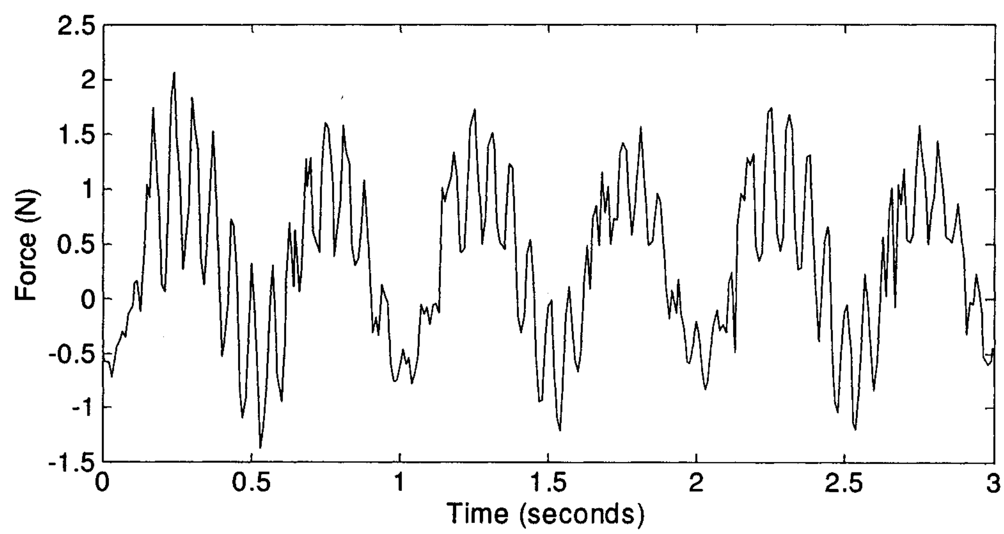

Figure 4-5: Force measurement along z-axis for an oscillation having A = 70°, T = 1s and γ_0 = 0°.

Using a Fast Fourier Transform (FFT), a power spectrum was obtained for each force and moment measured during two experiments having oscillation periods of 0.6 seconds and 1 second. The frequencies corresponding to the highest intensity peaks on the power spectra, hereafter called dominant frequencies, are shown in Table 4.1. In the table, F_i corresponds to the force measured along axis i of the sensor, while T_i corresponds to the moment about axis i, for $i = x$, y and z. Table 4.1 also shows the dominant frequencies of the thrust measuring setup impact test described in Chapter 3. As highlighted with bold characters in the table, the dominant frequencies in the impact test are also dominant frequencies in the two experiments. Based on this, a conclusion can safely be drawn that the higher frequencies observed in the experimental measurements can be attributed to natural vibration of the test setup.

Dominant frequencies of tests / Measurements	Impact test	Experiment #1 Period = 0.6 seconds (Frequency = 1.66Hz)	Experiment #2 Period = 1 second (Frequency = 1Hz)
	Dominant frequencies (Hz)	Dominant frequencies (Hz)	Dominant frequencies (Hz)
F_x	**16**	1.69 and **15**	1 and **16**
F_y	**47**	1.69 and **47**	1 and **47**
F_z	**16**	3.38 and **15**	2 and **16**
T_x	**16, 47**	3.38, **15** and **47**	2, **16** and **47**
T_y	none	1.69	1
T_z	**16**	1.69 and **15**	1 and **16**

Table 4.1: Dominant frequencies in forces and moments measured during impact test and two experiments.

The lower dominant frequencies that cannot be attributed to the setup vibrations, are in integer proportion to the frequency of oscillation. The lower dominant frequencies in F_x, F_y, T_y and T_z are equal to the frequency of oscillation of the experiment, while those in F_z and T_x are double the frequency of oscillation. Rigid paddle model simulations, such as the one shown in Figure 2-13, also show that the frequency of the perpendicular force F_x

is the same as the frequency of oscillation and that the frequency of the parallel force F_z is double the frequency of oscillation.

4.1.4. Data Processing

As explained in Chapter 3, an attempt was made to damp the vibrations of the test structure by using rubber padding. A recommendation was also made to stiffen the structure. For the present work, the unwanted noise at 16 and 47Hz was removed by applying a low-pass filter to the measurements. The experiments were performed at frequencies of oscillation ranging between 1 and 2.5Hz. As stated in Section 4.1.3 the dominant frequencies in forces and torques are equal to the frequency of oscillation or double that frequency. The dominant frequencies of all experiments therefore range between 1 and 5Hz; the latter being double the highest oscillation frequency. The lowest frequency of the noise to be removed is 16Hz. Therefore, the cutoff frequency of the filter must be greater than 5Hz and lower than 16Hz. A cutoff frequency of 7Hz was found to be the best compromise between attenuating the higher frequencies without attenuating the lower ones.

A double-pass third-order Butterworth filter with a cutoff frequency of 7Hz was applied to force and torque measurements of all experiments. This filter processes the data in the forward direction, reverses the filtered sequence and runs it back through the filter. Consequently, the resulting sequence has zero-phase distortion. Figure 4-6 shows the magnitude response of the filter. Frequencies up to 5Hz are attenuated by less than 12%, while frequencies of 16 Hz are attenuated to 0.4% of their original value. A 2Hz force signal is illustrated in Figure 4-7 before and after it has been filtered.

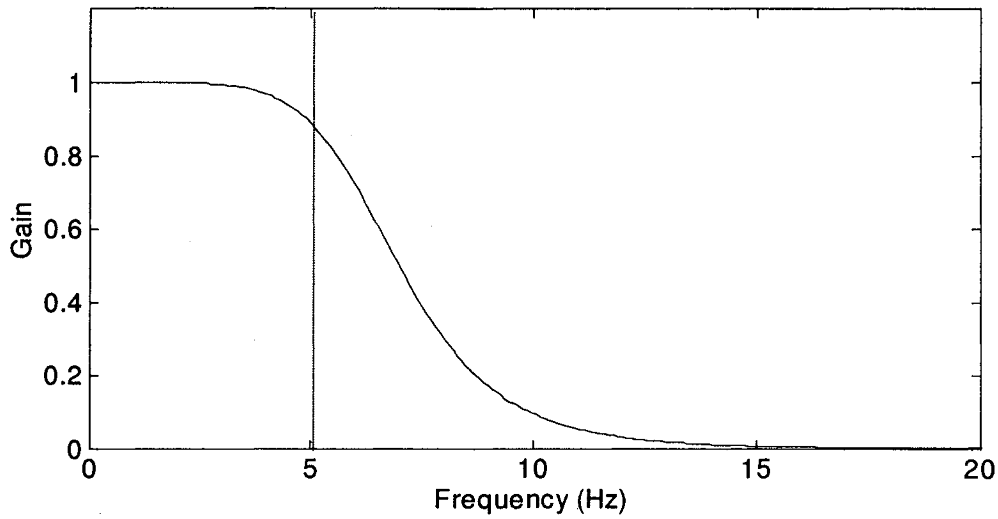

Figure 4-6: Magnitude response of double-pass third-order Butterworth filter with a cutoff frequency of 7Hz.

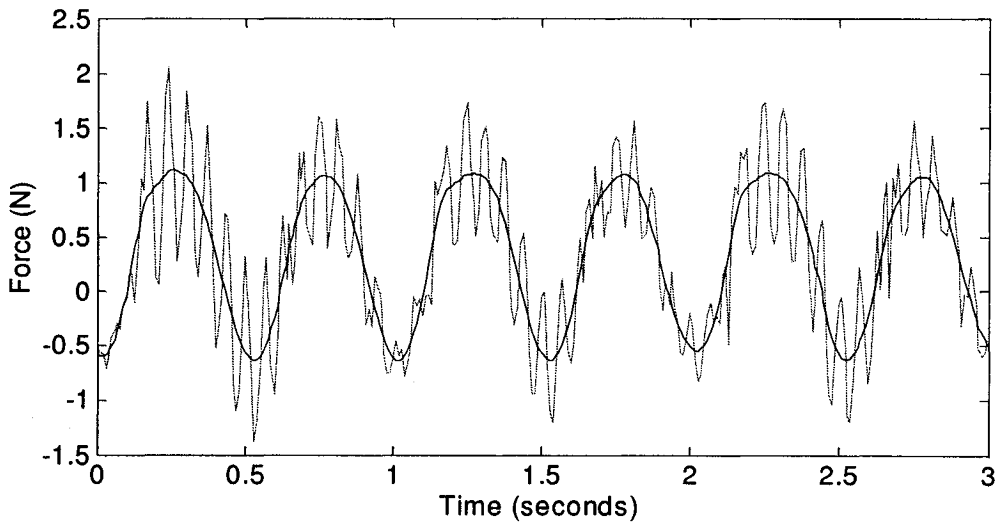

Figure 4-7: Filtered force measurement along z-axis for an oscillation having A = 70°, T =1s and γ_0 = 0°.

4.1.5. Rigid Paddle Results

The rigid paddle was oscillated at four different periods for each of the eight different amplitudes. Each of the 32 period/amplitude combinations was repeated twice. Forces and torques generated during each experiment were recorded and filtered. Of particular interest are two forces: the force parallel to the offset angle (F_z) and the force perpendicular to it (F_x). As stated earlier, the parallel force constitutes the force that propels the vehicle forwards, while the perpendicular force constitutes the force that moves the robot upwards or downwards. The parallel and perpendicular forces were integrated over a fixed integer number of oscillations and divided by the time it took to perform the oscillations to obtain the time-averaged parallel and perpendicular forces, which are shown in Figure 4-8. The cycle-averaged forces shown in Figure 4-9 were obtained by instead dividing by the number of oscillations. As previously discussed, the actual amplitude of oscillation was smaller than the desired one. In Figure 4-8 and Figure 4-9, the average forces are plotted against the actual amplitude of oscillation.

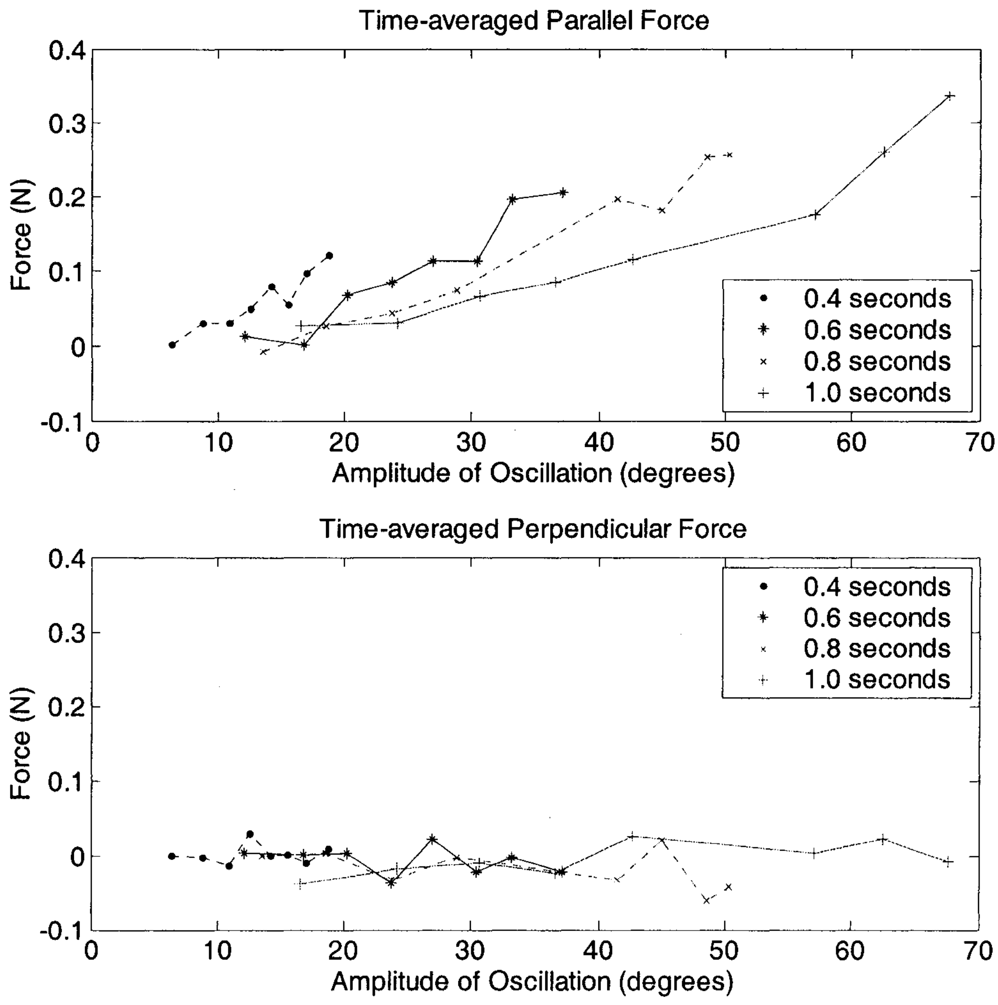

Figure 4-8: Time-averaged parallel and perpendicular forces resulting from oscillations of different periods and amplitudes.

As can be seen from the lower plot of Figure 4-8, the perpendicular force does not depend on amplitude of oscillation or period, and is approximately zero for all experiments. As is evident from the upper plot of Figure 4-8, the parallel force increases with oscillation amplitude and decreases with oscillation period. More oscillations are performed in a given time when the period is shorter. Therefore, if two oscillations of the same amplitude, but different periods produce the same net force over one cycle, then the oscillation with the shorter period will produce more force per unit time. Whether oscillations of different periods produce equal net forces over one cycle can be determined from Figure 4.9.

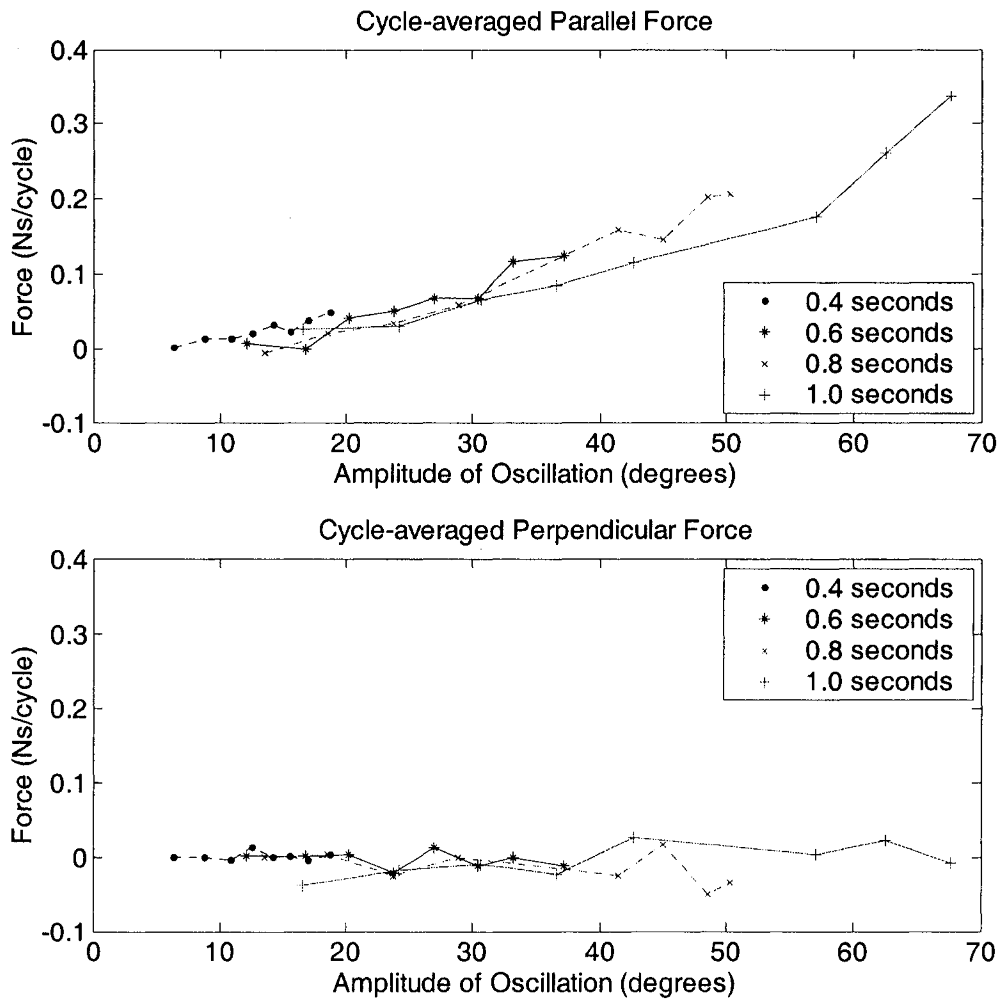

Figure 4-9: Cycle-averaged parallel and perpendicular forces resulting from oscillations of different periods and amplitudes.

The upper plot of Figure 4-9 shows, that the cycle-averaged parallel force, like the time-averaged parallel force, increases with oscillation amplitude. The cycle-averaged parallel force, however, increases only slightly with decreasing period. Intuitively, one might expect that the thrust per cycle should remain constant with changing period, but the results appear to show that a faster oscillation produces a slightly greater net force per cycle.

It was just stated that oscillations of a given amplitude and smaller periods generate a greater time-averaged parallel force than do oscillations of larger periods. However, oscillations with smaller periods require greater average power than do oscillations with larger periods to generate the same amplitude of oscillation, as shown in Figure 4-10. Power was calculated as the product of torque and paddle angular velocity. Average power was the integral of power divided by the time of integration. Because oscillations producing a greater parallel force require greater power to do so, it is important to examine the ratio of parallel force to power required as a measure of paddling efficiency. This ratio is shown in Figure 4-11 and represents the average force produced per Watt of power.

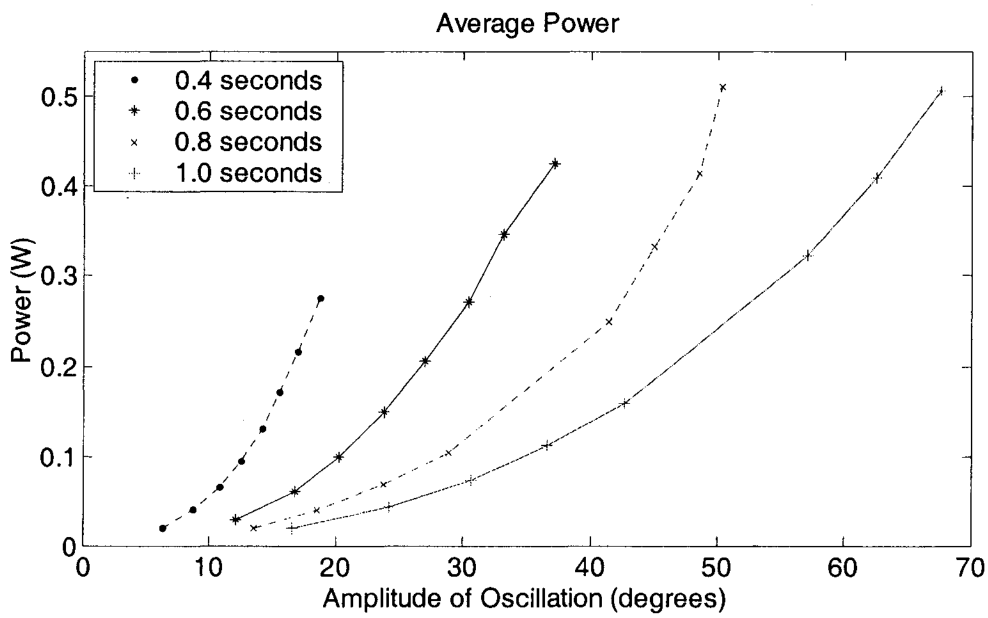

Figure 4-10: Average power required by oscillations of different periods and amplitudes.

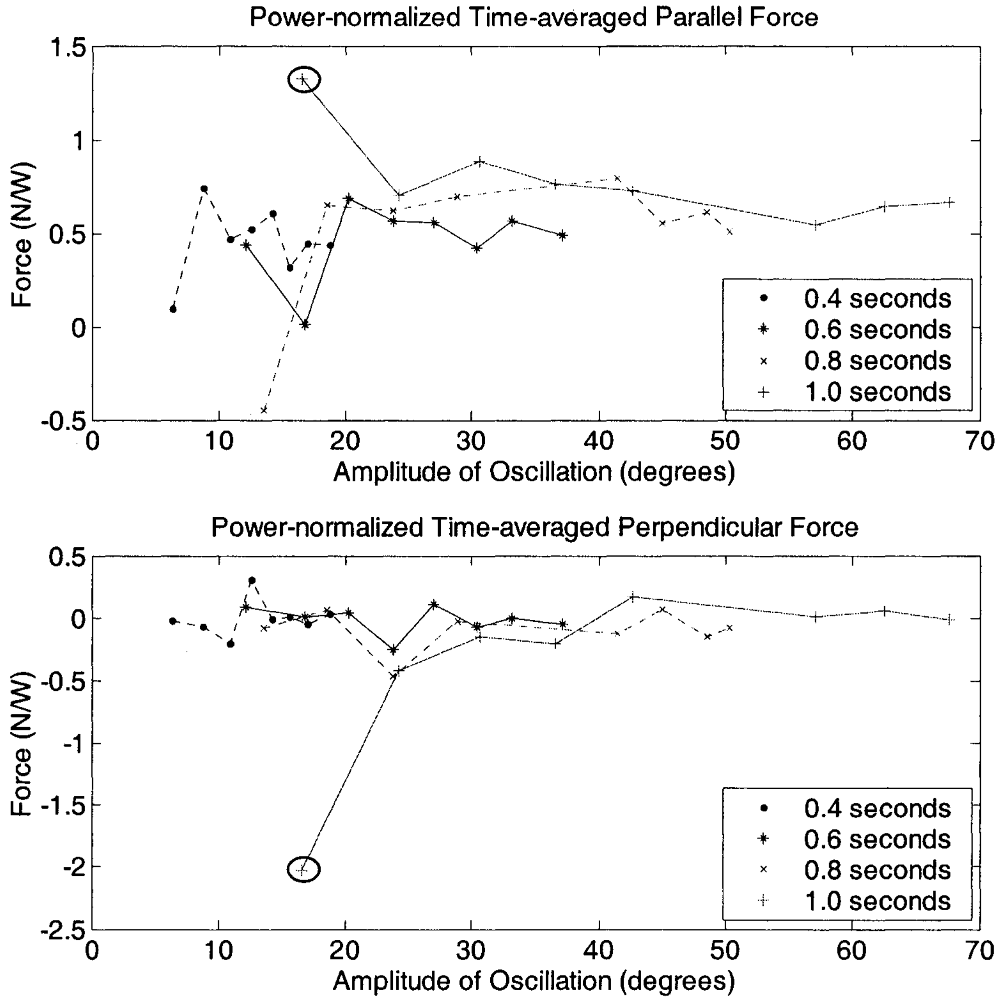

Figure 4-11: Power-normalized time-averaged parallel and perpendicular forces resulting from oscillations of different periods and amplitudes.

The points circled in Figure 4-11 represent an artifact resulting from a division by a value of power very close to zero and these points were dismissed from the analysis. The results appear to show that longer periods produce greater power-normalized thrust. An oscillation period T of 1 second and an amplitude A of 30° appear to produce the highest power-normalized time-averaged parallel force.

4.1.6. Comparison of Experimental Results and Simulations

To gauge the accuracy of the model described in Chapter 2, the time-averaged experimental forces shown in Figure 4-8 were compared to their corresponding time-averaged simulated forces.

For each of the 32 experiments, the instantaneous forces produced by a paddle oscillating with the period and amplitude of the experiment were calculated using the rigid paddle model incorporating the inflow estimate presented in Chapter 2. Then, the instantaneous forces were integrated over time, just as was done for Figure 2-13, in order to calculate the impulses. Finally, each impulse was divided by the time over which the instantaneous force had been integrated in order to find the time-averaged simulated force.
Taking the experiment of Figure 2-13 as an example, the parallel impulse is equal to 2.23Ns at 3 seconds. Dividing 2.23Ns by 3s gives a time-averaged parallel force of 0.74N. Figure 2-13 is the simulation for an actual amplitude of oscillation of 90° and a period of 1 second. Since none of the experiments having a period of 1second had an actual amplitude of 90°, the parallel time-averaged force of Figure 2-13 does not appear in Figure 4-13. If that point were to appear in Figure 4-13, it would have an x-coordinate of 90° and a y-coordinate of 0.74N.

From Figure 4-12 and Figure 4-13, which show the time-averaged experimental forces and the time-averaged simulated forces, it can be seen that there is a good match between the two. The time-averaged simulated forces are related to the inflow used in their calculation. The fact that the simulated forces match the experimental ones indicates that the experimental inflow was estimated correctly in the simulation. As stated in chapter 3, measuring entrained flow would have eliminated the need to estimate it and it is recommended to add a flow velocity sensor on the thrust measuring setup for future experiments.

The simulated parallel time-averages forces increase with oscillation amplitude and decrease with oscillation period as do the experimental parallel time-averages forces.

The simulated perpendicular time-averaged forces are zero, while those obtained experimentally are nearly zero, as shown in the lower plots of Figure 4-12 and Figure 4-13. This implies that, when the paddle is used as a thruster, it will generate forward thrust without producing a net vertical force, which would result in a vertical motion of the robot. Of course, since the instantaneous perpendicular force oscillates, it is expected that the robot will oscillate vertically unless the six paddles can be coordinated to keep the net vertical force at zero.

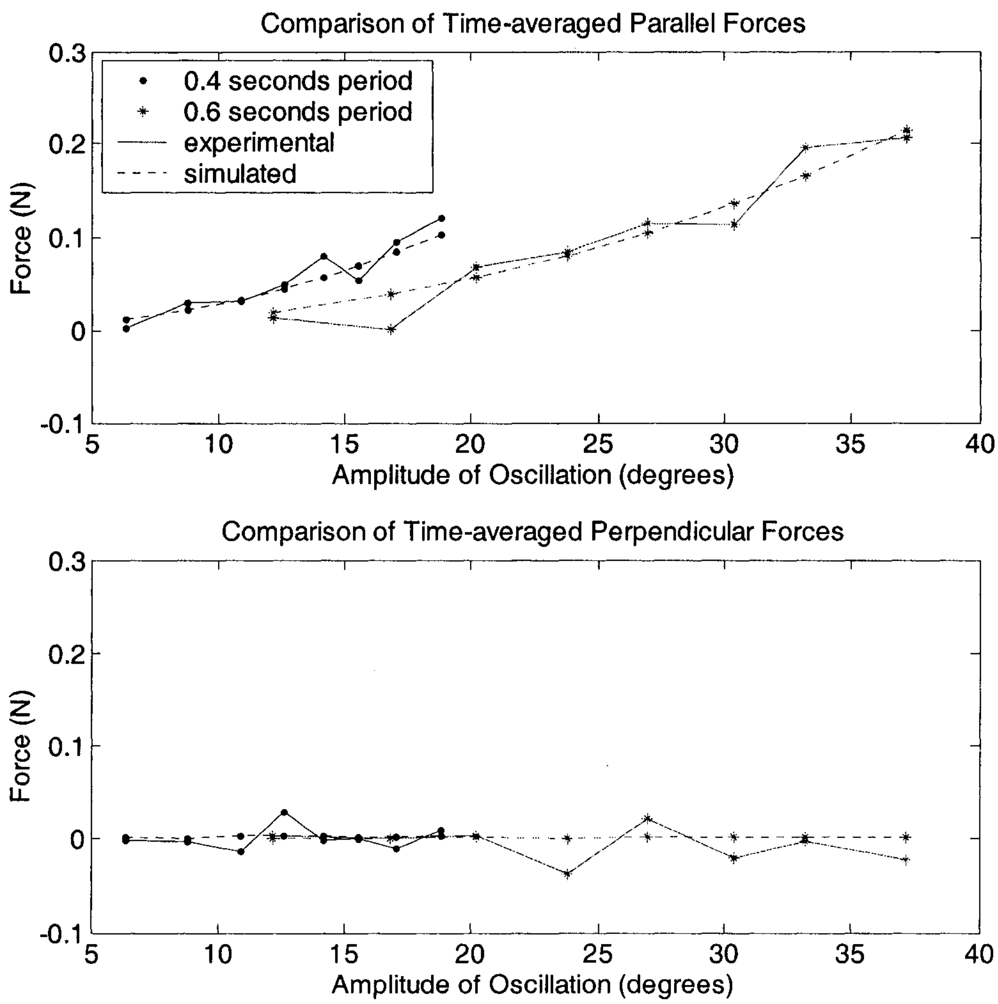

Figure 4-12: Comparison between experimental and simulated results for oscillations with periods of 0.4s and 0.6s.

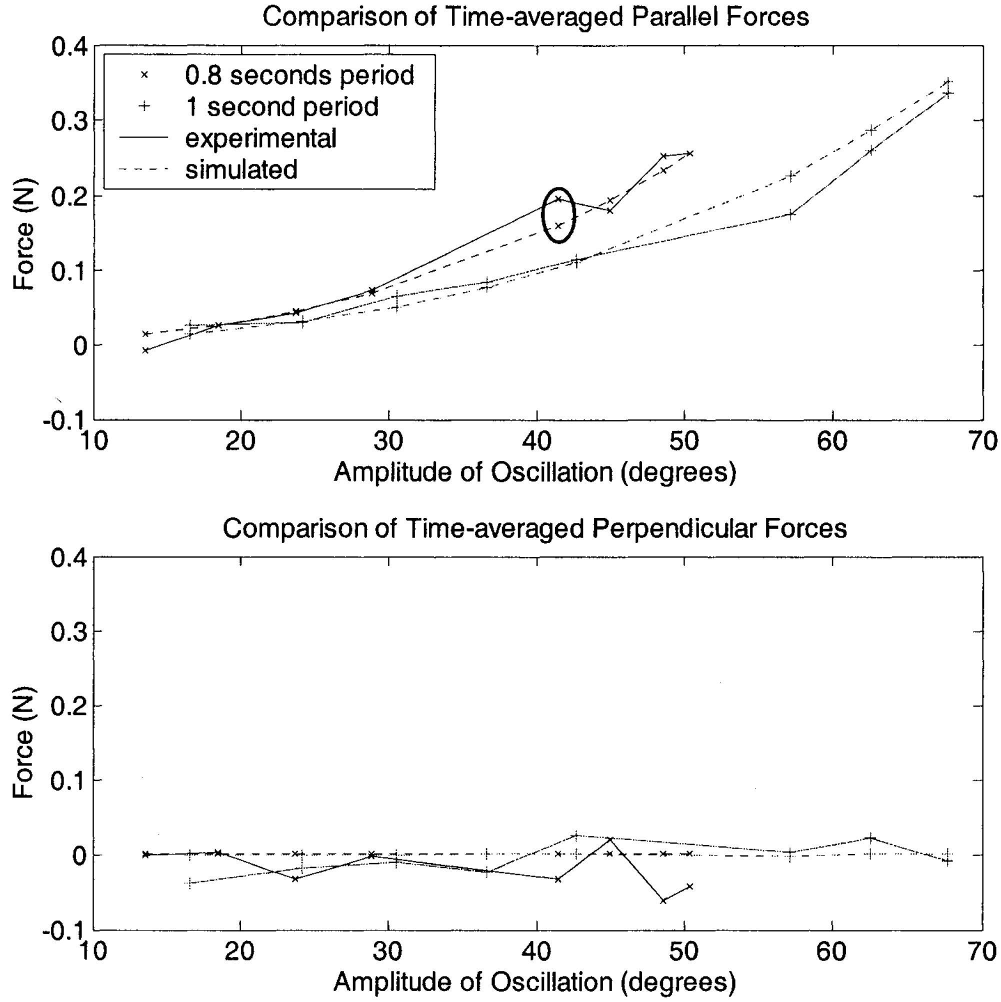

Figure 4-13: Comparison between experimental and simulated results for oscillations with periods of 0.8s and 1s.

As stated previously, the simulated perpendicular time-averaged forces are zero, while those obtained experimentally are nearly zero. Figure 4-14 shows that simulated and experimental perpendicular forces vary slightly from cycle to cycle. It also shows that the experimental force does not have a perfect sinusoidal shape that the simulated force has. It is not the slight variation of the experimental force from cycle to cycle, but rather the imperfection of the sinusoidal shape of the experimental force that explains why the experimental time-averaged force is not equal zero.

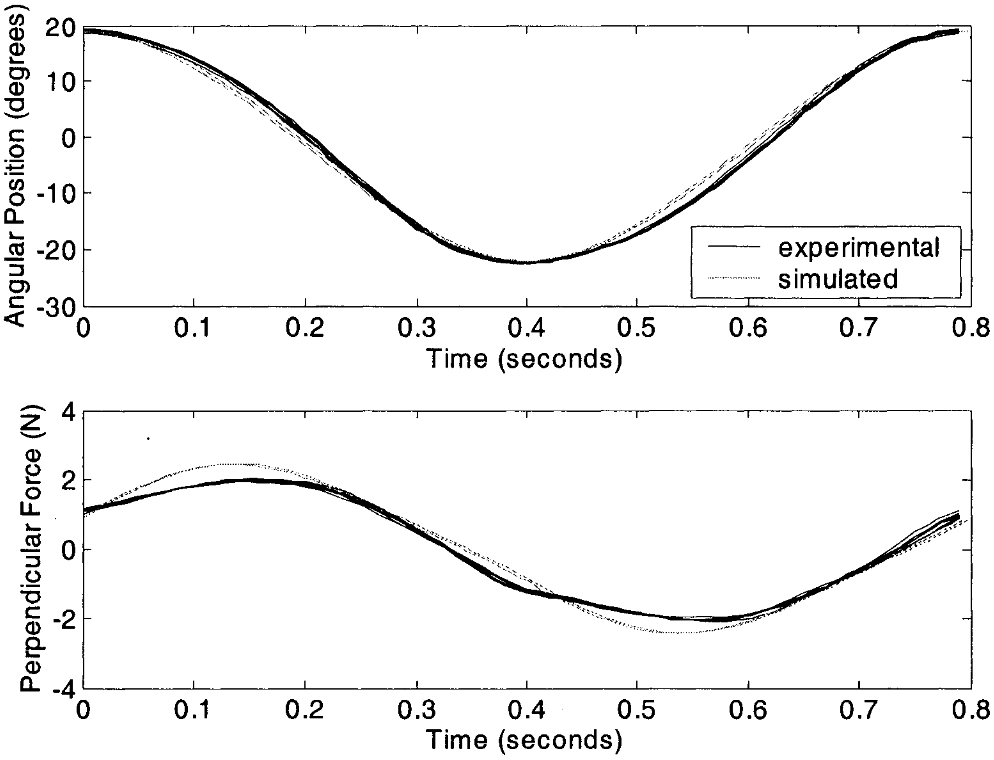

Figure 4-14: Superposition of angular position and perpendicular force of 8 cycles.

The points circled in Figure 4-13, for a period of 0.8 seconds and an amplitude of 42°, constitute one of the worst matches between an experiment and its corresponding simulation. The parallel and perpendicular forces, which were integrated to yield those points, are shown in Figure 4-15 to highlight that, even when the match appears poor, the simulated and experimental forces are, in fact, in reasonable agreement. Because the forces are integrated, small differences between the simulated and experimental forces are sometimes compounded.

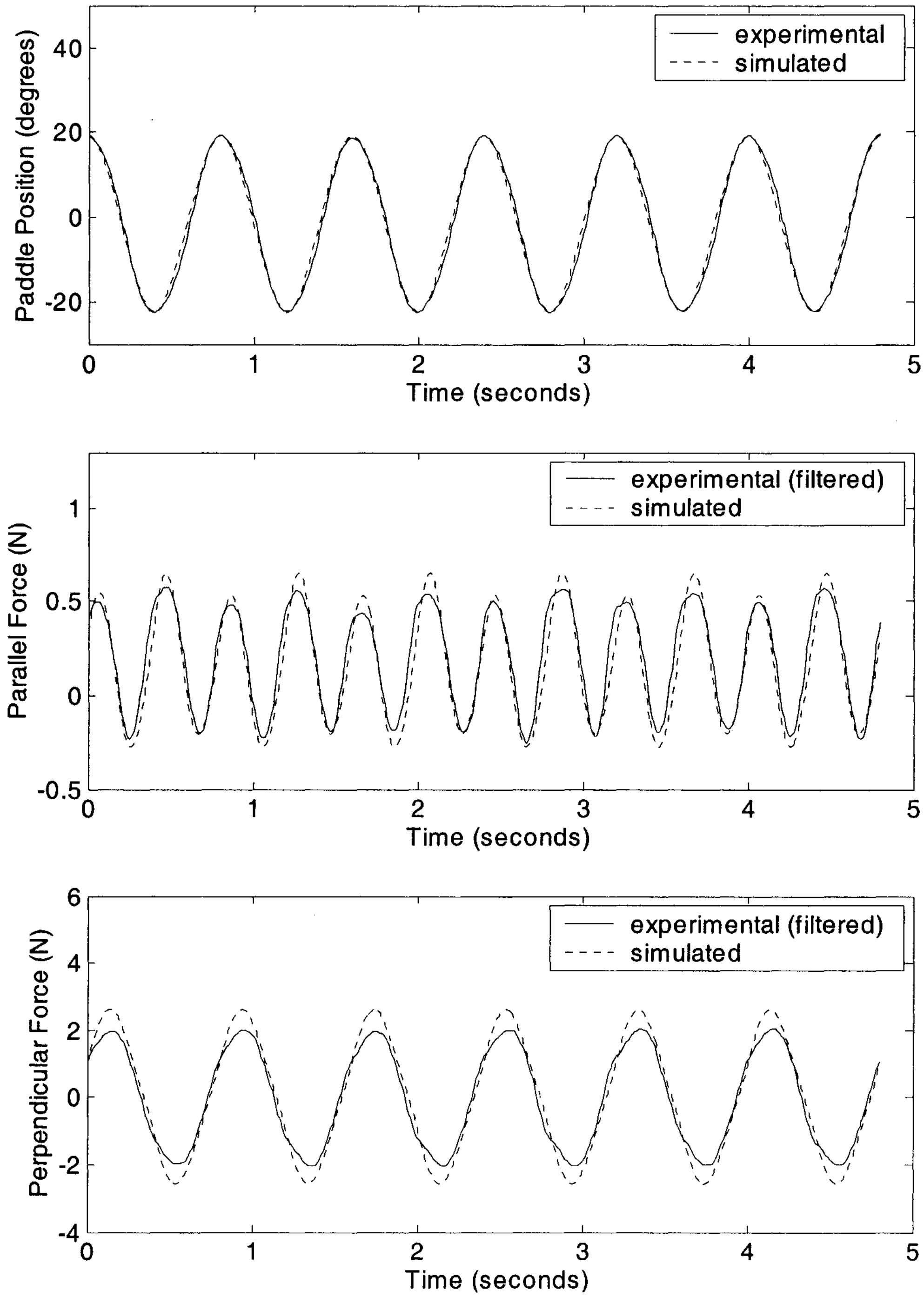

Figure 4-15: Simulated and experimental forces match fairly accurately, but when these forces are integrated, differences between them are sometimes compounded and the integrated results appear not to match very accurately.

4.1.7. Parameters Extracted from Experiments

One of the parameters that was extracted from the experimental results is the paddle's moment of inertia, which includes the added mass moment of inertia. As will be explained in Section 5.2, when a body is accelerated in water, the fluid surrounding it is also accelerated. The effect of fluid being accelerated by the body is represented by added mass.

The torque acting on the paddle was assumed to be a linear combination of the acceleration of the paddle and the square of the paddle speed:

$$\tau = K_1\dot{\gamma}^2 + K_2\ddot{\gamma} \tag{4.1}$$

The acceleration term is related to paddle inertia, which includes added mass effects, while the velocity term is associated with fluid viscosity. The measured torque and paddle velocity were both filtered. The acceleration of the paddle was computed from the velocity and filtered. Equation (4.1) was written for every sample point of an experiment to form an overdetermined system of the form

$$\begin{bmatrix} \dot{\gamma}_1^{\,2} & \ddot{\gamma}_1 \\ \dot{\gamma}_2^{\,2} & \ddot{\gamma}_2 \\ \vdots & \vdots \\ \dot{\gamma}_n^{\,2} & \ddot{\gamma}_n \end{bmatrix} \begin{bmatrix} K_1 \\ K_2 \end{bmatrix} = \begin{bmatrix} \tau_1 \\ \tau_2 \\ \vdots \\ \tau_n \end{bmatrix}$$

Using a minimum norm solution, the unknown coefficients, K_1 and K_2, were computed. Across all experiments, a value of 0.0078kg·m^2 was obtained for K_2.

Another parameter that was extracted from the experiments is the characteristic length of the paddle. This length was determined by decomposing forces along the x- and y-axes into forces components parallel and perpendicular to the paddle. Torque is a linear combination of the forces parallel ($F_{//}$) and perpendicular ($F_{\perp}$) to the paddle. For each sample point of an experiment, can be written

$$\tau = K_3F_{//} + K_4F_{\perp} \tag{4.2}$$

Solving the overdetermined system allows K_3 and K_4 to be computed. Since the force parallel to the paddle cannot produce a moment, K_3 should be 0. The constant K_4 represents the characteristic length and must therefore be smaller than the paddle length

(20cm). Most experiments resulted in values of K_3 and K_4 that were physically meaningful. Experiments having values of K_3 smaller than 1cm were retained. Values for K_4 in these experiments ranged between 12.2cm and 15.0cm. The variation of K_4 with amplitude of oscillation is illustrated in Figure 4-16. The apparent linear trend could be explained by a rearward shift in the center of pressure as the amplitude increases.

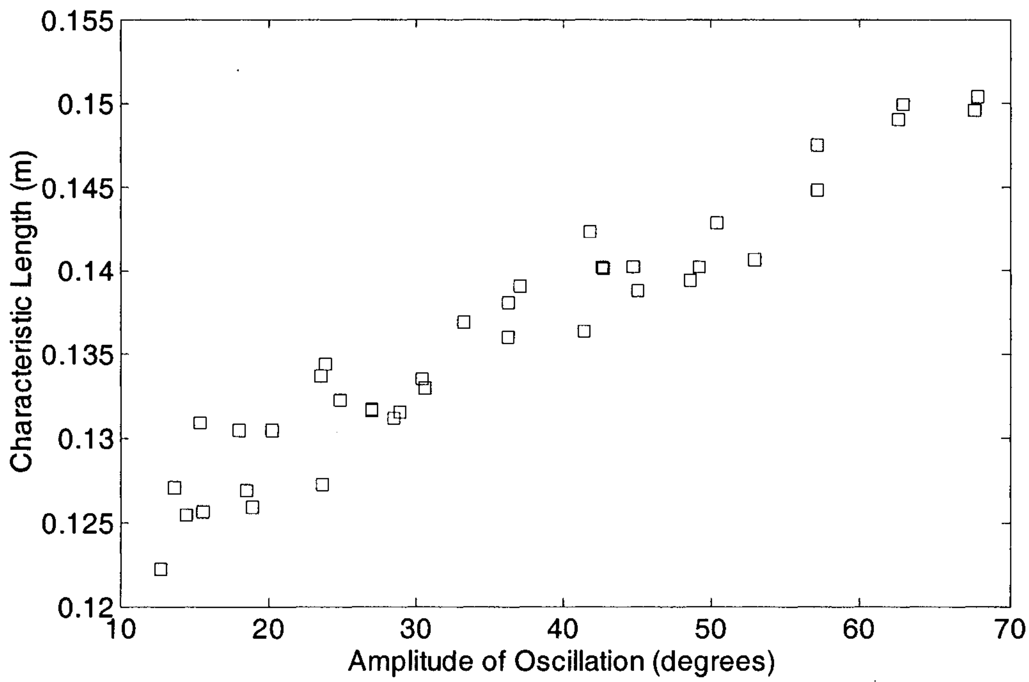

Figure 4-16: A linear relationship between the amplitude of oscillation and the characteristic length emerges from this plot.

4.2. Flexible Fin

Flexible fins can have a higher propulsive efficiency than rigid paddles do [32]. A set of flexible fins was developed at the Ambulatory Robotics Laboratory and tested on the thrust measuring setup. The flexible fins were ranked in terms of the net thrust they produced. The flipper producing the highest net thrust was used on the robot and is illustrated in Figure 4-17. This fin's structure is inspired by the morphology of a duck's webbed foot. Dimensions of the fin (a length of 20cm and a width tapering from 4cm to 7cm) are close to those of the rigid paddle. On that basis, the rigid paddle can be compared to the flexible fin. This section outlines the difference in the thrust produced by a rigid plate and a flexible fin.

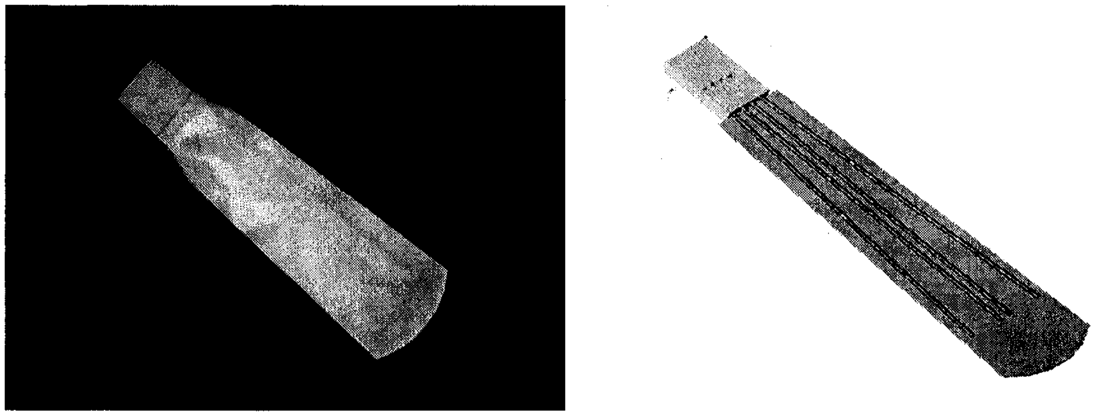

Figure 4-17: Picture and CAD drawing of flexible fin.

A subset of the experiments performed on the rigid paddle was also performed on the flexible fin. The flexible fin demonstrated the same trajectory tracking difficulties that were exhibited by the rigid paddle (described in Section 4.1.2). The rigid paddle and the flexible fin tracked a trajectory having a period of 0.6 seconds and a desired amplitude of 60°, as shown in Figure 4-18. The actual amplitude of the flexible fin trajectory is closer to the desired amplitude than that of the rigid paddle, and the time lag between the desired and the actual positions is smaller for the flexible fin.

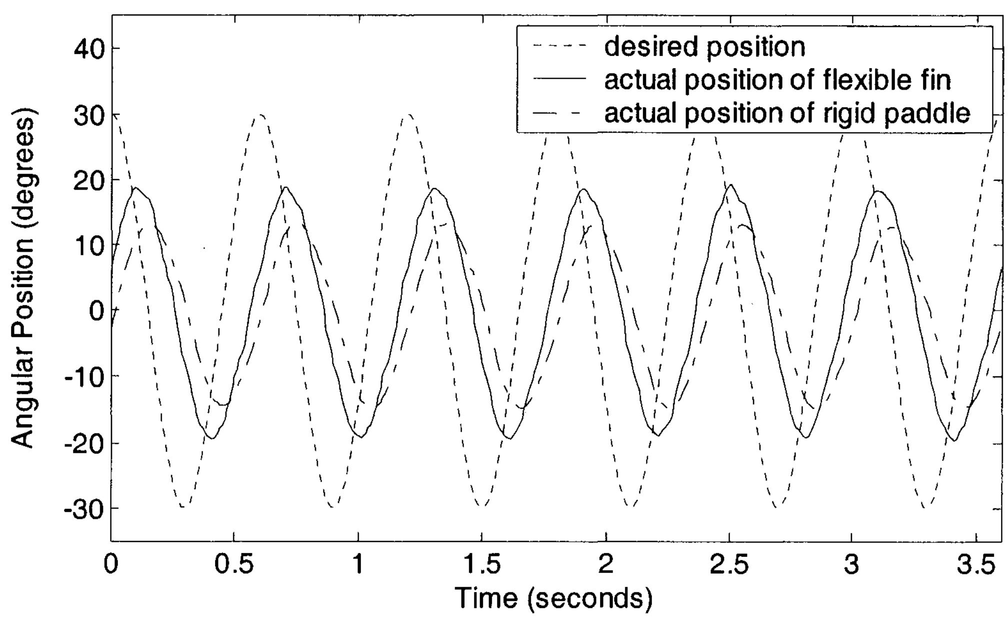

Figure 4-18: The flexible fin and the rigid paddle's tracking of a trajectory with a period of 0.6s and a desired amplitude of 60°.

In all experiments, the flexible fin had a greater amplitude ratio than did the rigid paddle. The amplitude ratio of the flexible fin increased with increasing periods, as did the ratio of the rigid paddle. For experiments with a period of 1 second, the flexible fin's amplitude ratio exceeded 1, meaning that the actual amplitude was greater than the desired one.

The better trajectory tracking of the flexible fin was due to the higher stable gains that could be used for the fin than for the rigid paddle. For the trajectories shown in Figure 4-18, the flexible fin had a proportional gain of 1.5, while the rigid paddle had a gain of 0.4. Both paddles had a derivative gain of 0.01. A greater proportional gain resulted in a larger applied torque. In order to follow the trajectories illustrated in Figure 4-18, the flexible fin and the rigid paddle were supplied with peak-to- peak torques of 1.53Nm and 0.74Nm respectively.

For all experiments, the flexible fin produced more net thrust than did the rigid paddle. For example, flexible fin oscillations with a period of 0.6 seconds and an actual amplitude of 37° produced time-averaged parallel and perpendicular forces of 0.70N and –0.08N respectively. Rigid paddle oscillations with the same parameters generated forces of 0.21N and –0.04N respectively. The thrust force produced by the flexible fin was 3.3 times greater than the thrust force produced by the rigid paddle. The side force produced by the flexible fin was 2 times greater than the side force produced by the paddle, but both forces were negligible in magnitude.

Although the flexible fin is capable of producing greater forces, it requires more power to do so. Dividing the time-averaged forces by the average power required to perform the oscillations resulted in power-normalized time-averaged parallel and perpendicular forces of 0.60N/W and -0.07N/W for the flexible fin and 0.49N/W and -0.05N/W for the rigid paddle. It is interesting to note that the fin produces only 1.2 times more thrust than does the rigid paddle for a given amount of power. Thus, the flexible fin has the main advantage of generating greater thrust than does the rigid paddle, but it does so only slightly more efficiently than the rigid paddle.

4.3. Paddle Trajectory Development

Videos of sea turtles provided inspiration to develop a gait mimicking their swimming stroke, in which the paddles sweep water faster in one direction than in the other (stroke is done faster than recovery). In simulations, a rigid paddle sweeping 180° rapidly in one direction and returning slowly to the starting position generated large net thrust while still producing near zero side force. Experiments verified this. Forces generated by the flexible fin as it performed oscillations having a desired amplitude of 180°, a period of 1 second and an oscillation ratio of 0.2 are shown in Figure 4-19. The oscillation ratio was defined by Equation (2.6) as the ratio of the time it takes to perform the stroke to the time it takes to perform the entire oscillation (stroke and recovery). The impulses generated by the flexible fin are also shown in Figure 4-19.

Time-averaged parallel and perpendicular forces generated with the asymmetrical oscillation of Figure 4-19 are 2.39N and -0.14N. The time-averaged forces generated by the flexible fin performing the same trajectory (A = 130°, T = 1 second and $\gamma_0 = 0°$) with different oscillation ratios are displayed in Table 4.2. A proportional gain of 1.5 and a derivative gain of 0.01 were used for all oscillations. Trajectories with smaller oscillation ratios generate greater parallel time-averaged forces.

Oscillation ratio R	Parallel time-averaged force (N)	Perpendicular time-averaged force (N)
0.2	2.39	-0.14
0.3	1.86	-0.36
0.4	1.80	-0.12
0.5	1.77	0.05

Table 4.2: Time-averaged parallel and perpendicular forces generated by paddles undergoing trajectories with amplitude A = 130°, period T = 1s, offset angle $\gamma_0 = 0°$ and oscillation ratios R of 0.2, 0.3, 0.4 and 0.5.

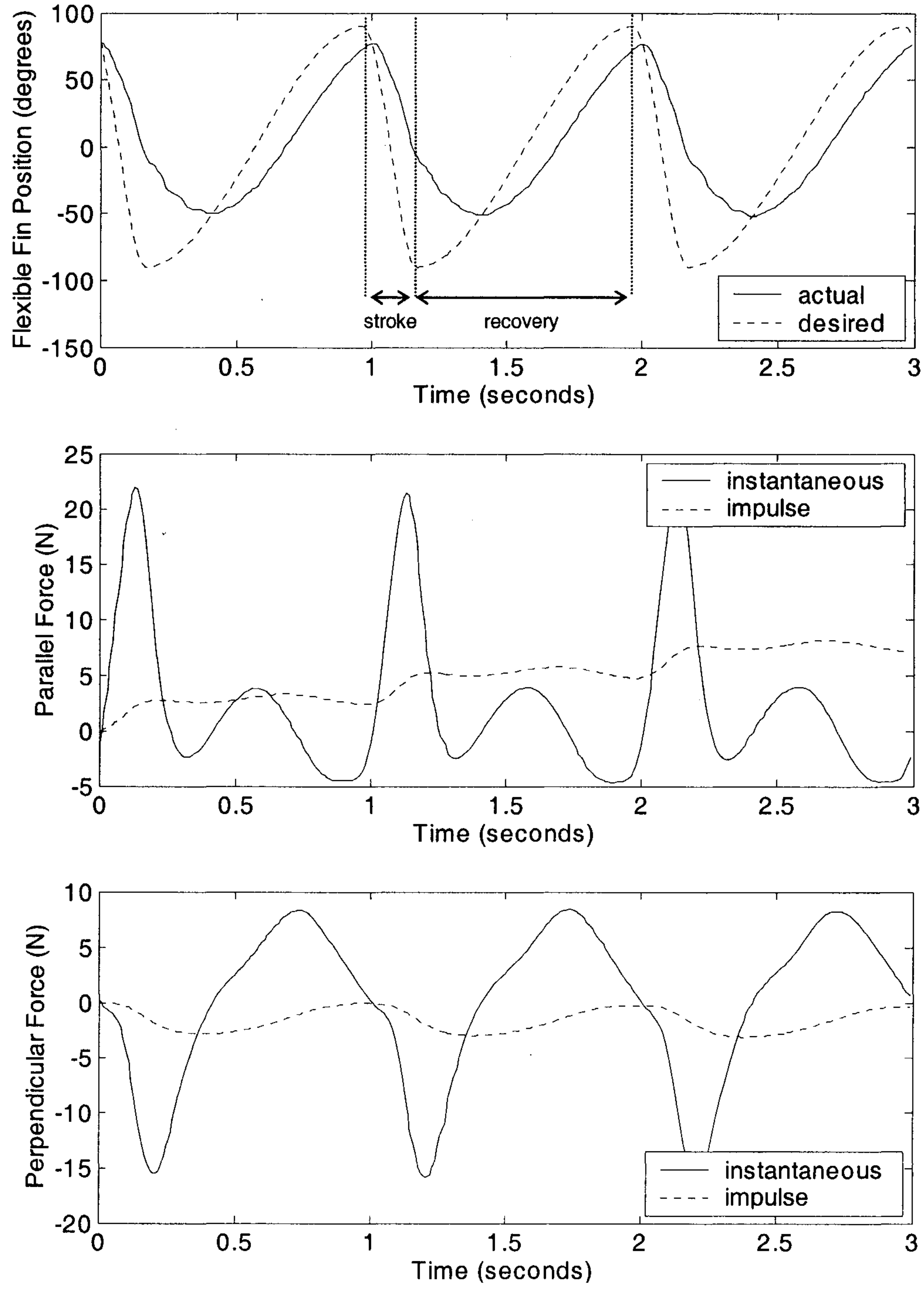

Figure 4-19: Forces generated by the flexible fin as it performed oscillations having a desired amplitude of 180°, but an actual amplitude of 130°, a period of 1s and an oscillation ratio of 0.2.

Dividing the time-averaged forces of Table 4.2 by the average power required to perform the different oscillations resulted in the power-normalized forces shown in Table 4.3. It is interesting to notice that oscillations having an oscillation ratio of 0.3, 0.4 and 0.5 produce the same force for a given amount of power. The oscillation having an oscillation ratio of 0.2 appears to be more efficient than the others. In general, asymmetric strokes appear to promise an advantage in producing more thrust, but at the cost of proportionally more power.

Oscillation ratio	Power-normalized parallel time-averaged force (N/W)	Power-normalized perpendicular time-averaged force (N/W)
0.2	0.44	-0.03
0.3	0.35	-0.07
0.4	0.34	-0.02
0.5	0.34	0.01

Table 4.3: Power-normalized time-averaged parallel and perpendicular forces generated by paddles undergoing trajectories with amplitude A = 130°, period T = 1s, offset angle γ_0 = 0° and oscillation ratios R of 0.2, 0.3, 0.4 and 0.5.

4.4. Thrust Measuring Setup Conclusions

Experiments were performed on the thrust measuring setup with a rigid paddle in order to validate the rigid paddle model presented in Chapter 2. The rigid paddle performed oscillations at four different periods (0.4 seconds, 0.6 seconds, 0.8 seconds and 1 second) and eight different amplitudes (20° to 90° in increments of 10°) for each period. For all oscillations, the paddle did not track the desired trajectory accurately: the actual amplitude of oscillation was smaller than the desired one. This was due to the time lag between the desired position and the actual one.

Noise from the transducer as well as noise at two distinct frequencies, 16Hz and 47Hz, were present in the force/torque measurements of all experiments. The two distinct frequencies correspond to the natural frequencies of the thrust measuring setup. A double-pass third-order Butterworth filter with a cutoff frequency of 7Hz was applied to force and torque measurements of all experiments in order to attenuate the higher frequency noise.

The time-averaged parallel experimental forces indicated that larger parallel forces could be obtained with paddle oscillations of shorter periods and larger amplitudes. The cycle-averaged parallel experimental forces indicated that smaller period oscillations produce slightly larger parallel forces per oscillation. The power required to perform the different oscillations indicated however that smaller period oscillations require greater power. Dividing the time-averaged forces by the power required to perform the different oscillations showed that the oscillation parameters which produce the greatest net thrust per unit power are a period of 1 second and an amplitude of 30°.

The rigid paddle experimental results were compared to the results of rigid paddle model simulations. A good match was observed between the two sets of results, indicating that experimental inflow was estimated correctly in the simulations. As stated in chapter 3, measuring entrained flow would have eliminated the need to estimate it and it is recommended to add a flow velocity sensor on the thrust measuring setup for future experiments.

Two parameters were extracted from the rigid paddle experiments. First, an added mass coefficient of $0.0078 kg{\cdot}m^2$ was obtained. Second, a characteristic length ranging between 12.2cm and 15.0cm was obtained.

Tests were also performed with different flexible fins. In all experiments, the flexible fin tracked the desired trajectory more accurately than did the rigid paddle. The flexible fin was shown to produce greater time-averaged forces than the rigid paddle, but does so only slightly more efficiently than the rigid paddle.

An oscillation whose stroke phase is faster than its recovery phase was tested. The asymmetry in the gait is characterized by the oscillation ratio. Trajectories with smaller oscillation ratios generate greater parallel time-averaged forces. Dividing the time-averaged forces by the power required indicated that oscillations with oscillation ratios of 0.3, 0.4 and 0.5 produce the same forces for a given amount of power. Oscillations with oscillation ratios of 0.2 produce greater forces per Watt. In the future, an optimization should be performed to find the types of oscillation as well as the oscillation parameters that produce the maximum amount of thrust, and the most efficient thrust generation.

5. Numerical Simulation

As discussed in the introduction, the goal of this research was to develop a simulation of a hexapod underwater robot. The greatest difficulty lay in characterizing the paddles accurately, and that task was undertaken first. A model predicting the forces and moments generated by a rigid paddle oscillating in the water was presented in Chapter 2 and that model was validated with experiments presented in Chapter 4. This chapter presents a simulation of the robot, which uses the validated rigid paddle model.

Section 5.1 lists the basic assumptions that were made in the simulation of AQUA. The equations of motion of a rigid body in water are then derived in Section 5.2. Mass, moments of inertia and hydrodynamic derivatives terms in the equations of motion are determined in Section 5.3. The forces and moments in the equations of motion are due to gravitational, buoyancy, hydrodynamic and propulsive effects. The four types of forces and moments are calculated in Section 5.4. The expanded equations of motion are presented in Section 5.6, and Section 5.7 explains how those equations were solved. Section 5.8 discusses the animation of the time-varying position and orientation of the robot in order to help visualization of the results.

5.1. Assumptions and Reference Frames

The following assumptions were made in the simulation of AQUA:

- The underwater vehicle is moving in a stationary body of water having constant properties
- The underwater vehicle is rigid
- The underwater vehicle is of constant mass
- The acceleration due to gravity is constant.
- The accelerations of the underwater vehicle due to motion about a curved rotating Earth are negligible

The body of the robot is modeled as a rectangular prism. Attached to the body is the coordinate frame *xyz*, which has its origin at the center of mass of the body, its x-axis pointing forward, its y-axis out the right side and its z-axis pointing downward, as shown in Figure 5-1. *XYZ* is an inertial coordinate frame. Its origin is at some arbitrary fixed point on the sea surface, its Z-axis is pointing down and its X-axis is pointing toward the North. The orientation of *xyz* relative to *XYZ* is specified by the Euler angles (ϕ, θ, ψ), where ϕ is the roll angle, θ is the pitch angle, and ψ is the yaw angle [52].

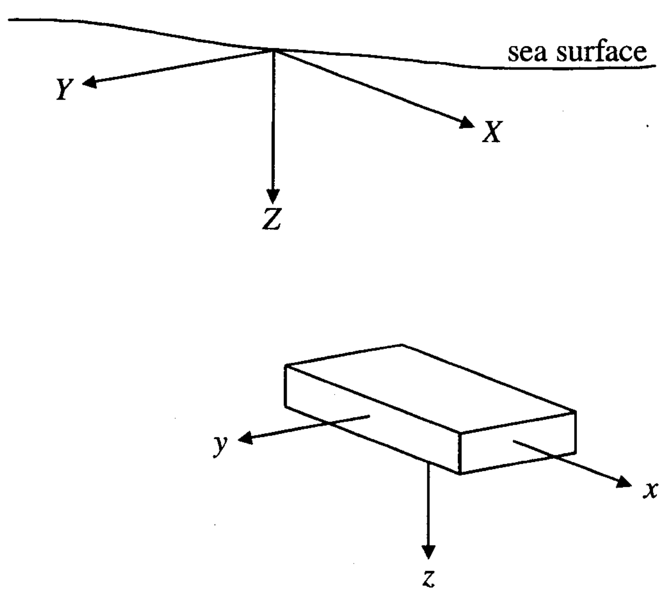

Figure 5-1: Inertial coordinate frame *XYZ* and robot-fixed coordinate frame *xyz*.

5.2. Derivations of the Equations of Motion

The robot has six degrees of freedom: surge, sway, heave, roll, pitch and yaw. These are shown in Figure 5-2. The translational motions (surge, sway and heave) obey Newton's law and the rotational motions (roll, pitch and yaw) are governed by Euler's equation. Fossen derived the rigid-body dynamics of a marine vehicle [53], and expressed the 6 DOF nonlinear dynamic equations of motion as:

$$\vec{F} = \boldsymbol{M}\,\dot{\vec{v}} + \boldsymbol{C}(\vec{v})\vec{v} \tag{5.1}$$

where $\vec{F}$ is a vector of forces and moments acting on the rigid body, $\boldsymbol{M}$ is the inertia matrix, $\boldsymbol{C}(\vec{v})$ is the matrix of Coriolis and centripetal terms and $\dot{\vec{v}}$ and $\vec{v}$ are the acceleration and velocity vectors of the robot's center of mass with respect to the body-fixed frame. Vector $\vec{v} = [u\ v\ w\ p\ q\ r]^T$, where u, v and w are the components of velocity of the mass center along the x-, y- and z-axes and p, q and r are the components of body angular velocity about the x-, y- and z-axes.

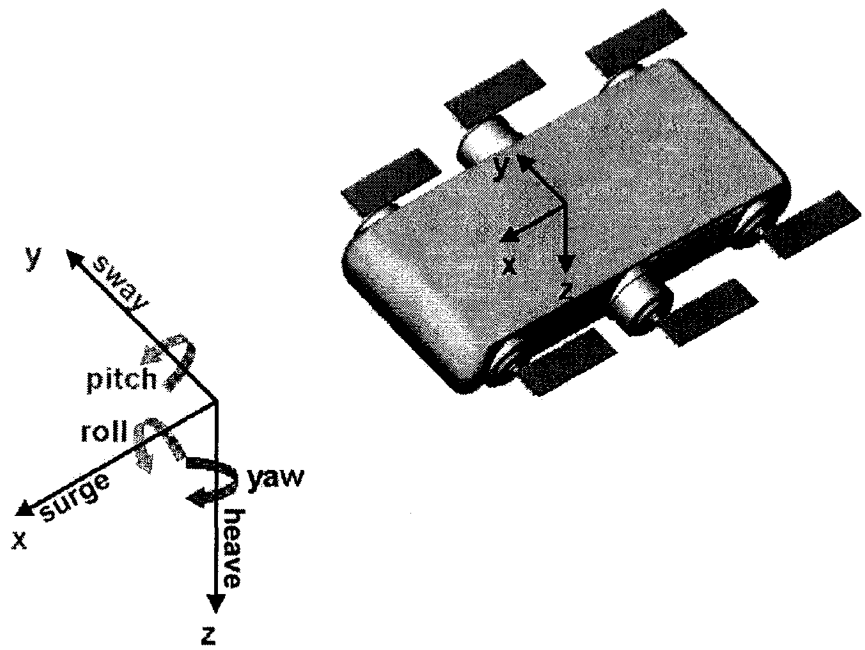

Figure 5-2: Six degrees of freedom of the robot.

When a body is accelerated in water, the fluid surrounding it is also accelerated. The concept of added mass represents the effect of fluid being accelerated by the body. The added mass forces and moments are contained in an added inertia matrix M_A and a matrix of added hydrodynamic Coriolis and centripetal terms $C_A(\vec{v})$.

Matrix M in Equation (5.1) is equal to $M_{RB} + M_A$, where M_{RB} is the rigid-body inertia matrix and M_A is the added inertia matrix. Matrix $C(\vec{v})$ is equal to $C_{RB}(\vec{v}) + C_A(\vec{v})$, where $C_{RB}(\vec{v})$ is the rigid-body Coriolis and centripetal matrix and $C_A(\vec{v})$ is the matrix of added hydrodynamic Coriolis and centripetal terms.

The rigid-body inertia matrix $\boldsymbol{M}_{RB}$ and the rigid-body Coriolis and centripetal matrix $\boldsymbol{C}_{RB}(\vec{v})$ are given by

$$\boldsymbol{M}_{RB} = \begin{bmatrix} m & 0 & 0 & 0 & 0 & 0 \\ 0 & m & 0 & 0 & 0 & 0 \\ 0 & 0 & m & 0 & 0 & 0 \\ 0 & 0 & 0 & I_{xx} & -I_{xy} & -I_{xz} \\ 0 & 0 & 0 & -I_{xy} & I_{yy} & -I_{yz} \\ 0 & 0 & 0 & -I_{xz} & -I_{yz} & I_{zz} \end{bmatrix} \tag{5.2}$$

$$\boldsymbol{C}_{RB}(\vec{v}) = \begin{bmatrix} 0 & 0 & 0 & 0 & mw & -mv \\ 0 & 0 & 0 & -mw & 0 & mu \\ 0 & 0 & 0 & mv & -mu & 0 \\ 0 & 0 & 0 & 0 & -I_{yz}q - I_{xz}p + I_{zz}r & I_{yz}r + I_{xy}p - I_{yy}q \\ 0 & 0 & 0 & I_{yz}q + I_{xz}p - I_{zz}r & 0 & -I_{xz}r - I_{xy}q + I_{xx}p \\ 0 & 0 & 0 & -I_{yz}r - I_{xy}p + I_{yy}q & I_{xz}r + I_{xy}q - I_{xx}p & 0 \end{bmatrix} \tag{5.3}$$

where m is the mass of the robot, I_{xx}, I_{yy} and I_{zz} are the moments of inertia of the robot about the x-, y- and z-axes and I_{xy}, I_{xz} and I_{yz} are the products of inertia.

In underwater applications, like AQUA, where the vehicle moves at low speed and has three planes of symmetry, $\boldsymbol{M}_A$ and $\boldsymbol{C}_A(\vec{v})$ are as follows [53]:

$$\boldsymbol{M}_A = \begin{bmatrix} -X_{\dot{u}} & 0 & 0 & 0 & 0 & 0 \\ 0 & -Y_{\dot{v}} & 0 & 0 & 0 & 0 \\ 0 & 0 & -Z_{\dot{w}} & 0 & 0 & 0 \\ 0 & 0 & 0 & -L_{\dot{p}} & 0 & 0 \\ 0 & 0 & 0 & 0 & -M_{\dot{q}} & 0 \\ 0 & 0 & 0 & 0 & 0 & -N_{\dot{r}} \end{bmatrix} \tag{5.4}$$

The terms in the 6×6 added mass matrix $\boldsymbol{M}_A$ are called hydrodynamic derivatives; $X_{\dot{u}}$, $Y_{\dot{v}}$ and $Z_{\dot{w}}$ have units of mass (kg) while $L_{\dot{p}}$, $M_{\dot{q}}$ and $N_{\dot{r}}$ have units of moments of inertia (kg·m^2).

$$\boldsymbol{C}_A(\vec{v}) = \begin{bmatrix} 0 & 0 & 0 & 0 & -Z_{\dot{w}}w & Y_{\dot{v}}v \\ 0 & 0 & 0 & Z_{\dot{w}}w & 0 & -X_{\dot{u}}u \\ 0 & 0 & 0 & -Y_{\dot{v}}v & X_{\dot{u}}u & 0 \\ 0 & -Z_{\dot{w}}w & Y_{\dot{v}}v & 0 & -N_{\dot{r}}r & M_{\dot{q}}q \\ Z_{\dot{w}}w & 0 & -X_{\dot{u}}u & N_{\dot{r}}r & 0 & -L_{\dot{p}}p \\ -Y_{\dot{v}}v & X_{\dot{u}}u & 0 & -M_{\dot{q}}q & L_{\dot{p}}p & 0 \end{bmatrix} \tag{5.5}$$

In general, the added mass coefficients are different for each direction of motion of the body. For example, the hydrodynamic force in the x-direction due to $\dot{u}$ is equal to $X_{\dot{u}}\dot{u}$, where $\dot{u}$ is the acceleration in the x-direction and $X_{\dot{u}}$ is defined as $X_{\dot{u}} = \dfrac{\partial F_x}{\partial \dot{u}}$. The other hydrodynamic derivatives $Y_{\dot{v}}$, $Z_{\dot{w}}$, $L_{\dot{p}}$, $M_{\dot{q}}$ and $N_{\dot{r}}$ are also defined as partial derivatives of forces or moments with respect to accelerations.

Equation (5.1) can be expanded to obtain the following six non-linear, coupled differential equations of motion:

$$F_{cm\,x} = m\,(\dot{u} - vr + wq) - X_{\dot{u}}\dot{u} - Z_{\dot{w}}wq + Y_{\dot{v}}vr \tag{5.6}$$

$$F_{cm\,y} = m\,(\dot{v} - wp + ur) - Y_{\dot{v}}\dot{v} + Z_{\dot{w}}wp - X_{\dot{u}}ur \tag{5.7}$$

$$F_{cm\,z} = m\,(\dot{w} - uq + vp) - Z_{\dot{w}}\dot{w} - Y_{\dot{v}}vp + X_{\dot{u}}uq \tag{5.8}$$

where $F_{cm\,x}$, $F_{cm\,y}$ and $F_{cm\,z}$ are components of $\vec{F}_{cm}$, the total external force acting at the center of mass of the robot, along the x-, y- and z-axes.

$$\begin{aligned} M_{cm\,x} = {} & I_{xx}\dot{p} + (I_{zz} - I_{yy})\,qr - (\dot{r} + pq)\,I_{xz} + (r^2 - q^2)\,I_{yz} + \\ & (pr - \dot{q})\,I_{xy} - L_{\dot{p}}\dot{p} + (Y_{\dot{v}} - Z_{\dot{w}})vw + (M_{\dot{q}} - N_{\dot{r}})qr \end{aligned} \tag{5.9}$$

$$M_{cm\,y} = I_{yy}\dot{q} + (I_{xx} - I_{zz})\,rp - (\dot{p} + qr)\,I_{xy} + (p^2 - r^2)\,I_{xz} + \\ (qp - \dot{r})\,I_{yz} - M_{\dot{q}}\dot{q} + (Z_{\dot{w}} - X_{\dot{u}})uw + (N_{\dot{r}} - L_{\dot{p}})\,pr \tag{5.10}$$

$$M_{cm\,z} = I_{zz}\dot{r} + (I_{yy} - I_{xx})\,pq - (\dot{q} + rp)\,I_{yz} + (q^2 - p^2)\,I_{xy} + \\ (rq - \dot{p})\,I_{xz} - N_{\dot{r}}\dot{r} + (X_{\dot{u}} - Y_{\dot{v}})uv + (L_{\dot{p}} - M_{\dot{q}})\,pq \tag{5.11}$$

where $M_{cm\,x}$, $M_{cm\,y}$ and $M_{cm\,z}$ are components of $\vec{M}_{cm}$, the total external moment acting at the center of mass of the robot, about the x-, y- and z- axes.

5.3. Determination of Mass, Moments of Inertia and Hydrodynamic Derivatives

AQUA, shown in Figure 5-3, is a neutrally buoyant robot. This means that it weighs as much as the volume of water it displaces. The body of the robot is approximated as a rectangular parallelepiped having a length L of 0.66m, a width B of 0.21m and a height H of 0.13m, which is illustrated (not to scale) in Figure 5-4. The volume of the robot is 0.018 m^3 and the mass of that volume of water is 18.0kg.

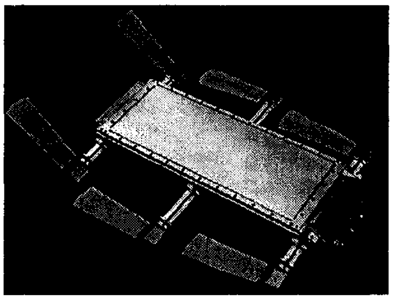

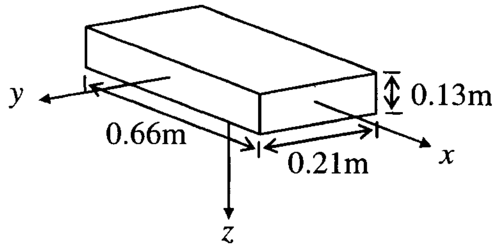

Figure 5-3 (left): AQUA. **Figure 5-4 (right):** Rectangular parallelipiped approximating AQUA.

The robot is approximated to be a homogeneous solid. Formulas for the moments of inertia of a homogeneous rectangular parallelepiped were used to calculate an I_{xx} of 0.091kg·m^2, an I_{yy} of 0.68kg·m^2 and an I_{zz} of 0.72kg·m^2. The products of inertia I_{xy}, I_{xz} and I_{yz} are all equal to zero since the robot has three planes of symmetry.

Fossen states that, for slender bodies, an estimate of the added mass hydrodynamic derivatives can be obtained by applying strip theory. AQUA was approximated as a slender body and its six added mass hydrodynamic derivatives were estimated using strip theory.

5.3.1. Calculation of Added Mass Coefficients Using Strip Theory

The principle of strip theory involves dividing the submerged vehicle into a number of strips. AQUA is therefore approximated to be a rectangular prism and divided into strips. Then, two-dimensional added mass hydrodynamic derivatives are computed for each strip and integrated over the third dimension. For a submerged slender vehicle the following formulas for three-dimensional added mass hydrodynamic derivatives can be used [53]:

$$A_{11} = -X_{\dot{u}} = \int_{-L/2}^{L/2} A_{11}^{(2D)}(y,z)dx \tag{5.12}$$

$$A_{22} = -Y_{\dot{v}} = \int_{-L/2}^{L/2} A_{22}^{(2D)}(y,z)dx \tag{5.13}$$

$$A_{33} = -Z_{\dot{w}} = \int_{-L/2}^{L/2} A_{33}^{(2D)}(y,z)dx \tag{5.14}$$

$$A_{44} = -L_{\dot{p}} = \int_{-L/2}^{L/2} A_{44}^{(2D)}(y,z)dx = \int_{-B/2}^{B/2} y^2 A_{33}^{(2D)}(x,z)dy + \int_{-H/2}^{H/2} z^2 A_{22}^{(2D)}(x,y)dz \tag{5.15}$$

$$A_{55} = -M_{\dot{q}} = \int_{-L/2}^{L/2} A_{55}^{(2D)}(y,z)dx = \int_{-L/2}^{L/2} x^2 A_{33}^{(2D)}(y,z)dx + \int_{-H/2}^{H/2} z^2 A_{11}^{(2D)}(x,y)dz \tag{5.16}$$

$$A_{66} = -N_{\dot{r}} = \int_{-L/2}^{L/2} A_{66}^{(2D)}(y,z)dx = \int_{-B/2}^{B/2} y^2 A_{11}^{(2D)}(x,z)dy + \int_{-L/2}^{L/2} x^2 A_{22}^{(2D)}(y,z)dx \tag{5.17}$$

where $L = 0.66$m, $B = 0.21$m and $H = 0.13$m.

The added mass depends on the shape of the body. $A_{11}^{(2D)}(y,z)$, $A_{11}^{(2D)}(x,y)$, $A_{11}^{(2D)}(x,z)$, $A_{22}^{(2D)}(x,y)$, $A_{22}^{(2D)}(y,z)$, $A_{33}^{(2D)}(x,z)$ and $A_{33}^{(2D)}(y,z)$ were computed using experimentally obtained two-dimensional added mass derivatives for a rectangular cross-section of width *2a* and height *2b*. This cross-section and its direction of motion are shown in Figure 5-5.

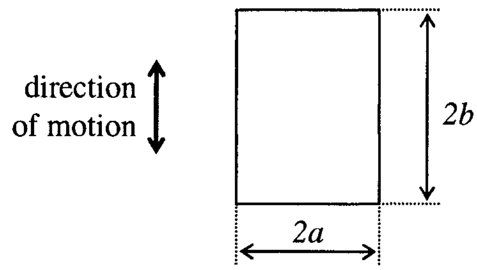

Figure 5-5: Rectangular cross-section of width *2a* and height *2b* having a direction of motion parallel to *2b*.

The subscript i in $A_{ii}^{(2D)}$ represents the direction of motion of the rectangular prism, where $i = 1, 2$ and 3 corresponds to motion along the x-, y- and z-axes of the prism respectively. The indices in the parentheses following $A_{ii}^{(2D)}$ indicate the plane in which the rectangular cross-section is taken. In Figure 5-5, the dimension *2b* corresponds to the cross-section dimension parallel to the direction of motion of the rectangular prism. The dimension *2a* corresponds to the other cross-section dimension. The only two-dimensional added mass derivative that does not follow this convention is $A_{11}^{(2D)}(y,z)$.

The two-dimensional added mass hydrodynamic derivatives of the AQUA robot were calculated from Table 5.1 [54].

a/b	$k = \dfrac{A_{ii}^{(2D)}}{\pi\rho a^2}$, where $i = 1, 2$ or 3
∞	1
10	1.14
5	1.21
2	1.36
1	1.51
0.5	1.70
0.2	1.98
0.1	2.23

Table 5.1: Coefficients used in calculation of two-dimensional added mass hydrodynamic derivatives of a parallelepiped of width *2a* and height *2b* moving in the direction shown in Figure 5-5 [54].

Then, the three-dimensional added mass hydrodynamic derivatives were calculated from Equations (5.12) to (5.17). Values of these derivatives are recorded in Table 5.2.

Hydrodynamic derivatives	
$-X_{\dot{u}}$	6.98kg
$-Y_{\dot{v}}$	14.50kg
$-Z_{\dot{w}}$	32.41kg
$-L_{\dot{p}}$	0.40kg·m^2
$-M_{\dot{q}}$	1.19kg·m^2
$-N_{\dot{r}}$	0.55kg·m^2

Table 5.2: Three-dimensional added mass hydrodynamic derivatives of a rectangular parallelepiped having a length $L = 0.66$m, a width $B = 0.21$m and a height $H = 0.13$m.

5.4. Calculation of Forces and Moments

The force $\vec{F}_{cm}$ and moment $\vec{M}_{cm}$ are generated by the following effects: gravitational, buoyancy, hydrodynamic and propulsive:

$$\vec{F}_{cm} = \vec{F}_g + \vec{B} + \vec{F}_p + \vec{F}_h \tag{5.18}$$

where $\vec{F}_g$ is the gravitational force, $\vec{B}$ is the buoyancy force, $\vec{F}_p$ is the propulsive force and $\vec{F}_h$ is the hydrodynamic force.

$$\vec{M}_{cm} = \vec{M}_b + \vec{M}_p + \vec{M}_h \tag{5.19}$$

where $\vec{M}_b$ is the buoyancy moment, $\vec{M}_p$ is the propulsive moment and $\vec{M}_h$ is the hydrodynamic moment.

These forces and moments are discussed in more detail in the following subsections.

5.4.1. Gravitational Force

The gravitational force $\vec{F}_g$ acts through the center of mass of the robot and is directed in the positive direction of the Z-axis of the inertial frame. It is equal to $m\vec{g}$, where m is the mass of the robot and $\vec{g}$ is the gravitational acceleration.

The rotation matrix $\boldsymbol{T}$ transforms vectors in the body-fixed frame into vectors in the inertial frame.

$$\boldsymbol{T} = \begin{bmatrix} c\psi\, c\theta & -s\psi\, c\phi + c\psi\, s\theta\, s\phi & s\psi\, s\phi + c\psi\, c\phi\, s\theta \\ s\psi\, c\theta & c\psi\, c\phi + s\phi\, s\theta\, s\psi & -c\psi\, s\phi + s\theta\, s\psi\, c\phi \\ -s\theta & c\theta\, s\phi & c\theta\, c\phi \end{bmatrix} \tag{5.20}$$

where $s\cdot \equiv \sin(\cdot)$, $c\cdot \equiv \cos(\cdot)$

Correspondingly, the inverse of the rotation matrix, which is simply its transpose, $\boldsymbol{T}^{\mathrm{T}}$, transforms vectors in the inertial frame into vectors in the body-fixed frame.

Thus, the gravitational force $[0\ 0\ mg]^{\mathrm{T}}$ is pre-multiplied by $\boldsymbol{T}^{\mathrm{T}}$ to give

$$\vec{F}_g = \begin{bmatrix} F_{gx} \\ F_{gy} \\ F_{gz} \end{bmatrix} = \begin{bmatrix} -mg\sin\theta \\ mg\sin\phi\cos\theta \\ mg\cos\phi\cos\theta \end{bmatrix} \tag{5.21}$$

Since the gravitational force acts through the center of mass, it produces no moment about the center of mass.

5.4.2. Buoyancy Force and Moment

The buoyancy force $\vec{B}$ passes through the volumetric center of the robot and acts in the negative Z-direction of the inertial frame. It is equal to the weight of the water displaced by the robot and has a magnitude equal to $V\rho\, g$, where V is the volume of the robot, ρ is the density of the water and g is the magnitude of the gravitational acceleration.

The buoyancy force $[0 \quad 0 \quad -V\rho g]^{\mathrm{T}}$ is pre-multiplied by $\boldsymbol{T}^{\mathrm{T}}$ to give

$$\vec{B} = \begin{bmatrix} B_x \\ B_y \\ B_z \end{bmatrix} = \begin{bmatrix} V\rho g \sin\theta \\ -V\rho g \sin\phi \cos\theta \\ -V\rho g \cos\phi \cos\theta \end{bmatrix} \tag{5.22}$$

The buoyancy moment $\vec{M}_b$ is the cross product between the position of the center of buoyancy with respect to the center of mass, and the buoyancy force. It is equal to:

$$\begin{aligned} \vec{M}_b = \begin{bmatrix} M_{bx} \\ M_{by} \\ M_{bz} \end{bmatrix} &= \begin{bmatrix} x_b \\ y_b \\ z_b \end{bmatrix} \times \begin{bmatrix} V\rho g \sin\theta \\ -V\rho g \sin\phi \cos\theta \\ -V\rho g \cos\phi \cos\theta \end{bmatrix} \\ &= \begin{bmatrix} -y_b(V\rho g \cos\phi\cos\theta) + z_b(V\rho g \sin\phi\cos\theta) \\ x_b(V\rho g \cos\phi\cos\theta) + z_b(V\rho g \sin\theta) \\ -x_b(V\rho g \sin\phi\cos\theta) - y_b(V\rho g \sin\theta) \end{bmatrix} \end{aligned} \tag{5.23}$$

where x_b, y_b and z_b are the distances from the center of mass to the center of buoyancy along the x-, y- and z-axes. If the center of mass coincides with the volumetric center of the robot, x_b, y_b and z_b are zero and the buoyancy moment is null. In the simulation, it was assumed that the center of mass and the volumetric center coincide and x_b, y_b and z_b were set to zero.

5.4.3. Hydrodynamic Force and Moment

The hydrodynamic force $\vec{F}_h$ is a function of the vehicle motion and its geometry. It is calculated from relations derived for solid blocks with sharp edges in an unbounded, smooth, uniform, low-speed flow [55]. Typically, bodies with sharp edges have drag coefficients that do not vary significantly with Reynolds number [56]. It is expected that drag coefficient estimates be valid for a wide range of Reynolds numbers. The relations that the hydrodynamic force was calculated from are valid for a free-stream Reynolds number between 10^4 and 10^6. In the simulation of AQUA, the Reynolds number is approximately 1.5×10^4 at a vehicle speed of 0.2m/s.

It is not straightforward to find relations for the calculation of the hydrodynamic force acting on a rectangular prism having the free stream at an arbitrary angle with respect to it. Relations were found for an isolated block having the free stream normal to one of its faces. To calculate the hydrodynamic force on a block having the free stream at other angles, these relations were used in conjunction with the following assumption.

The drag force on the body of the robot is taken to be the vector sum of the drag forces acting on the three faces of the parallelepiped exposed to the incoming flow. If the robot has velocities u, v and w along the x-, y- and z-axes, each relative flow velocity component causes a drag force on the exposed face of the prism to which it is perpendicular. The drag force on each of the three faces is equal to $0.5\rho C_{Di} A_i v_i^2$, where $i = x$, y or z and, C_{Di} is the drag coefficient of the corresponding face, A_i is the area of the face and v_i is the relative flow velocity component perpendicular to the face. Table 5.3 and Figure 5-6 give C_{Di}, A_i and v_i for the three faces of the robot exposed to the incoming flow.

Face perpendicular to	C_{Di}	A_i	v_i magnitude
x-axis	C_{Dx}	BH	u
y-axis	C_{Dy}	LH	v
z-axis	C_{Dz}	BL	w

Table 5.3: Drag coefficient C_{Di}, area A_i and component of relative flow velocity v_i perpendicular to the face for the three faces of the rectangular prism exposed to the incoming flow.

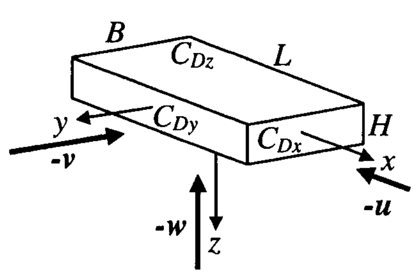

Figure 5-6: Drag coefficient, area and component of relative flow velocity perpendicular to the face for the three faces of the rectangular prism exposed to the incoming flow.

Coefficients C_{Dx}, C_{Dy} and C_{Dz} are the drag coefficients of the front, the right and the top faces of the robot. They were found from a set of data for rectangular prisms having the free stream normal to one face [55]. Based on the dimensions of the prism, the data set gives the drag coefficient of the face to which the free stream is perpendicular. A prism having AQUA's dimensions has C_{Dx}, C_{Dy} and C_{Dz} equal to 0.90, 1.08 and 1.22 respectively.

The drag forces along the x-, y- and z-axes are F_{hx}, F_{hy} and F_{hz} respectively. The hydrodynamic force vector acting on the robot is equal to:

$$\vec{F}_h = \begin{bmatrix} F_{hx} \\ F_{hy} \\ F_{hz} \end{bmatrix} = \begin{bmatrix} 0.5\rho C_{Dx} BH u^2 \\ 0.5\rho C_{Dy} LH v^2 \\ 0.5\rho C_{Dz} BL w^2 \end{bmatrix} \tag{5.24}$$

The robot rotates with velocities p, q and r about the x-, y- and z-axes respectively, as illustrated in Figure 5-7.

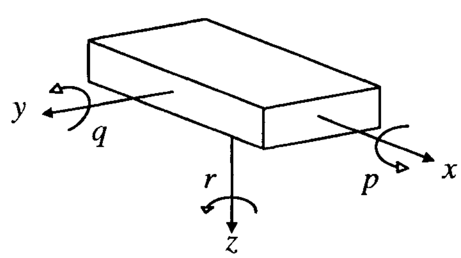

Figure 5-7: Angular rotations p, q, r of the robot about the x-, y- and z-axes respectively.

These angular velocities cause each point of the robot to have a velocity $\vec{v} = \vec{v}_{cm} + \vec{\omega} \times \vec{r}$, where $\vec{v}_{cm} = [u \quad v \quad w]^{\mathrm{T}}$ is the velocity of the center of mass, $\vec{\omega} = [p \quad q \quad r]^{\mathrm{T}}$ is the angular velocity vector and $\vec{r} = [x \quad y \quad z]^{\mathrm{T}}$ is the position of the point with respect to the center of mass.

In the calculation of hydrodynamic forces and moments, $\vec{v}_{cm}$ and $\vec{\omega} \times \vec{r}$ are treated independently. It is assumed that $\vec{v}_{cm}$ is responsible for the drag forces, which were described earlier in this section, and that $\vec{\omega} \times \vec{r}$ is responsible for the drag moments, which will be described later in this section. Because the drag forces and moments are functions of the square of the velocity, the contributions of $\vec{v}_{cm}$ and $\vec{\omega} \times \vec{r}$ are not truly independent, and the assumption is only a rough approximation. For the calculation of drag moments, the velocity of each point of the robot is given by equation (5.25).

$$\vec{\omega} \times \vec{r} = \begin{bmatrix} p \\ q \\ r \end{bmatrix} \times \begin{bmatrix} x \\ y \\ z \end{bmatrix} = \begin{bmatrix} qz - ry \\ rx - pz \\ py - qx \end{bmatrix} \tag{5.25}$$

Illustrations of the velocities due to these terms of the front, right and top faces of the robot can be seen in Figure 5-8.

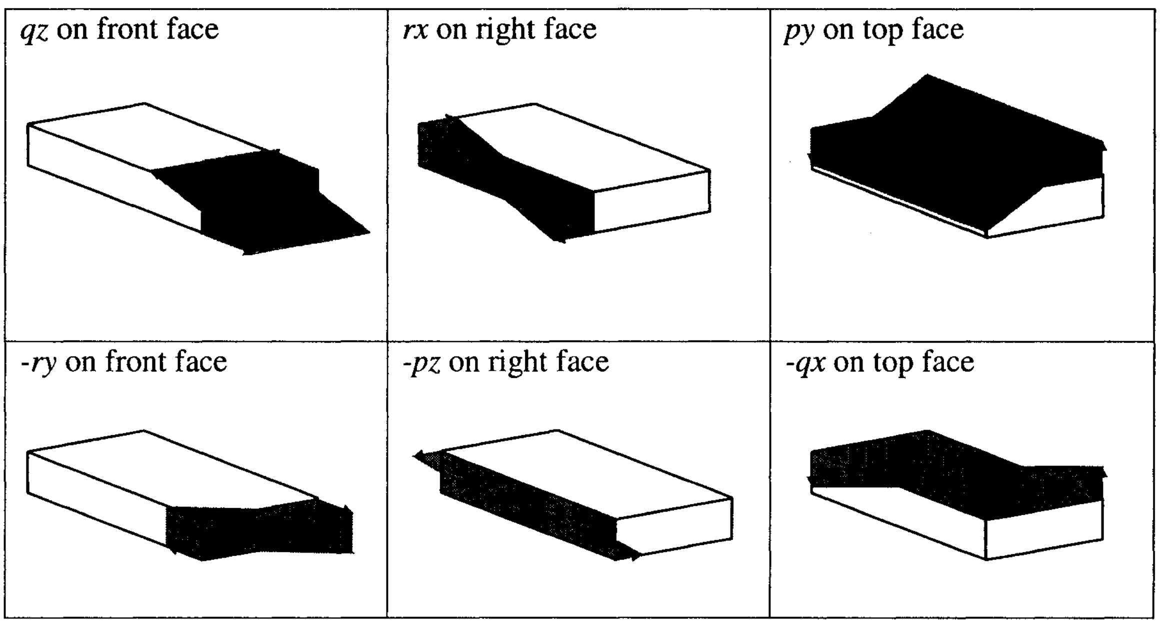

Figure 5-8: Velocities of the front, right and top faces of the robot due to angular velocities p, q and r.

The velocities on the back, left and bottom faces of the robot are the same as those on the front, right and top faces respectively. Figure 5-9 shows the velocity distribution acting on the left and right faces due to a positive yaw rate (i.e. rx in Figure 5-8). The resulting drag forces have a magnitude proportional to the square of the linear velocities and a direction opposite to the linear velocities. Due to symmetry, the drag forces cancel each other out. A similar situation holds true for all velocities illustrated in Figure 5-8.

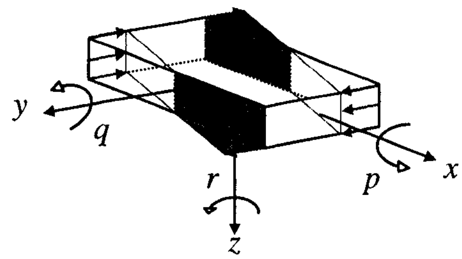

Figure 5-9: Linear velocities on opposing faces of the robot cause drag forces that cancel each other out.

Although the drag forces on opposing faces cancel each other out, they create a drag moment $\vec{M}_h$, hereafter called hydrodynamic moment. In the example of Figure 5-9, that hydrodynamic moment opposes the robot's rotation about the z-axis. The hydrodynamic moments M_{hx}, M_{hy} and M_{hz} are the robot's "resistance" to rotation about the x-, y- and z-axes respectively. M_{hx} is due to linear velocities py on top and bottom faces and $-pz$ on right and left faces and acts in the direction opposite that of p.

The contribution of linear velocities py to M_{hx} is given by

$$M_{hx,py} = 2\int_{-L/2}^{L/2}\int_{0}^{-B/2} D_{py}\, y\, dy dx \tag{5.26}$$

where D_{py} is equal to the drag force per unit area due to py on element $dydx$. D_{py} is given by

$$D_{py} = 0.5\rho C_{Dz}(py)^2 \tag{5.27}$$

where C_{Dz} is the drag coefficient of the face normal to the z-axis.

Substituting equation (5.27) in equation (5.26), the following equation is obtained.

$$M_{hx,py} = \rho C_{Dz}\int_{-L/2}^{L/2}\int_{0}^{-B/2}(py)^2\, y\; dy\, dx = \frac{\rho C_{Dz} p^2 B^4 L}{64} \tag{5.28}$$

The contribution of $-pz$ to M_{hx} is given by

$$M_{hx,-pz} = 2\int_{-L/2}^{L/2}\int_{0}^{-H/2} D_{-pz}\, z\, dz dx \tag{5.29}$$

where D_{-pz} is equal to the drag force per unit area due to $-pz$ on element $dxdz$. D_{-pz} is given by

$$D_{py} = 0.5\rho C_{Dy}(-pz)^2 \tag{5.30}$$

where C_{Dy} is the drag coefficient of the face normal to the y-axis.

Substituting equation (5.30) in (5.29), the following equation is obtained.

$$M_{hx,-pz} = \rho C_{Dy} \int_{-L/2}^{L/2} \int_{0}^{-H/2} (-pz)^2 z \, dz \, dx = \frac{\rho C_{Dy} p^2 H^4 L}{64} \tag{5.31}$$

M_{hx} is the sum of $M_{hx,py}$ and $M_{hx,-pz}$ (equations (5.28) and (5.31)). Similarly, M_{hy} is due to linear velocities qz on front and back faces and $-qx$ on top and bottom faces and acts in the direction opposite that of q. Finally, M_{hz} is due to linear velocities rx on right and left faces and $-ry$ on front and back faces and acts in the direction opposite that of r. Hydrodynamic moments M_{hy} and M_{hz} are calculated similarly to M_{hx}. The resulting values of all hydrodynamic moments M_{hx}, M_{hy} and M_{hz} are given by

$$\vec{M}_h = \begin{bmatrix} M_{hx} \\ M_{hy} \\ M_{hz} \end{bmatrix} = \begin{bmatrix} \dfrac{\rho p^2 L\left(C_{Dz} B^4 + C_{Dy} H^4\right)}{64} \\ \dfrac{\rho q^2 B\left(C_{Dx} H^4 + C_{Dz} L^4\right)}{64} \\ \dfrac{\rho r^2 H\left(C_{Dx} B^4 + C_{Dy} L^4\right)}{64} \end{bmatrix} \tag{5.32}$$

5.4.4. Propulsive Force and Moment

The propulsive force $\vec{F}_p$ of the robot comes from the movement of its paddles, which are modeled as flat plates, as explained in Chapter 2. Each paddle's equation of motion is given by

$$\tau = J\ddot{\gamma} - T_{res} \tag{5.33}$$

where τ is the applied torque. The PD controller generating the applied torque was described in Section 2.3, J is the paddle's moment of inertia, which includes added mass effects. Experimentally, the value of J was found to be 0.0078kg·m^2, as discussed in Section 4.1.7, $\ddot{\gamma}$ is the angular acceleration of the paddle and T_{res} is the resistive torque. The latter represents the water's resistance to the paddle's motion. It is equal to the moment generated by the lift and drag forces about the hip, as explained in Section 2.4.4.1.

For each of the robot's six paddles, equation (5.33) must be solved in order to find the paddle's angular acceleration. The angular acceleration is integrated once to find angular velocity and once more to find angular position. Both angular velocity and position are used to calculate the generated drag and lift forces, as explained in Section 5.5.4.1. These forces are then translated from the hips to the center of mass. Finally, the moments, which are created at the center of mass by these forces are calculated, as explained in Section 5.5.4.2. Figure 5-10 illustrates the actual and the desired angular positions of a paddle oscillating with an amplitude of 90° and a period of 1second. Note that the actual position is practically identical to the desired one. This implies that, for the parameters that have been used in the simulation, equations (3.2) and (5.33) can be bypassed and the actual position can be set to the desired one.

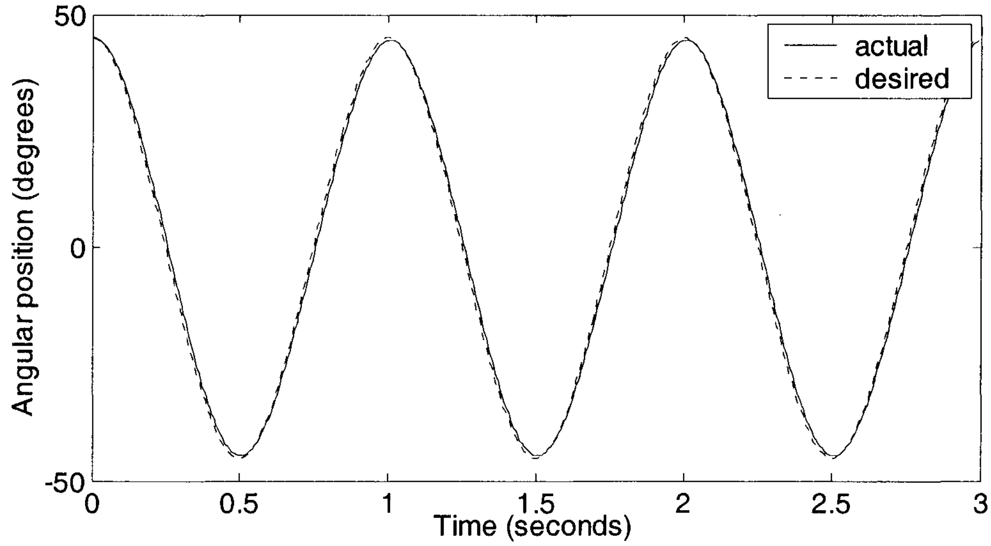

Figure 5-10: Simulated actual and desired angular positions of the paddle oscillating with an amplitude of 90° and a period of 1second.

Equation (5.33) is a simplified expression that neglects the fact that, in addition to oscillating, the paddle is moving with the robot. In the future, it is recommended to write paddle equations of motion that take that fact into account.

5.4.4.1. Generation of Drag, Lift and Resistive Torque

As explained in Section 2.1, lift and drag forces vary with velocity U and angle of attack α. The expressions for lift and drag were given by equations (2.1) and (2.2), which are repeated here.

$$L = 0.5\, \rho U^2 S\, C_{L\max} \sin(2\alpha) \tag{2.1}$$

$$D = 0.5\, \rho\, U^2 S\, C_{D\max} \left(1 - \cos(2\alpha)\right) \tag{2.2}$$

where S is the surface area of the paddle, α is the angle of attack and U is the velocity of the flow relative to the paddle. $C_{L\max}$ and $C_{D\max}$ are the maximum values of lift and drag coefficients of the rigid paddle. They are equal to 0.92 and 1.12 respectively.

In Section 2.1, U was a vector sum of inflow velocity and normal velocity. The normal velocity was due to the motion of the paddle, and was equal in magnitude and opposite in direction to the normal velocity of the paddle. The inflow velocity estimated there was due to the water entrained by the paddle. By contrast, in the simulation of the robot, the inflow is due to the motion of the robot. The robot moves with velocities u, v and w along the x-, y- and z-axes, and angular velocities p, q and r about these axes. The velocity of each hip is a function of u, v, w, p, q and r. The inflow at each hip is taken to be the opposite of the velocity of the hip.

The second difference between the simulation of the rigid paddle experiments and the simulation of the robot relates to the transformation of the lift and drag forces. In Chapter 2, lift and drag were transformed into forces in an inertial frame via equations (2.3) and (2.4). In the simulation of the robot, lift and drag forces created by paddle j are transformed via the same equations into forces in a coordinate frame xyz, which is fixed to the robot at the hip j.

These forces are rewritten as components of $\vec{F}_{pj}$: the propulsive force vector of paddle *j*.

$$\vec{F}_{pj} = \begin{bmatrix} D_j \sin\beta_j + L_j \cos\beta_j \\ 0 \\ -L_j \sin\beta_j + D_j \cos\beta_j \end{bmatrix} \tag{5.34}$$

where D_j and L_j are the drag and lift forces produced by paddle *j* and β_j is the angle, in the *xyz* coordinate frame, of the flow impinging on paddle *j*.

The resistive torque, T_{res} in equation (5.33), is found equation (5.35), which is the cross product between $\vec{P}_j$, the position of the point of pressure in the hip joint-fixed coordinate frame *xyz*, and $\vec{F}_{pj}$, the propulsive force vector. $\vec{P}_j$ and $\vec{F}_{pj}$ can be seen in Figure 5-11. Detailed calculations explaining this point of application can be found in Appendix B. Experimental results presented in Section 4.1.7 indicated that the characteristic length (or point of application of the force) ranged between 0.61 and 0.75 of the paddle length, which corresponds to the calculated point of application at 0.75 of the paddle length, and so the value of 0.75 was used here.

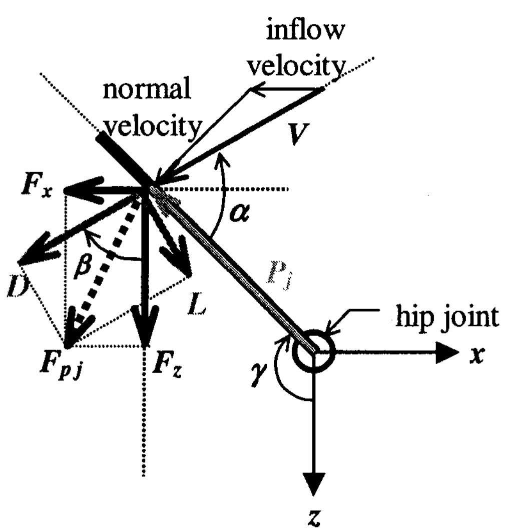

Figure 5-11: Illustration of $\vec{P}_j$, the position of the point of application of the drag and lift forces, and $\vec{F}_{pj}$, the propulsive force vector, in the hip joint-fixed coordinate frame *xz*.

$$\vec{T}_{res} = \vec{P}_j \times \vec{F}_{pj} = \begin{bmatrix} 0.75l\sin\gamma_j \\ 0 \\ 0.75l\cos\gamma_j \end{bmatrix} \times \begin{bmatrix} D_j \sin\beta_j + L_j\cos\beta_j \\ 0 \\ -L_j\sin\beta + D_j\cos\beta_j \end{bmatrix} \tag{5.35}$$

$$= \begin{bmatrix} 0 \\ 0.75l\cos\gamma_j\left(D_j\sin\beta_j + L_j\cos\beta_j\right) - 0.75l\sin\gamma_j\left(-L_j\sin\beta + D_j\cos\beta_j\right) \\ 0 \end{bmatrix}$$

5.4.4.2. Propulsive Force and Moment Vectors Acting on the Center of Mass

The propulsive force creates a moment $\vec{M}_p$, which acts on the center of mass. The propulsive moment due to the propulsive force acting at hip *j* is given by

$$\begin{aligned} \vec{M}_{pj} &= \begin{bmatrix} x_{\text{hip}\,j} \\ y_{\text{hip}\,j} \\ z_{\text{hip}\,j} \end{bmatrix} \times \begin{bmatrix} F_{px\,j} \\ F_{py\,j} \\ F_{pz\,j} \end{bmatrix} = \begin{bmatrix} x_{\text{hip}\,j} \\ y_{\text{hip}\,j} \\ z_{\text{hip}\,j} \end{bmatrix} \times \begin{bmatrix} D_j\sin\beta_j + L_j\cos\beta_j \\ 0 \\ -L_j\sin\beta + D_j\cos\beta_j \end{bmatrix} \\ &= \begin{bmatrix} y_{\text{hip}\,j}\left(-L_j\sin\beta + D_j\cos\beta_j\right) \\ -x_{\text{hip}\,j}\left(-L_j\sin\beta + D_j\cos\beta_j\right) + z_{\text{hip}\,j}\left(D_j\sin\beta_j + L_j\cos\beta_j\right) \\ -y_{\text{hip}\,j}\left(D_j\sin\beta_j + L_j\cos\beta_j\right) \end{bmatrix} \end{aligned} \tag{5.36}$$

where $x_{\text{hip}\,j}$, $y_{\text{hip}\,j}$ and $z_{\text{hip}\,j}$ give the position of hip *j* with respect to the center of mass in the coordinate frame fixed to the robot, and $F_{px\,j}$, $F_{py\,j}$ and $F_{pz\,j}$ are the components of $\vec{F}_{p\,j}$ given by equation (5.34) for paddle *j*.

The propulsive force vector of paddle *j*, $\vec{F}_{pj}$, is translated from hip *j* to the center of mass of the robot, for $j = 1\ldots6$. The total propulsive force along the *x*-, *y*- and *z*-axes is the sum of the six propulsive forces along the *x*-, *y*- and *z*-axes. The components of the total propulsive force are given by

$$F_{px} = \sum_{j=1}^{6}\left(D_j\sin\beta_j + L_j\cos\beta_j\right) \tag{5.37}$$

$$F_{py} = 0 \tag{5.38}$$

$$F_{pz} = \sum_{j=1}^{6}\left(-L_j\sin\beta + D_j\cos\beta_j\right) \tag{5.39}$$

The total propulsive moment at the center of mass about the x-, y- and z-axes is the sum of the moments generated by the six propulsive forces at the center of mass about the x-, y- and z-axes. They are given by

$$M_{px} = \sum_{j=1}^{6} \left(y_{\text{hip}\,j} \left(-L_j \sin\beta + D_j \cos\beta_j \right) \right) \tag{5.40}$$

$$M_{py} = \sum_{j=1}^{6} \left(-x_{\text{hip}\,j} \left(-L_j \sin\beta + D_j \cos\beta_j \right) + z_{\text{hip}\,j} \left(D_j \sin\beta_j + L_j \cos\beta_j \right) \right) \tag{5.41}$$

$$M_{pz} = \sum_{j=1}^{6} \left(-y_{\text{hip}\,j} \left(D_j \sin\beta_j + L_j \cos\beta_j \right) \right) \tag{5.42}$$

5.5. Equations of Motion

Once the gravity, buoyancy, hydrodynamic and propulsive force and moment expressions (equations (5.21), (5.22), (5.23), (5.24), (5.32), and (5.37) to (5.42)) are substituted into equations (5.6) to (5.11), the following six differential equations are obtained:

$$\begin{aligned} &-(mg - V\rho g)\sin\theta + \sum_{j=1}^{6} \left(D_j \sin\beta_j + L_j \cos\beta_j \right) + 0.5\rho C_{dx} BH u^2 = \\ &m(\dot{u} - vr + wq) - X_{\dot{u}}\dot{u} - Z_{\dot{w}} wq + Y_{\dot{v}} vr \end{aligned} \tag{5.43}$$

$$\begin{aligned} &(mg - V\rho g)\sin\phi\cos\theta + 0.5\rho C_{dy} LH v^2 = \\ &m(\dot{v} - wp + ur) - Y_{\dot{v}}\dot{v} + Z_{\dot{w}} wp - X_{\dot{u}} ur \end{aligned} \tag{5.44}$$

$$\begin{aligned} &(mg - V\rho g)\cos\phi\cos\theta + \sum_{j=1}^{6} \left(-L_j \sin\beta + D_j \cos\beta_j \right) + 0.5\rho C_{dz} BL w^2 = \\ &m(\dot{w} - uq + vp) - Z_{\dot{w}}\dot{w} - Y_{\dot{v}} vp + X_{\dot{u}} uq \end{aligned} \tag{5.45}$$

$$\begin{aligned} &-y_b V\rho g\cos\phi\cos\theta + z_b V\rho g\sin\phi\cos\theta + \sum_{j=1}^{6} \left(y_{\text{hip}\,j} \left(-L_j \sin\beta + D_j \cos\beta_j \right) \right) + \\ &\frac{0.5\rho p^2 L \left(C_{dz} B^4 + C_{dy} H^4 \right)}{32} = I_{xx}\dot{p} + (I_{zz} - I_{yy})\, qr - (\dot{r} + pq)\, I_{xz} + \\ &(r^2 - q^2)\, I_{yz} + (pr - \dot{q})\, I_{xy} - L_{\dot{p}}\dot{p} + \left(Y_{\dot{v}} - Z_{\dot{w}} \right) vw + \left(M_{\dot{q}} - N_{\dot{r}} \right) qr \end{aligned} \tag{5.46}$$

$$
\begin{aligned}
&x_b V\rho\, g \cos\phi \cos\theta + z_b V\rho\, g \sin\theta + \frac{0.5\rho q^2 B\left(C_{dx} H^4 + C_{dz} L^4\right)}{32} + \\
&\sum_{j=1}^{6}\left(-x_{\text{hip}\,j}\left(-L_j \sin\beta + D_j \cos\beta_j\right) + z_{\text{hip}\,j}\left(D_j \sin\beta_j + L_j \cos\beta_j\right)\right) \\
&= I_{yy}\dot{q} + (I_{xx} - I_{zz})\, rp - (\dot{p} + qr)\, I_{xy} + (p^2 - r^2)\, I_{xz} + (qp - \dot{r})\, I_{yz} \\
&- M_{\dot{q}}\dot{q} + (Z_{\dot{w}} - X_{\dot{u}})\, uw + \left(N_{\dot{r}} - L_{\dot{p}}\right) pr
\end{aligned}
\tag{5.47}
$$

$$
\begin{aligned}
&- x_b V\rho\, g \sin\phi \cos\theta - y_b V\rho\, g \sin\theta + \sum_{j=1}^{6}\left(-y_{\text{hip}\,j}\left(D_j \sin\beta_j + L_j \cos\beta_j\right)\right) + \\
&\frac{0.5\rho r^2 H\left(C_{dx} B^4 + C_{dy} L^4\right)}{32} = I_{zz}\dot{r} + (I_{yy} - I_{xx})\, pq - (\dot{q} + rp)\, I_{yz} + \\
&(q^2 - p^2)\, I_{xy} + (rq - \dot{p})\, I_{xz} - N_{\dot{r}}\dot{r} + (X_{\dot{u}} - Y_{\dot{v}})\, uv + \left(L_{\dot{p}} - M_{\dot{q}}\right) pq
\end{aligned}
\tag{5.48}
$$

Equations (5.43) to (5.48) are insufficient to solve for the motion of the robot because they include ϕ and θ as variables, but make no provision to solve for them. To obtain these variables, relationships between angular rates (p, q and r) and the time rate of change of the Euler angles ($\dot{\phi}$, $\dot{\theta}$ and $\dot{\psi}$) must be considered:

$$\dot{\phi} = p + (\sin\phi \tan\theta) q + (\cos\phi \tan\theta) r \tag{5.49}$$

$$\dot{\theta} = (\cos\phi) q - (\sin\phi) r \tag{5.50}$$

$$\dot{\psi} = (\sin\phi \sec\theta) q + (\cos\phi \sec\theta) r \tag{5.51}$$

It should be noted that the equation for $\dot{\psi}$ becomes singular at $\theta = \pm 90$.

5.6. Numerical Simulation

Equations (5.43) to (5.51) can be written in the form $\dot{\vec{x}} = f(\vec{x}, \vec{u})$ where $\vec{x} = [u \quad v \quad w \quad p \quad q \quad r \quad \phi \quad \theta \quad \psi]^{\mathrm{T}}$ represents the state of the system and $\vec{u}$, a vector of variables characterizing the oscillation of the paddles, represents the input to the system. Based on the initial state $\vec{x}_0$ and the input, which varies with time, the goal is to find the time-varying state $\vec{x}$. In order to obtain $\vec{x}$, $\dot{\vec{x}}$ is calculated and is integrated. The outputs of the simulation are the position and orientation of the robot in the inertial frame *XYZ*.

The state $\bar{x}$ and the integral of $\bar{x}$ were found by numerical integration using Simulink®: a software package for modeling, simulating, and analyzing dynamical systems. Simulink® successively computes the states and outputs of the system at intervals from the simulation start time to the finish time, using information provided by the model. At the start of the simulation, the model specifies the initial states and outputs of the system to be simulated. At each step, Simulink computes new values for the system's inputs, states, and outputs and updates the model to reflect the computed values. To perform this task, Simulink® can use an assortment of solvers each geared to solving a specific type of model. The model of AQUA was simulated using variable-step continuous solver. These solvers decrease the simulation step-size to increase accuracy when a system's continuous states are changing rapidly and increase the step size to save simulation time when a system's states are changing slowly. The average time step in the simulation of AQUA was approximately 0.05 seconds. At the end of the simulation, the model reflects the final values of the system's inputs, states, and outputs [57].

Simulink® provides a graphical user interface (GUI) for building models as block diagrams, and includes a comprehensive block library of sinks, sources, linear and nonlinear components, and connectors. The user can also customize and create blocks. The built models can be simulated using a choice of integration methods. Using scopes and other display blocks, the user can see the simulation results while the simulation is running. The simulation results can be routed to the MATLAB workspace for postprocessing and visualization.

5.6.1. Implementation of Hardware Limits

As explained in Section 2.2, a proportional derivative controller calculates the torque requested from each motor. The motor cannot always supply the requested torque. A model predicting the output torque of the battery-amplifier-actuator-geartrain combination of the hexapod robot RHex, based on the requested duty cycle of the PWM amplifier, battery voltage and motor speed was developed by Dave McMordie at the Ambulatory Robotics Laboratory [51]. The model was implemented in the simulation, along with specifications of the hardware (voltage supply, amplifiers, motors and gear heads), in order to ensure that the torques supplied by the motors were within the physical limits of the system.

5.6.2. Simulation Results

The simulation inputs are the variables characterizing the oscillation of the paddles: the amplitude of oscillation, the period of oscillation, the offset angle and the amplitude ratio. The outputs of the simulation are the position and orientation of the robot in the inertial frame *XYZ*.

For an input where all paddles oscillate with a period of 0.7 seconds, an amplitude of 27°, an offset angle in line with the back of the robot and an oscillation ratio of 0.5, the robot, which has an initial velocity of 0m/s, traverses 2m in 21 seconds. It should be recalled from Section 4.2 that the flexible fin produced 3.3 times more thrust than the flat plate for a given oscillation. Assuming that the flexible fin produces about three times more thrust than the flat plate for all oscillations, the forces produced by the rigid paddle were multiplied by 3 in the simulation and the robot traversed 6.7m in 21 seconds, as shown in the first plot of Figure 5-12. As a point of comparison, pool tests were performed with the real vehicle with flexible fins in July 2004. For the same paddle motion, the real vehicle, which also had an initial velocity of 0m/s, traversed 6.4m in 21 seconds. The real vehicle also performed oscillations in pitch such as the ones shown in the fifth plot of Figure 5-12. Thus, the simulation of the robot gives outputs that are very consistent with those observed in the pool.

It should be noted from the upper plot of Figure 5-12 that the acceleration of the robot is initially very low. Between 3 and 8 seconds, the robot accelerates quickly and it then reaches a constant velocity. This behaviour can be explained as follows: as noted in Section 5.4.4.1, the inflow velocity in the simulation is taken to be the opposite of the velocity of the hip. It was shown in Section 2.3 that the net thrust over one cycle in the absence of inflow was 0. The reason why the robot is able to move forward at all is due to the fact that it generates forces in the first half of its first oscillation, which give it a small acceleration. The ensuing velocity creates a nonzero inflow, which results in a force

propelling the vehicle. The initial thrust of the paddles is very nearly zero and the vehicle has a very low acceleration. As the velocity of the robot increases, the propelling force increases as well. After a certain point, the forces produced by the paddles are used entirely to counter drag acting on the body and the robot stops accelerating.
The flow induced by the paddle displacing water, which was described in Chapter 2 for the rigid paddle model in stagnant water, is not accounted for in the simulation of the robot. Future experiments of a rigid paddle oscillating in a tow tank would help to gauge the accuracy of the rigid paddle model in the robot simulation and to determine whether inflow related to water displacement should be incorporated in the simulation of the robot, particularly at low speeds.

Figure 5-13 shows a maneuver which is more involved than the rectilinear swimming shown in Figure 5-12. The robot pitches down, as it turns right and rolls counterclockwise. While doing that, the robot moves very little along the *X*-, *Y*- and *Z*-axes. In order to perform that maneuver, all paddles of the robot except the middle left paddle oscillate with a period of 1 second, an amplitude of 6°, an offset angle in line with the back of the robot and an oscillation ratio of 0.5. The middle left paddle oscillates with a period of 1 second, an amplitude of 46°, an offset angle that is half way between the back of the robot and the bottom of the robot, and an oscillation ratio of 0.5.

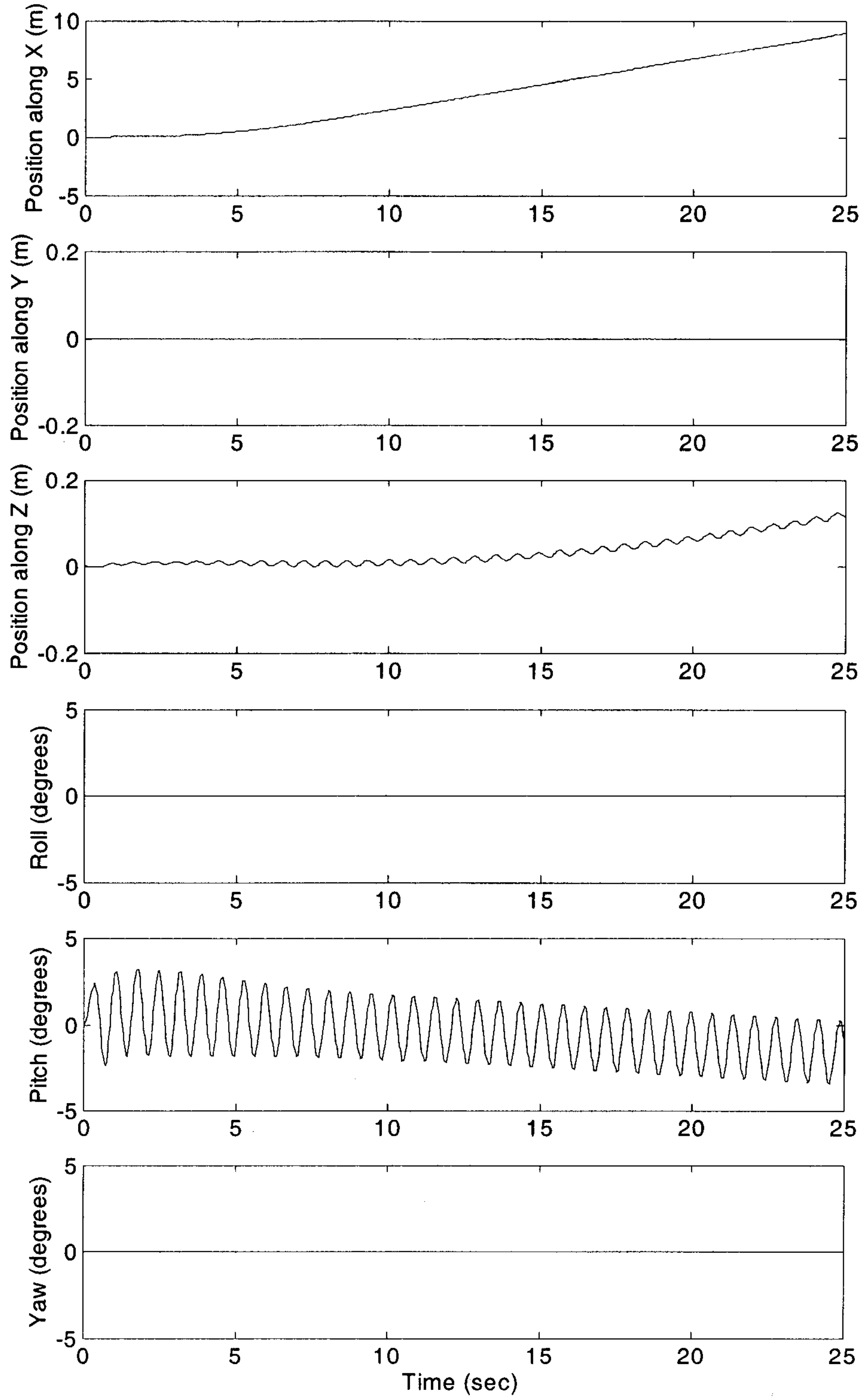

Figure 5-12: The robot position and orientation resulting from all paddles oscillating with a period of 0.7s, an amplitude of 27°, an offset angle in line with the back of the robot and an oscillation ratio of 0.5.

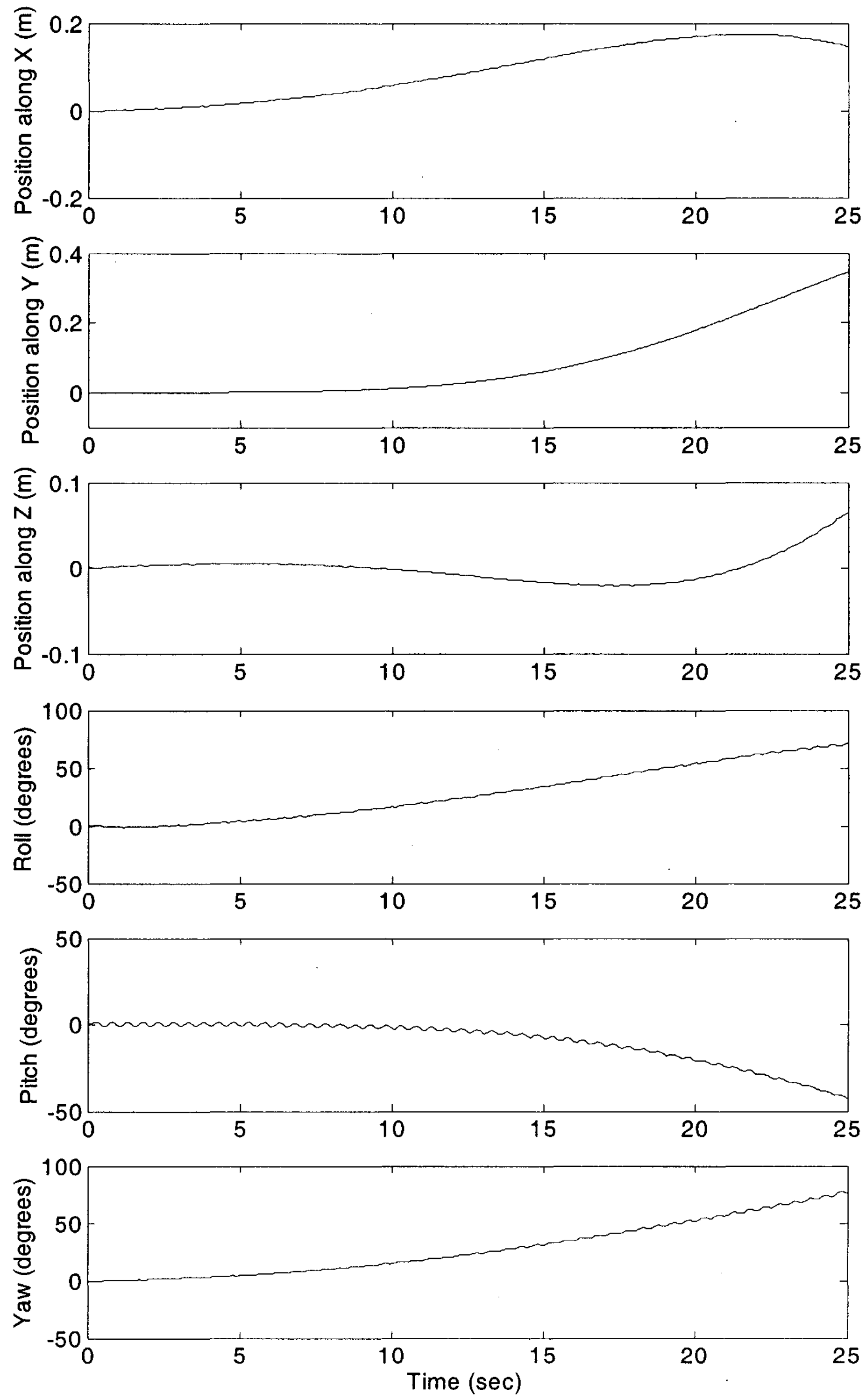

Figure 5-13: The robot position and orientation of the robot pitching down, as it turns right and rolls counterclockwise.

5.7. Animation

The simulation results were output to a scope, which displayed them as in Figure 5-9. When many of the time-varying positions and orientations are not zero, like in Figure 5-13, it can be difficult to visualize the motion of the robot in three dimensions. For that purpose, an animation of the motion of the robot was created using 3ds max®, a graphics and animation software.

The robot position along the inertial frame's *X*-, *Y*- and *Z*-axes, the robot orientation about these axes as well as the angular position of the paddles with respect to the robot were written to a file. A program was written in 3ds max® to read the file and produce an animation of the motion of the robot. Figure 5-14 shows a few frames of an animation of the maneuver illustrated in Figure 5-13.

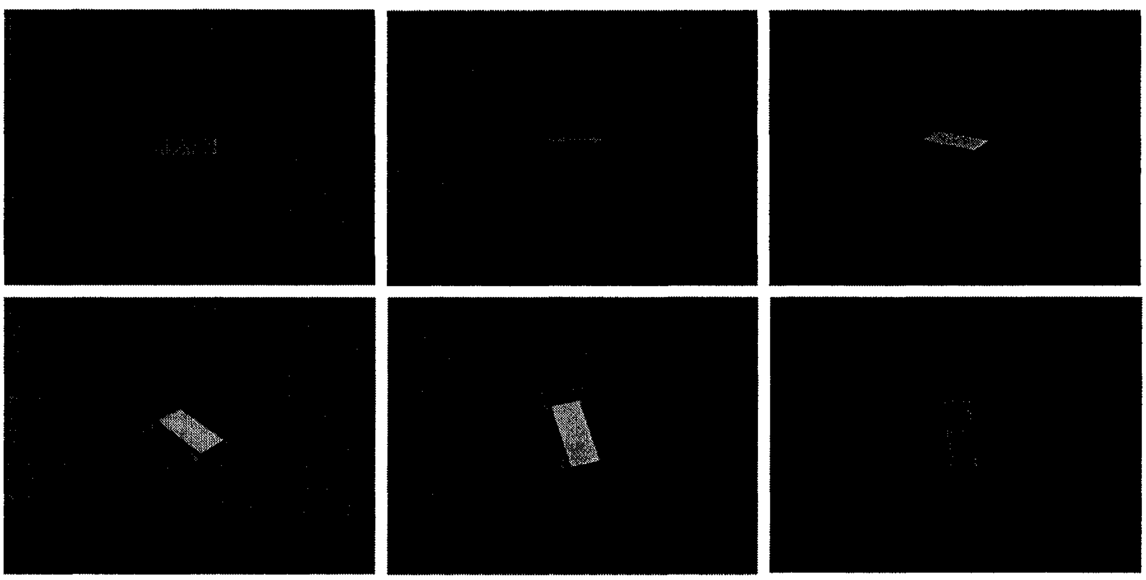

Figure 5-14: A few frames of an animation showing the robot pitching down, as it turns right and rolls counterclockwise.

6. Conclusions and Recommendations for Future Work

6.1. Conclusions

The main goal of this work was to develop a simulation of the motion of the AQUA swimming robot based on its paddle oscillations. The challenging task of characterizing the forces generated by the paddles oscillating in the water was undertaken first: a model predicting the forces produced by a rigid paddle was developed. A setup measuring the forces generated by a paddle oscillating in the water was designed and built. Rigid and flexible paddles were tested on the setup and the rigid paddle model was validated. Lastly, a simulation of AQUA, which incorporates the rigid paddle model, was developed.

The model predicting the forces generated by a rigid paddle oscillating in stagnant water was presented in Chapter 2. The model included inflow, which is the water entrained by the paddle during oscillation in a stagnant tank. Simulations showed that, in the absence of inflow, no net thrust is produced. The inflow was estimated based on the size of the paddle, the period of oscillation and the amplitude of oscillation, and was found to be inversely proportional to period and only weakly dependent on amplitude.

The experimental setup, which was designed and built to measure forces and torques produced by a paddle oscillating in the water, was described in Chapter 3. The graphical user interface developed to acquire force/torque measurements and to control the paddle was also described in that chapter. The thrust measuring setup can accommodate paddles of different design and geometry and oscillate them through symmetric and asymmetric trajectories of different amplitude and period. An impact test was performed on the structure of the thrust measuring setup. From the vibrations of the setup, natural frequencies of 16Hz and 48Hz were found.

Rigid paddles were tested on the setup in order to gauge the accuracy of the rigid paddle model. To assess the validity of the rigid paddle model, the forces predicted by the model were compared to the forces obtained experimentally. Flexible fins were tested on the setup in order to assess how they compare to rigid paddles. The rigid paddle and flexible fin experimental results were presented in Chapter 4. In all experiments, difficulties were experienced in controlling the paddle. The paddle did not track the desired trajectory accurately: the actual amplitude of oscillation was smaller than the desired one. One possible reason for which the paddle did not follow the desired trajectory accurately is that the applied torque was not great enough. Increasing the requested torques, by augmenting the gains of the PD controller resulted in instability. The poor tracking was not a serious impediment in validating the rigid paddle model. The actual trajectory was used in the simulation instead of the desired trajectory and the forces predicted by the rigid paddle model were compared to the ones obtained experimentally.

Noise at two distinct frequencies, 16Hz and 47Hz, were present in the force and torque measurements of all experiments. Since the two distinct frequencies corresponded to the natural frequencies of the thrust measuring setup, a hypothesis was made that the higher frequencies in the experimental measurements could be attributed to vibrations in the setup. A low-pass filter was applied to force and torque measurements of all experiments in order to attenuate high-frequency noise.

Of all the forces and torques measured during rigid paddle and flexible fin experiments, two were of interest: the force parallel to the offset angle direction and the force perpendicular to that direction. The parallel force is the force that propels the vehicle and should be as large as possible. The perpendicular force should be as close to zero as possible. It was found that, for a given period, time-averaged parallel forces increased with amplitude and frequency of oscillation. Time-averaged perpendicular forces were approximately zero, as they should be. It was also found that flexible fins produce greater time-averaged forces than rigid paddles. One last finding of interest is that asymmetrical oscillations, where sweep is done faster than recovery, produce greater time-averaged forces than symmetrical oscillations.

The validity of the rigid paddle model was assessed by comparing the forces predicted by the model to the forces obtained experimentally. The match between the two sets of forces was good and it provided the model validation that was sought.

After being verified, the rigid paddle was used in the simulation of AQUA to predict the forces generated by the oscillating paddles. The robot simulation was developed, as described in Chapter 5, to determine the motion of the robot resulting from the oscillation of its paddles. To visualize the motion of the robot in three dimensions, an animation was created using 3ds max, a graphics and animation software. The simulation was used to develop simple gaits that were implemented on the robot and were used to control it remotely. Comparisons between the output of the simulation and the motion of the robot during swimming pool tests are preliminary but appear to be good.

6.2. Recommendations for Future Work

There would have been no need to estimate inflow in the rigid paddle model presented in Chapter 2 if the water entrained by the oscillating paddle during experiments had been measured. To avoid having to estimate the inflow, it is suggested that future experiments include a flow sensor on the thrust measuring setup.

In Chapter 3, a recommendation was also made to stiffen the thrust measuring setup. From the response of the setup to an impact test, it was determined that the setup is very lightly damped. To dampen the vibrations of the setup, rubber was added at two places, but it made no significant difference in the natural frequency of the setup. Stiffening the setup can be done by adding members, which will prevent different parts of the setup from bending or twisting.

The data acquisition program in LabVIEW was designed to read force and torque measurements at a frequency of 100 S/s. One of the greatest problems with LabVIEW was that the time steps at which measurements were obtained had a 20% variance on the desired 0.01 seconds. Unequal iteration steps contributed to instability of the controller. Another problem with LabVIEW was that the encoder and time readings did not occur simultaneously. As a result, the paddle velocity calculated from position and time was noisy. The noisy velocity signal resulted in noisy commanded torque. In order to improve the stability of the controller, it is suggested to find a way to minimize variance in the time step length. It is also suggested to determine how encoder and time readings can occur sequentially so as to obtain a smooth velocity signal. If these tasks cannot be accomplished in LabVIEW, it could be worthwhile to consider using a real-time operating system to perform the data acquisition and motor control of the experiments.

Tests of the flexible fin used on the robot showed that it produced approximately 3 times more thrust than a rigid paddle of the same size. A model of the forces generated by the fin as a function of the inflow, the amplitude of oscillation and the frequency of oscillation must be developed. The flexible fin model can then be validated, similarly to the rigid paddle, and implemented in the robot simulation, which will then become more representative of the robot.

Beyond developing a model for flexible fins, further work can be done to characterize paddles. Some optimization can be done to find the types of oscillation as well as the oscillation parameters that produce maximum thrust, for example. As was stated in Chapter 1, when foils operate in the wake another foil or propeller, their performance is affected. Additional experimental work can be conducted to determine how the turbulent flow caused by the front paddle affects the forces produced by the middle and rear paddles. In Chapter 1, it was also stated that, when foils operate near a wall or are attached to a vehicle, there are important interaction effects, which may result in deterioration of performance. It would be useful to test the effect that the body has on the performance of the paddles.

Before having a simulation that is truly representative of the robot, several issues need to be looked at. First, the accuracy of the hydrodynamic forces acting on the robot have to be verified. Conducting tow tank tests would allow determination of the validity of the assumption that the drag force on the body of the robot is the vector sum of the drag forces acting on the three faces of the robot exposed to the incoming flow. If this assumption is not valid, modifications need to be made to the calculation of the hydrodynamic forces in the simulation, in order to obtain forces that correspond to those observed during the tow tank tests. Second, in the calculation of hydrodynamic forces and moments, a rough assumption was made that the velocity of the center of mass is responsible for the drag forces and that the angular velocities are responsible for the drag moments. In future calculations of hydrodynamic forces and moments, it is recommended to simultaneously consider the velocity of the center of mass and the angular velocities, when calculating the velocity of each point of the robot. Third, future experiments of a rigid paddle oscillating in a tow tank would help to gauge the accuracy of the rigid paddle model in the robot simulation and to determine whether inflow related to water displacement should be incorporated in the simulation of the robot, particularly at low speeds. Fourth, the equation of motion of the paddle in the simulation neglects the fact that, on top of oscillating, the paddle is moving with the robot. In the future, it is recommended to write equations of motion that take that fact into account.

Once the simulation of the robot is validated, it can be used to develop and optimize swimming gaits. The simulation can also be used to develop an algorithm, which would allow the robot to track a 3D trajectory. In this scenario, the simulation would be used to determine the paddle oscillations that will result in the desired trajectory. Alternately, if the robot is equipped with an inclinometer, a compass and/or an inertial measurement unit (IMU), the algorithm can determine the paddle oscillations that will correct the error between the actual and the desired robot position and orientation. Trajectory tracking would be a big stepping-stone towards autonomy. The robot needs to be able to follow prescribed trajectories before being able to decide the trajectories that it should follow.

Besides autonomy, the other goal of the AQUA project that has not yet been met is to enable the robot to transition between crawling at the bottom of the sea and swimming. In order to do this, a buoyancy control system would need to be developed. The system would change the buoyancy of the robot, making it negatively, neutrally or positively buoyant depending on whether it needs to walk, swim or float. When the system is developed, it should also be modeled and implemented in the simulation.

RE 25 ∅25 mm, Graphite Brushes, 20 Watt

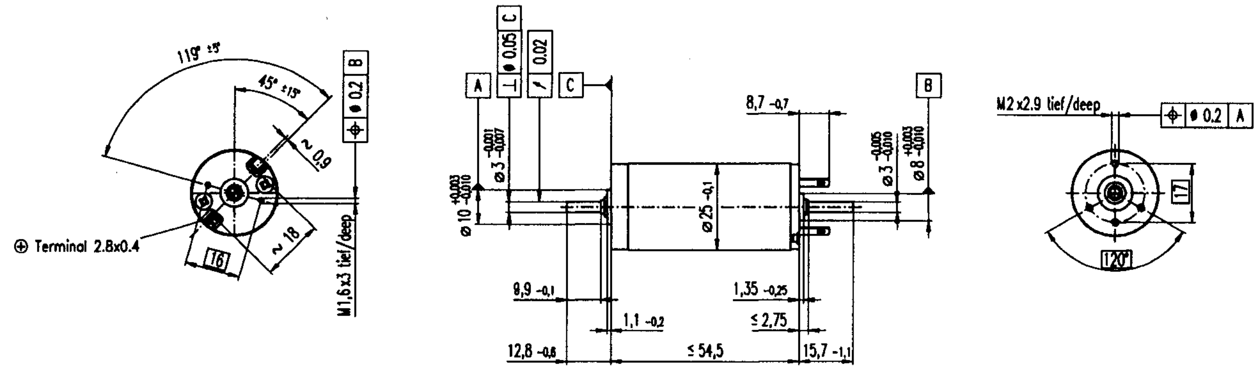

M 1:2

- Stock program
- Standard program
- Special program (on request!)

Order Number

Motor Data		Unit	118749	118750	118751	118752	118753	118754	118755	118756	118757
1	Assigned power rating	W	20	20	20	20	20	20	20	20	20
2	Nominal voltage	Volt	9.0	15.0	18.0	24.0	30.0	42.0	48.0	48.0	48.0
3	No load speed	rpm	10000	9650	10200	9550	9850	11100	10300	8230	5050
4	Stall torque	mNm	232	225	220	243	249	283	264	210	129
5	Speed / torque gradient	rpm / mNm	46.5	44.7	47.9	40.2	40.3	39.7	39.6	39.7	39.7
6	No load current	mA	110	61	54	37	31	25	20	15	9
7	Starting current	mA	29100	15700	13500	10400	8720	7940	6030	3810	1440
8	Terminal resistance	Ohm	0.309	0.953	1.33	2.32	3.44	5.29	7.96	12.6	33.4
9	Max. permissible speed	rpm	11000	11000	11000	11000	11000	11000	11000	11000	11000
10	Max. continuous current	mA	1500	1500	1500	1210	992	800	652	519	318
11	Max. continuous torque	mNm	11.8	20.6	23.5	26.1	26.1	26.3	26.3	26.3	26.3
12	Max. power output at nominal voltage	mW	52000	52800	55500	58300	62200	80400	70200	44400	16800
13	Max. efficiency	%	77	82	83	85	86	87	87	87	84
14	Torque constant	mNm / A	7.97	14.3	16.3	23.4	28.5	35.7	43.8	55	89.7
15	Speed constant	rpm / V	1200	669	585	407	335	268	218	173	106
16	Mechanical time constant	ms	5	5	5	4	4	4	4	4	4
17	Rotor inertia	gcm²	11.3	10.0	9.11	10.3	10.1	10.1	10.0	9.96	9.91
18	Terminal inductance	mH	0.03	0.09	0.12	0.24	0.35	0.55	0.83	1.31	3.48
19	Thermal resistance housing-ambient	K / W	14	14	14	14	14	14	14	14	14
20	Thermal resistance rotor-housing	K / W	3.1	3.1	3.1	3.1	3.1	3.1	3.1	3.1	3.1
21	Thermal time constant winding	s	13	12	10	12	12	12	12	11	11

Specifications

- Axial play 0.05 - 0.15 mm
- Max. ball bearing loads
  axial (dynamic)
  not preloaded 3.2 N
  preloaded 3.2 N
  radial (5 mm from flange) 16 N
  Force for press fits (static) 64 N
  (static, shaft supported) 270 N
- Radial play ball bearing 0.025 mm
- Ambient temperature range -20 ... +100°C
- Max. rotor temperature +125°C
- Number of commutator segments 11
- Weight of motor 130 g
- 2 pole permanent magnet
- Values listed in the table are nominal.
  For applicable tolerances see page 43.
  For additional details please use the maxon selection program on the enclosed CD-Rom.

Operating Range

Comments Details on page 49

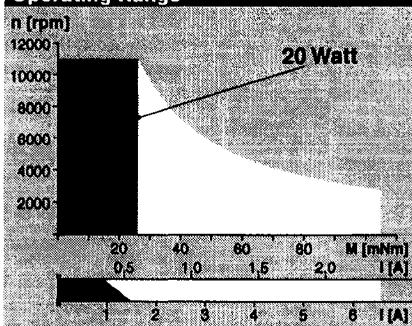

Recommended operating range

Continuous operation
In observation of above listed thermal resistances (lines 19 and 20) the maximum permissible rotor temperature will be reached during continuous operation at 25°C ambient.
= Thermal limit.

Short term operation
The motor may be briefly overloaded (recurring).

118757 Motor with high resistance winding
118749 Motor with low resistance winding

maxon Modular System

Overview on page 17 - 21

Planetary Gearhead
Ø26 mm
0.5 - 2.0 Nm
Details page 210

Planetary Gearhead
Ø32 mm
0.75 - 6.0 Nm
Details page 212 / 214

Planetary Gearhead
Ø32 mm
0.4 - 2.0 Nm
Details page 216

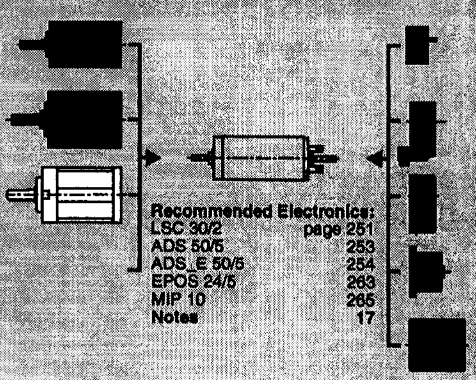

Recommended Electronics:

LSC 30/2	page 251
ADS 50/5	253
ADS_E 50/5	254
EPOS 24/5	263
MIP 10	265
Notes	17

Digital MR Encoder
128 - 1000 CPT,
3 channels
Details page 232

Digital Encoder
22 mm
100 CPT, 2 channels
Details page 234

Digital Encoder
HP HED_ 55_
500 CPT, 3 channels
Details page 236 / 238

DC-Tacho
Ø22 mm
0.52 V
Details page 246

Brake
Ø40 mm
24 VDC, 0.4 Nm
Details page 269

Planetary Gearhead GP 32 A ∅32 mm, 0.75 - 4.5 Nm

Metal Version

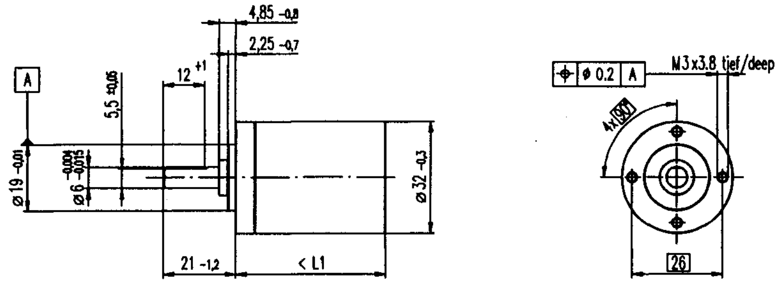

M 1:2

Technical Data

Planetary Gearhead	straight teeth
Output shaft	stainless steel
Bearing at output	ball bearing
Radial play, 5 mm from flange	max. 0.14 mm
Axial play	max. 0.4 mm
Max. radial load, 12 mm from flange	140 N
Max. permissible axial load	120 N
Max. permissible force for press fits	120 N
Sense of rotation, drive to output	=
Recommended input speed	< 6000 rpm
Recommended temperature range	-15 ... +80°C

Stock program
Standard program
Special program (on request!)

Order Number		166155	166158	166163	166164	166169	166174	166179	166184	166187	166192	166197	166202
Gearhead Data													
1 Reduction		3.7 : 1	14 : 1	33 : 1	51 : 1	111 : 1	246 : 1	492 : 1	762 : 1	1181 : 1	1972 : 1	2829 : 1	4380 : 1
2 Reduction absolute		26/7	676/49	529/16	17576/343	13824/125	421824/1715	86112/175	19044/25	10123776/8575	8626176/4375	495144/175	109503/25
3 Max. motor shaft diameter	mm	6	6	3	6	4	4	3	3	4	4	3	3
Order Number		166156	166159		166165	166170	166175	166180	166185	166188	166193	166198	166203
1 Reduction		4.8 : 1	18 : 1		66 : 1	123 : 1	295 : 1	531 : 1	913 : 1	1414 : 1	2189 : 1	3052 : 1	5247 : 1
2 Reduction absolute		24/5	624/35		16224/245	6877/56	101062/343	331776/625	36501/40	2425488/1715	536406/245	1907712/625	839523/160
3 Max. motor shaft diameter	mm	4	4		4	3	3	4	3	3	3	3	3
Order Number		166157	166160		166166	166171	166176	166181	166186	166189	166194	166199	166204
1 Reduction		5.8 : 1	21 : 1		79 : 1	132 : 1	318 : 1	589 : 1	1093 : 1	1526 : 1	2362 : 1	3389 : 1	6285 : 1
2 Reduction absolute		23/4	299/14		3887/49	3312/25	389376/1225	20631/35	279841/256	9345024/6125	2066688/875	474513/140	6436343/1024
3 Max. motor shaft diameter	mm	3	3		3	3	4	3	3	4	3	3	3
Order Number			166161		166167	166172	166177	166182		166190	166195	166200	
1 Reduction			23 : 1		86 : 1	159 : 1	411 : 1	636 : 1		1694 : 1	2548 : 1	3656 : 1	
2 Reduction absolute			576/25		14976/175	1587/10	359424/875	79488/125		1162213/686	7962624/3125	457056/125	
3 Max. motor shaft diameter	mm		4		4	3	4	3		3	4	3	
Order Number			166162		166168	166173	166178	166183		166191	166196	166201	
1 Reduction			28 : 1		103 : 1	190 : 1	456 : 1	706 : 1		1828 : 1	2623 : 1	4060 : 1	
2 Reduction absolute			138/5		3588/35	12167/64	89401/196	158171/224		2238912/1225	2056223/784	3637933/896	
3 Max. motor shaft diameter	mm		3		3	3	3	3		3	3	3	
4 Number of stages		1	2	2	3	3	4	4	4	5	5	5	5
5 Max. continuous torque	Nm	0.75	2.25	2.25	4.50	4.50	4.50	4.50	4.50	4.50	4.50	4.50	4.50
6 Intermittently permissible torque	Nm	1.1	3.4	3.4	6.5	6.5	6.5	6.5	6.5	6.5	6.5	6.5	6.5
7 Max. efficiency	%	80	75	75	70	70	60	60	60	50	50	50	50
8 Weight	g	118	162	162	194	194	226	226	226	258	258	258	258
9 Average backlash no load	°	0.7	0.8	0.8	1.0	1.0	1.0	1.0	1.0	1.0	1.0	1.0	1.0
10 Mass inertia	gcm²	1.5	0.8	0.8	0.7	0.7	0.7	0.7	0.7	0.7	0.7	0.7	0.7
11 Gearhead length L1	mm	26.4	36.3	36.3	43.0	43.0	49.7	49.7	49.7	56.4	56.4	56.4	56.4

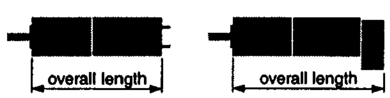

Combination

+ Motor	Page	+ Tacho / Encoder / Brake	Page	Overall length [mm] = Motor length + gearhead length + (tacho / encoder / brake) + assembly parts											
RE 25, 10 W	76			81.0	90.9	90.9	97.6	97.6	104.3	104.3	104.3	111.0	111.0	111.0	111.0
RE 25, 10 W	76	MR Encoder	232	92.0	101.9	101.9	108.6	108.6	115.3	115.3	115.3	122.0	122.0	122.0	122.0
RE 25, 10 W	76	Digital Encoder 22	234	95.1	105.0	105.0	111.7	111.7	118.4	118.4	118.4	125.1	125.1	125.1	125.1
RE 25, 10 W	76	Digital Encoder HED_ 55__	236/238	101.8	111.7	111.7	118.4	118.4	125.1	125.1	125.1	131.8	131.8	131.8	131.8
RE 25, 10 W	76	DC Tacho 22	246	103.3	113.2	113.2	119.9	119.9	126.6	126.6	126.6	133.3	133.3	133.3	133.3
RE 25, 20 W	77			81.0	90.9	90.9	97.6	97.6	104.3	104.3	104.3	111.0	111.0	111.0	111.0
RE 25, 20 W	77	MR Encoder	232	92.0	101.9	101.9	108.6	108.6	115.3	115.3	115.3	122.0	122.0	122.0	122.0
RE 25, 20 W	77	Digital Encoder 22	234	95.1	105.0	105.0	111.7	111.7	118.4	118.4	118.4	125.1	125.1	125.1	125.1
RE 25, 20 W	77	Digital Encoder HED_ 55__	236/238	101.8	111.7	111.7	118.4	118.4	125.1	125.1	125.1	131.8	131.8	131.8	131.8
RE 25, 20 W	77	DC Tacho 22	246	103.3	113.2	113.2	119.9	119.9	126.6	126.6	126.6	133.3	133.3	133.3	133.3
RE 25, 20 W	77	Brake 40	269	115.1	125.0	125.0	131.7	131.7	138.4	138.4	138.4	145.1	145.1	145.1	145.1
RE 26, 18 W	78			85.3	95.2	95.2	101.9	101.9	108.6	108.6	108.6	115.3	115.3	115.3	115.3
RE 26, 18 W	78	MR Encoder	232	96.3	106.2	106.2	112.9	112.9	119.6	119.6	119.6	126.3	126.3	126.3	126.3
RE 26, 18 W	78	Digital Encoder 22	234	102.7	112.6	112.6	119.3	119.3	126.0	126.0	126.0	132.7	132.7	132.7	132.7
RE 26, 18 W	78	Digital Encoder HED_ 55__	236/238	103.7	113.6	113.6	120.3	120.3	127.0	127.0	127.0	133.7	133.7	133.7	133.7
RE 26, 18 W	78	DC Tacho 22	246	106.3	116.2	116.2	122.9	122.9	129.6	129.6	129.6	136.3	136.3	136.3	136.3
A-max 26	113-120			71.2	81.1	81.1	87.8	87.8	94.5	94.5	94.5	101.2	101.2	101.2	101.2
A-max 26	113-119	Digital Magnetic Encoder 13	245	78.3	88.2	88.2	94.9	94.9	101.6	101.6	101.6	108.3	108.3	108.3	108.3
A-max 26	114-120	MR Encoder	232	80.0	89.9	89.9	96.6	96.6	103.3	103.3	103.3	110.0	110.0	110.0	110.0
A-max 26	114-120	Digital Encoder 22	235	85.6	95.5	95.5	102.2	102.2	108.9	108.9	108.9	115.6	115.6	115.6	115.6
A-max 26	114-120	Digital Encoder HED_ 55__	237/239	90.0	99.9	99.9	106.6	106.6	113.3	113.3	113.3	120.0	120.0	120.0	120.0
RE-max 29	143-146			71.2	81.1	81.1	87.8	87.8	94.5	94.5	94.5	101.2	101.2	101.2	101.2
RE-max 29	144/146	MR Encoder	232	80.0	89.9	89.9	96.6	96.6	103.3	103.3	103.3	110.0	110.0	110.0	110.0

Gamma

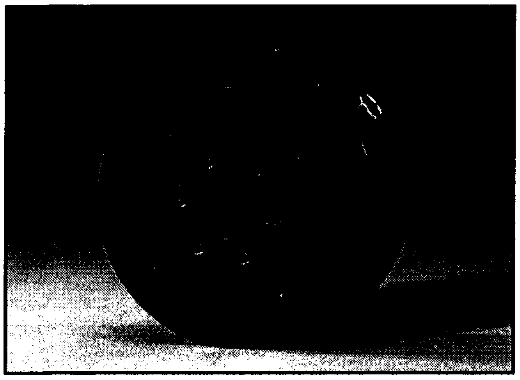

The Gamma F/T transducer
The transducer and the standard mounting adapter are made of high-strength aircraft aluminum.

"I highly recommend ATI's force/torque transducers to anyone who needs a reliable, pre-calibrated, easily programmable transducer. It is a truly versatile plug-and-play system."
Prof. Francisco Valera-Cuevas
Neuromuscular Biomechanics Laboratory
Cornell University, Ithaca, NY

BENEFITS AND FEATURES

Extremely High strength
- Precision machined from high-strength aircraft aluminum.
- Maximum allowable overload values are 7.8 to 27 times rated capacities.

High Signal-to-Noise Ratio
Silicon strain gauges provide a signal 75 times stronger than conventional foil gauges. This signal is amplified, resulting in near-zero noise distortion.

TYPICAL APPLICATIONS

- **Real-time force control**
- **Haptics feedback**
- **Prosthetic device testing**
- **Robotic assembly**
- **Automotive part testing**

English-Calibrated Sensing Ranges	US-7.5-25		US-15-50		US-30-100	
Fx, Fy (±lb)	7.5		15		30	
Fz (±lb)	25		50		100	
Tx, Ty (±in-lb)	25		50		100	
Tz (±in-lb)	25		50		100	
Resolution						
F/T System Type †	CON	DAQ	CON	DAQ	CON	DAQ
Fx, Fy (lb)	1/160	1/2560	1/80	1/1280	1/40	1/640
Fz (lb)	1/80	1/1280	1/40	1/640	1/20	1/320
Tx, Ty (in-lb)	1/80	1/1280	1/40	1/640	1/20	1/320
Tz (in-lb)	1/80	1/1280	1/40	1/640	1/20	1/320

Metric-Calibrated Sensing Ranges	SI-32-2.5		SI-65-5		SI-130-10	
Fx, Fy (±N)	32		65		130	
Fz (±N)	100		200		400	
Tx, Ty (±N-m)	2.5		5		10	
Tz, (±N-m)	2.5		5		10	
Resolution						
F/T System Type †	CON	DAQ	CON	DAQ	CON	DAQ
Fx, Fy (N)	1/40	1/640	1/20	1/320	1/10	1/160
Fz (N)	1/20	1/320	1/10	1/160	1/5	1/80
Tx, Ty (N-m)	1/500	1/8000	3/1000	3/16000	1/200	1/3200
Tz (N-m)	1/500	1/8000	3/1000	3/16000	1/200	1/3200

Contact ATI for complex loading information. Resolutions are typical. † *CON = Controller F/T System, DAQ = 16-bit DAQ F/T System*

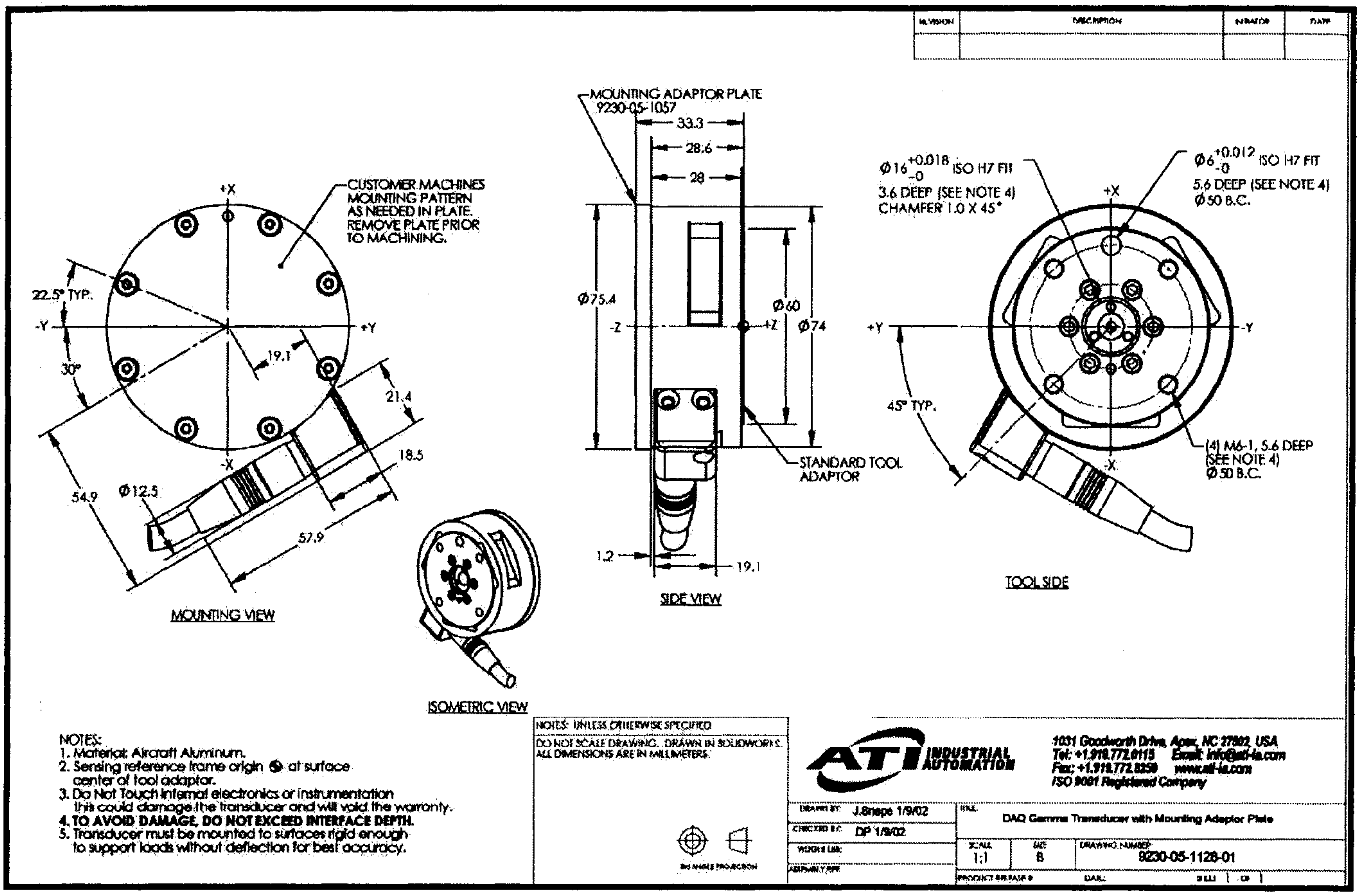

Single-Axis Overload	English	Metric
Fxy	±270 lb	±1200 N
Fz	±910 lb	±4100 N
Txy	±690 in-lb	±79 N-m
Tz	±730 in-lb	±82 N-m
Stiffness (Calculated)	**English**	**Metric**
X-axis & Y-axis force (Kx, Ky)	52×10^3 lb/in	9.1×10^6 N/m
Z-axis force (Kz)	100×10^3 lb/in	18×10^6 N/m
X-axis & Y-axis torque (Ktx, Kty)	93×10^3 in-lb/rad	11×10^3 N-m/rad
Z-axis torque (Ktz)	140×10^3 in-lb/rad	16×10^3 N-m/rad
Resonant Frequency (Measured)		
Fx, Fy, Tz	1400 Hz	
Fz, Tx, Ty	2000 Hz	
Physical Specifications	**English**	**Metric**
Weight †	0.56 lb	250 g
Diameter †	2.97 in	75.4 mm
Height †	1.31 in	33.3 mm

† *Specifications include standard interface plates.*

Appendix B

Theoretical derivation of the point of application of the drag force on the paddle

$$
\begin{aligned}
D &= \int_0^l \int_0^w 0.5\rho C_D (\dot{\gamma} z)^2 \, dydz \\
&= 0.5\rho C_D \dot{\gamma}^2 \, y\Big|_0^w \frac{z^3}{3}\Big|_0^l \\
&= 0.5\rho C_D \dot{\gamma}^2 w \frac{l^3}{3} \\
&= 0.5\rho C_D \left(\dot{\gamma} \frac{l}{\sqrt{3}} \right)^2 wl
\end{aligned}
$$

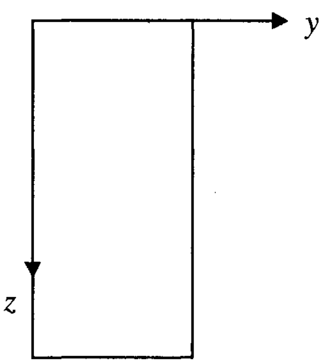

where D is the drag force, w is the width of the paddle and l is the length of the paddle

The velocity in the calculation of the drag force is that of the point which is at $l/\sqrt{3}$ from the y-axis.

$$
\begin{aligned}
M &= \int_0^l \int_0^w 0.5\rho C_D (\dot{\gamma} z)^2 \, zdydz \\
&= 0.5\rho C_D \dot{\gamma}^2 \, y\Big|_0^w \frac{z^4}{4}\Big|_0^l \\
&= 0.5\rho C_D \dot{\gamma}^2 w \frac{l^4}{4} \\
&= D \times \text{point of application of } D \\
&= 0.5\rho C_D \left(\dot{\gamma} \frac{l}{\sqrt{3}} \right)^2 wl \times \frac{3}{4} l
\end{aligned}
$$

The point of application of the drag force is at $\frac{3}{4}l$ from the y-axis

References

[1] J.M. Thorleifson, T.C. Davies, M.R. Black, D.A. Hopkin, R.I. Verrall, A. Pope, I. Monteith, V. Den Hertog, B. Butler, "The Theseus autonomous underwater vehicle. A Canadian success story" *MTS/IEEE Conference Proceedings OCEANS '97*, Volume 2, pp. 1001 – 1006, October 1997.

[2] Information on Ariel available electronically on website of iRobot: http://www.irobot.com.

[3] Northeastern University Marine Science Center. Biomimetic Underwater Robot Program (BURP). Ambulatory Underwater Robot. Information available electronically at http://www.dac.neu.edu/msc/burp.html.

[4] J. Ayers and J. Crisman. The Lobster as a Model for an Omnidirectional Robotic Ambulation Control Architecture. In R. Beer, R. Ritzman and T. McKenna, editors, *Biological Neural Networks in Invertebrate Neuroethology and Robots*, pp. 287-316. Academic Press, 1992.

[5] M. Buehler, U. Saranli and D.E. Koditschek, *"Single actuator per leg robotic hexapod"*, McGill University, The Regents of the University of Michigan: USA, 2002, US Patent 6,481,513.

[6] U. Saranli, M. Buehler and D.E. Koditschek. "RHex: A Simple and Highly Mobile Hexapod Robot", *The International Journal of Robotics Research,* Volume 20, pp. 616-631, July 2001.

[7] J. D. Weingarten, G. A. D. Lopes, M. Buehler, R. E. Groff and D. E. Koditschek, "Automated Gait Adaptation for Legged Robots." *IEEE Int. Conf. On Robotics and Automation (ICRA),* Volume 3, pp.2153-2158, April 2004,

[8] E. Z. Moore, D. Campbell, F. Grimminger and M. Buehler, "Reliable Stair Climbing in the Simple Hexapod 'RHex'.", *IEEE Int. Conf. on Robotics and Automation (ICRA)* Volume 3, pp. 2222-2227, May 2002.

[9] D. McMordie and M. Buehler, "Towards Pronking with a Hexapod Robot.", *4th Int. Conf. on Climbing and Walking Robots*, September 2001.

[10] D. Campbell and M. Buehler, "Preliminary Bounding Experiments in a Dynamic Hexapod.", *Experimental Robotics VIII*, 2003, pp. 612-621.

[11] U. Saranli and D.E. Koditschek. "Back Flips with a Hexapedal Robot.", *IEEE Int. Conf. On Robotics and Automation (ICRA)* Volume 3, pp. 128-134, May 2002.

[12] N. Neville and M. Buehler, "Towards Bipedal Running of a Six Legged Robot.", *12th Yale Workshop on Adaptive and Learning Systems*, May 2003.

[13] C. Prahacs, A. Saunders, M. K. Smith, D. McMordie and M. Buehler, "Towards Legged Amphibious Mobile Robotics", *The Inaugural Canadian Design Engineering Network (CDEN) Design Conference*, July 2004.

[14] C. Georgiades, A. German, A. Hogue, H. Liu, C. Prahacs, A. Ripsman, R. Sim, L.-A. Torres, P. Zhang, M. Buehler, G. Dudek, M. Jenkin and E. Milios, "AQUA: An Aquatic Walking Robot", *IEEE/RSJ International Conference on Intelligent Robots and Systems, IROS*, 2004.

[15] J.Gray, Studies in animal locomotion. IV. The propulsive powers of the dolphin. *J. Exp. Biol.* 13, pp. 192-199.

[16] Picture of Karman street taken from
http://www.enseeiht.fr/hmf/travaux/CD0102/travaux/optmfn/gpfmho/01-02/grp1/presenta.htm

[17] M.S. Triantafyllou, G.S. Triantafyllou and D.K.P. Yue, "Hydrodynamics of Fishlike Swimming", *Annu. Rev. Fluid Mech.,* Volume 32, pp. 33–53, 2000.

[18] K.A. Harper, M.D. Berkemeier and S. Grace, "Modeling the dynamics of spring-driven oscillating-foil propulsion", *IEEE Journal of Oceanic Engineering,* Volume 23, pp. 285-296, 1998.

[19] S.D.Kelly and R.M.Murray, "Modelling efficient pisciform swimming for control", *International Journal of Robust and Nonlinear Control*, Volume 10, pp. 217-241, 2000.

[20] R.Mason and J.W.Burdick, "Experiments in carangiform robotic fish locomotion", *Proceedings of IEEE International Conference on Robotics and Automation*, Volume 1, pp. 428 – 435, April 2000.

[21] M.S. Triantafyllou, A.H. Techet, F.S. Hover, "Review of Experimental Work in Biomimetic Foils", *IEEE Journal of Oceanic Engineering*, Volume 29, Issue 3, pp. 585 – 594, July 2004.

[22] M. Koochesfahani, "Vortical patterns in the wake of an oscillating foil," *American Institute of Aeronautics and Astronautics Journal*, Volume 27, pp. 1200–1205, 1989.

[23] K. D. Jones, C. M. Dohring and M. F. Platzer, "Experimental and computational investigation of the Knoller-Betz effect", *American Institute of Aeronautics and Astronautics Journal*, Volume 36, no.7, pp. 1240–1246, 1998.

[24] J. O. Scherer, "Experimental and Theoretical Investigation of Large Amplitude Oscillating Foil Propulsion Systems", U.S. Army Engineering Research and Development Laboratories, 1968.

[25] J. M. Anderson, K. Streitlien, D. S. Barrett and M. S. Triantafyllou, "Oscillating foils of high propulsive efficiency", *J. Fluid Mech.*, Volume 360, pp. 41–72, 1998.

[26] J. A. Sparenberg and A. K.Wiersma, "On the efficiency increasing interaction of thrust producing lifting surfaces", in *Swimming and Flying in Nature*, T.Wu, C. J. Brokaw and C. Brennen, Eds. New York: Plenum, Volume 2, pp. 891–917, 1975.

[27] M. Koochesfahani and P. Dimotakis, "A Cancellation Experiment in a Forced Turbulent Shear Layer", *American Institute of Aeronautics and Astronautics Technical Paper 88-3713-CP*, 1988.

[28] R. Gopalkrishnan, M. S. Triantafyllou, G. S. Triantafyllou and D. S. Barrett, "Active vorticity control in a shear flow using a flapping foil", *J. Fluid Mech.*, Volume 274, pp. 1–21, 1994.

[29] K. Streitlien, G. S. Triantafyllou and M. S. Triantafyllou, "Efficient foil propulsion through vortex control", *American Institute of Aeronautics and Astronautics Journal*, vol. 34, no. 11, pp. 2315–2319, 1996.

[30] D. N. Beal, F. S. Hover and M. S. Triantafyllou, "The effect on thrust and efficiency of an upstream Karman wake on an oscillating foil", *Proc. 12th Int. Symp. Unmanned Untethered Submersible Technology*, 2001.

[31] M. Kemp, B. Hobson and C. Pell, "Energetics of the oscillating fin thruster", *Proc. 13th Int. Symp. Unmanned Untethered Submersible Technology*, 2003.

[32] P. Prempraneerach, F.S. Hover and M.S. Triantafyllou, "The effect of chordwise flexibility on the thrust and efficiency of a flapping foil", *Proc. 13th Int. Symp. Unmanned Untethered Submersible Technology*, 2003.

[33] R. Ramamurti and W.C. Sandberg, "Simulation of flow about flapping airfoils using a finite element incompressible flow solver", *American Institute of Aeronautics and Astronautics Journal*, Volume 39, pp. 253-260, 2001.

[34] S.N.Singh, A.Simha and R.Mittal, "Biorobotic AUV Maneuvering by Pectoral Fins: Inverse Control Design Based on CFD Parameterization", *IEEE Journal of Oceanic Engineering*, Volume 29, no.3, July 2004.

[35] R.Mittal, I.Akhtar, M.Bozkurttas and F.M.Najjar, "Towards a Conceptual Model of a Bio-Robotic AUV: Pectoral Fin Hydrodynamics", *Proc. 13th Int. Symp. Unmanned Untethered Submersible Technology*, 2003.

[36] R.Mittal, "Computational Modeling in Bio-hydrodynamics: Trends, Challenges and Recent Advances", *Proc. 13th Int. Symp. Unmanned Untethered Submersible Technology*, 2003.

[37] M. S. Triantafyllou and G. S. Triantafyllou, "An efficient swimming machine", *Scientific American*, March 1995.

[38] J. Czarnowski, R. Cleary and B. Kreamer, "Exploring the possibility of placing traditional marine vessels under oscillating foil propulsion.", *Proceedings of the Seventh International Offshore and Polar Engineering Conference*, Volume 2, pages 76-81, May 1997.

[39] D.Barrett, M.Grosenbaugh and M.Triantafyllou, "The optimal control of a flexible hull robotic undersea vehicle propelled by an oscillating foil", *Proceedings of the IEEE Symposium on Autonomous Underwater Vehicle Technology*, 1-9, 1996.

[40] B. Hobson, M. Kemp, A. Leonessa, "Integration of a hovering module with the Morpheus AUV: application to MCM missions", *MTS/IEEE Oceans*, Volume 1, 29-31, pp. 207 – 209, Oct. 2002.

[41] M. Kemp, B. Hobson, J. Janet, C. Pell and E. Tytell, "Assessing the Peroformance of Oscillating Fin Thruster Vehicles", *Proceedings of 12th International Symposium on Unmanned, Untethered Submersible Technology,* 2001.

[42] F.E.Fish, G.V.Lauder, R.Mittal, A.H.Techet, M.S.Triantafyllou, J.A.Walker and P.W. Webb, "Conceptual Design of the Construction of a Biorobotic AUV Based on Biological Hydrodynamics", Pages: 207 – 209, *Proc. 13th Int. Symp. Unmanned Untethered Submersible Technology*, 2003.

[43] S.Licht, V.Polidoro, M.Flores, F.S.Hover and M.S.Triantafyllou, "Design and Projected Performance of a Flapping Foil AUV", *IEEE Journal of Oceanic Engineering*, Volume 29, Issue 3 , Pages 786 – 794, July 2004.

[44] Isiki et al., "Research on Oscillating Fin Propulsion", *Journal of Naval Architects of Japan*, No. 642, 1983.

[45] A. J. Healey, S. M. Rock, S. Cody, D. Miles and J. P. Brown, 1995, "Toward an Improved Understanding of Thruster Dynamics for Underwater Vehicles", *Autonomous Underwater Vehicle Technology. IEEE Journal of Oceanic Engineering*, Volume 20, Issue 4 , pp. 354 –361, 1994.

[46] J. P. Evans, "Dynamics Modeling and Performance Evaluation of an Autonomous Underwater Vehicle", M.Eng. Thesis, Dept. Mechanical Engineering, McGill University, Montreal, August 2003.

[47] F. W. Reigels, *Aerodynamische Profile*, Muchen, R. Oldenbourg, 1958.

[48]C. C. Critzos, H. H. Heyson, R. W. Boswinkle Jr., *Aerodynamic Characteristics of NACA 0012 Airfoil Section at Angles of Attack From 0° to 180°*, NACA TN 3361, 1955.

[49] R.D. Blevins, *Applied Fluid Dynamics Handbook*, Van Nostrand Reinhold Company, 1984.

[50] D. J. Inman, *Engineering Vibrations*, Prentice Hall, 1994, revised 1996.

[51] D. McMordie, C. Prahacs and M. Buehler, "Towards a dynamic actuator model for a hexapod robot", *Proceedings IEEE International Conference on Robotics and Automation*, Volume 1, pp. 1386 – 1390, September 2003.

[52] B. Etkin, *Dynamics of Flight Stability and Control*, Wiley, Second Edition, 1982.

[53] T.I. Fossen, *Guidance and Control of Ocean Vehicles*, John Wiley & Sons Ltd, UK, 1994.

[54] K.T. Patton, "Tables of Hydrodynamic Mass Factors for Translational Motion", *ASME Paper No. 65-WA/Unt-2*, 1965.

[55] ESDU Fluid forces, pressures and moments on rectangular blocks. Engineering Sciences Data Item No. 71016, ESDU International plc., London, 1971.

[56] B.W. McCormick, Aerodynamics, Aeronautics and Flight Mechanics, John Wiley & Sons, 1995.

[57] Simulink Documentation,
http://www.mathworks.com/access/helpdesk/help/toolbox/simulink/